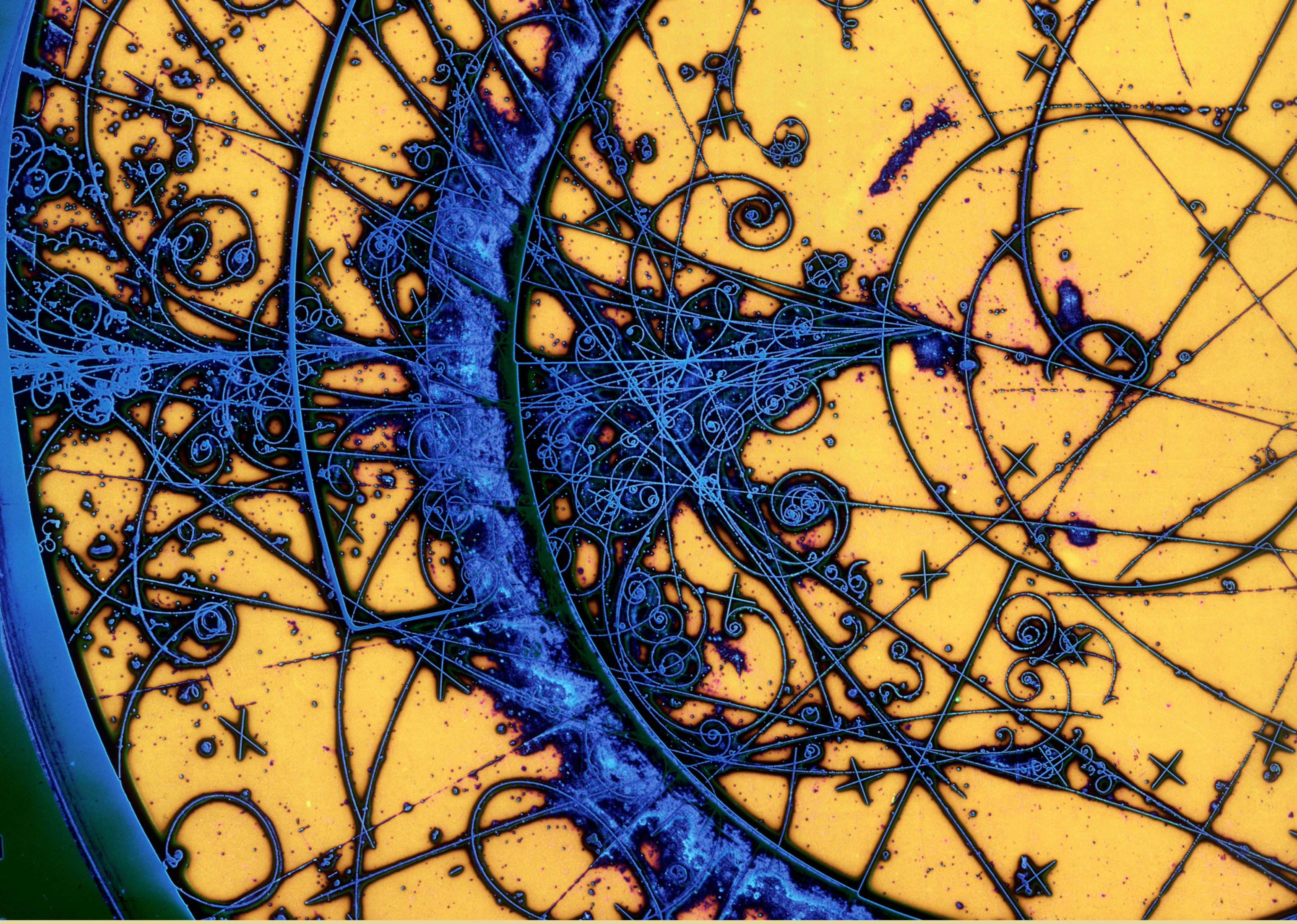

Miguel Daiyen Carvalho Won

FLAVOUR-CHANGING-NEUTRAL-CURRENTS IN TOP QUARK PHYSICS

Dissertação de Doutoramento na área científica de Física, especialidade em Física Teórica,
orientada pelo Professor Doutor Rui Alberto Serra Ribeiro dos Santos e co-orientada pelo Professor Doutor António Joaquim Onofre de Abreu Ribeiro Gonçalves, e apresentada
ao Departamento de Física da Faculdade de Ciências e Tecnologias da Universidade de Coimbra

Junho de 2014

· U C ·

UNIVERSIDADE DE COIMBRA

Flavour-Changing-Neutral-Currents in top quark physics

Miguel Won
Departamento de Física, Universidade de Coimbra

Dissertação submetida para obtenção do grau de
Doutor em Física, Especialidade em Física Teórica

Orientador: Professor Doutor Rui Alberto Serra Ribeiro dos Santos
Co-Orientador: Professor Doutor António Joaquim Onofre de Abreu Ribeiro Gonçalves

Coimbra, Junho de 2014

Abstract

This work presents a study on top quark flavour-changing-neutral-currents (FCNC) interactions. These interactions are characterised by a vertex with a top quark and a light u or c quark, together with one of the neutral gauge bosons: gluon, photon and Z boson. They are highly suppressed in the Standard Model (SM), and are therefore a good place to search for physics beyond the SM.

We start by presenting a theoretical introduction divided in three chapters. The first one is dedicated to the subject of collider physics, where the main aspects related to the physics and mathematical background of collider experiments are discussed. A brief account of the SM is then given followed by a more detailed chapter where the subject of Effective Theories and their use in FCNC top quark physics is described.

In the following chapters we first present a study where improvement of FCNC top quark interaction limits were tested in an electron-positron collider. A post LHC scenario where no FCNC physics is found was assumed. Then we present a study on the well-known asymmetry measured in top quark pair production at the Tevatron, and its deviation with respect to the SM prediction. The study addresses the problem using a set of six dimension effective operators in order to reproduce this asymmetry. In the following chapter a new Monte Carlo event generator, MEtop, is presented. It is a generator conceived primarily for FCNC direct top events with LO and NLO precision, but it also generates FCNC single top @ LO. The generator allows the user to generate events from three different sets of effective operators. Finally, experimental simulations were performed in order

to study the performance of MEtop in FCNC top quark searches @ LHC.

Resumo

Este trabalho apresenta um estudo sobre interacções FCNC (*flavour-changing-neutral-currents*) do quark top. Estas interacções são caracterisadas por um vértice entre o quark top e o quark leve u ou c, em conjunto com um dos bosões neutros: gluão, fotão e o bosão Z. Elas são altamente suprimidas pelo Modelo Padrão (MP), o que produz um boa janela de procura de física para além do MP.

Começamos pela apresentação de uma introdução teórica dividida em três capítulos. O primeiro é dedicado ao assunto de Física de Colisionadores, onde são discutidos os principais aspectos relacionados com os fundamentos físicos e matemáticos de experiências de colisão. Uma breve descrição do MP é depois dada seguida por um capítulo onde se descreve com mais detalhe os fundamentos das Teorias Efectivas e o seu uso na física FCNC do quark top.

Nos capítulos seguintes apresentamos primeiro um estudo onde o melhoramento dos limites da interacção FCNC do quark top foram testados num colisionador electrão-positrão. Para este estudo foi assumido um cenário post LHC onde física FCNC não é descoberta. No capítulo seguinte é apresentado um estudo sobre a conhecida medida da assimetria na produção de quarks top no Tevatron, e o seu desvio relativamente às previsões do MP. O estudo aborda o problema através de um conjunto de operadores effectivos de dimensão seis, de forma a reproduzir a referida assimetria. De seguida é apresentado um novo gerador de acontecimentos Monte Carlo, MEtop. É um gerador concebido principalmente para acontecimentos "FCNC Direct top" com precisão LO e NLO, apesar de também gerar "FCNC single top @ LO". O gerador permite ao utilizador gerar acontecimentos a partir de três conjuntos diferentes de operadores efectivos. Finalmente,

foram realizadas simulações de forma a estudar a *performance* dos acontecimentos gerados pelo MEtop, bem como a procura de quarks top FCNC no LHC.

Acknowledgements

I would like to thank all people involved in the work presented in this thesis: the LIP group people that were always available to the needed help, as well as family and friends not directly connected but that gave me their full social support during all these years.

I would also like to thank the Southampton High Energy Physics theory group (SHEP), in particular Stefano Moretti, who received me with all care and support in their PhD program.

A special acknowledgement goes to both my supervisors António Onofre and Rui Santos, who helped me so much, in work and life, since I started to work with both.

The work presented in this thesis was monetarily supported by Fundação para a Ciência e Tecnologia through the grant SFRH/BD/45041/2008.

Contents

List of Figures

List of Tables

1

Introduction

The Large Hadron Collider (LHC) at CERN has now concluded its operation at 8 TeV centre-of-mass energy. The LHC top factory will allow us to scrutinise the heaviest of all known quarks with unprecedented precision. Flavour physics is on the top of the agenda as one of most interesting research topics that can be addressed at this collider, through the study of flavour-changing-neutral-currents (FCNC) in top-quark production and decay. In fact, a wide variety of models show a strong dependence on the measurable FCNC quantities: for instance, top quark FCNC branching ratios can vary from extremely small in the Standard Model (SM) to measurable values at the LHC in a variety of SM extensions (1). Therefore, the large number of top quarks being produced provide a means to search for deviations from the SM, however small they are. It is clear that the simplest way to search for new FCNC physics is to look for rare top decays like for example $t \to q\gamma$ where $q = u, c$ is an up-quark or c-quark, respectively. Limits on the $BR(t \to q\gamma)$ were set indirectly at LEP (2, 3, 4, 5) and HERA (6, 7) and directly at the Tevatron (8) (see (9) for references and details). Presently, the best bound on the photon FCNC current is the one from HERA while the best experimental bounds on $BR(t \to qZ)$ were obtained at the Tevatron (10, 11) and at the LHC (12, 13). Finally, the best bound on the strong FCNC current tqg was recently obtained in direct top production at the LHC (14).

In this work we will present new contributions to the field of top FCNC physics. Using an effective operator formalism we will be able to scrutinise classes of models that have the SM as its low energy limit. This effective Lagrangain approach will be implemented using specific sets of higher order dimensional operators. The actual Lagrangian is build specifically for the study of top quark FCNC physics. Therefore, besides respecting the SM symmetries, redundant operators are removed by using the equation of motion and Fierz identities. This effective formalism is presented in chapter 4 just after a short review of the SM in chapter 3

Chapter 2 is dedicated to collider physics. It presents a brief overview of the mathematical and physics aspects needed to understand collider physics experiments. Concerning the mathematical issues, the main focus will be on Monte Carlo integration, together with a detailed account of the well known VEGAS algorithm. There is also a section describing Markov Chains and the Metropolis algorithm. This algorithm will be used to map a multidimensional phase space with a consequent increase of computational efficiency. Concerning the physical aspects, the main topic is the full event simulation at a collider experiment (except for hadronization). The starting point is the calculation of the *partonic cross section* which amounts to the phase space integration of the transition amplitude, $|M|^2$, for the process under study. This calculation, when performed at some fixed order in perturbation theory, gives rise to divergences. This problem can be solved analytically by the introduction of higher order corrections to the partonic cross section. However, when the aim is to simulate real events, alternative techniques must be introduced. A common method to avoid the problematic divergences is to restrict the phase space kinematics to safe regions. The dangerous ones, where the divergences occur, will then be covered by the introduction of parton showers. This method is part of a technique called *matching*. Additionally, the parton showers are needed to simulate the full event, since they will be responsible for the simulation of so-called jets. In chapter 2 we will show how to correctly generate higher order events using a combination of analytical methods and parton showers.

In chapter 5 we focus on top FCNC physics in a post LHC scenario. As mentioned above, the gap between the current limits on the top FCNC effective couplings and the SM predictions is still humongous. This gap will be gradually closed as more data is gathered at the LHC. However, it is important to address the question of what will be the next step in top FCNC physics after the LHC. Clearly, one of the possibilities investigated at present by the physics community is a new electron-positron collider. Hence, in chapter 5 we compare the predictions for the LHC operating at 14 TeV with the ones for a future electron-positron collider. With this chapter we also wish to contribute to the physics case of a future electron-positron collider (and possibly a photon-photon collider) in the field of top FCNC physics.

Chapter 6 is devoted to the study of the measured forward-backward asymmetry at Tevatron in the framework of FCNC effective operators. This asymmetry is measured in the $t\bar{t}$ production process. Althogh the SM predicts no asymmetry at tree-level, the most recent measurement performed by CDF collaboration shows an asymmetry of $A_{FB}^{t\bar{t}} = 0.158 \pm 0.074$ (15), far from the SM Next-to-Leading (NLO) correction $A_{FB}^{t\bar{t},\mathrm{SM}} = 0.058 \pm 0.009$ (16, 17). Additionally, the total $t\bar{t}$ cross section measured is in agreement with the SM prediction. Therefore, this scenario could hint at physics beyond the SM. In order to probe this scenario we have introduced a set of top FCNC effective operators that could induce a forward-backward asymmetry in $t\bar{t}$ production. This set include strong, electroweak and four-fermion operators. A Monte Carlo Markov Chain fit was then performed using a set of physical experimental observables, allowing us to understand if top FCNC operators contribute to the observed asymmetry at the Tevatron.

In chapter 7 we present a new generator, MEtop, for the study of top quark physics with effective operators. It is the first generator which can generate FCNC direct top events with NLO precision in QCD. The matching procedure mentioned above is implemented using the so-called *effective approximation* (18). In this approximation the phase space is divided in two regions, where one will be covered by the parton showers while the other is described by the transition amplitude. The matching is then performed using a resolution parameter, which in the present case is the top transverse momentum. Besides FCNC direct top, MEtop additionally generates FCNC top production processes, namely FCNC $t + jet$ production. Several sets of effective operators for top FCNC studies are available to use in MEtop. These include combinations of strong, electroweak and four-fermion operators allowing the study of a number of Lorentz structures.

In chapter 7 some examples will be provided.

Finally, in chapter 8 we present a study on the performance of the MEtop generator by performing a detector level analysis of the process of direct top production at the LHC. We start by reproducing the ATLAS experiment analysis presented in (14), but for $\sqrt{s} = 8$ TeV. We compare the use of LO and NLO generated events to understand what is the error in considering a constant K-factor. We also investigate the contribution of the FCNC $t + jet$ events to the same analysis. We then perform a second analysis where an extra hard jet is considered. We then compare the limits obtained for the strong FCNC coupling constants for the different scenarios.

2

Collider Physics

2.1 Introduction

Over the last century, particle physics research has always been supported by experiments where particle collisions took place. The core of many of the apparata used in those experiments involved some type of collision - from the cloud chamber used in the beginning of the 20th century to the present day high energy proton-proton collider, CERN's LHC. It is in this context that collider physics discipline emerges. In this chapter a short description of the fundamental concepts of collider physics is presented. The main focus will be on the computational and mathematical tools and in particular in the use of Monte Carlo generators and also more phenomenological issues like for example the physics of parton showers.

2.2 Monte Carlo event generation

The most relevant physical quantity in any collision process is its cross section. Experimental analyses are performed using this information as well as the cross section behaviour with the measurable kinematical variables. The cross section of a given process is defined as the *probability of some interaction to occur* and therefore it can be measured experimentally just by counting the events in the initial and final states. Initial and final states refer to the times before and after the collision. Mathematically, this probability is calculated within the framework of Quantum Field Theory (QFT), and is done by writing a transition amplitude (actually its square), with respect to a specific configuration in phase space. This amplitude's square is usually denoted by $|M|^2$. In this context, the total cross section can be viewed as a weighted average, where the sum extends to all kinematically allowed phase space configurations and where each point in this space is weighted by the value $|M|^2$ at that point. This calculation is in fact just a Riemann sum, which means that the total cross section calculation is no more that an integration of $|M|^2$ in the allowed phase space domain. As one would expect, these $|M|^2$ amplitudes are usually long and complex expressions which in most cases cannot be integrated analytically. To solve this problem, particle physicists usually use numerical methods, in particularly the very popular method of integration known as VEGAS (19).

2.2.1 VEGAS

We start by reviewing the basic principle of Monte Carlo integration. The starting point is the useful approximation shown in equation 2.1:

$$I = \int_V f(x)dx \sim V \times \frac{1}{N}\sum_i^N f(x_i) = V < f >, \tag{2.1}$$

where x_i are random points in a generic V space. The integral is then interpreted as a simple function average, $< f >$, normalised to the volume phase space. The next step is to estimate the precision of such approximation which is done by calculating the variance of f and its relation to the integral variance, σ_I. The two variances are shown in equations 2.2 and 2.3:

$$\sigma_f^2 \quad = \quad \frac{1}{N}\sum_{i=1}^N (f(x_i) - < f >)^2 =< f^2 > - < f >^2 \tag{2.2}$$

$$\sigma_I^2 \quad \equiv \quad Var(I) = Var(\frac{V}{N}\sum f) = \frac{V^2}{N^2}\sum Var(f) = \frac{V^2}{N}\sigma_f^2. \tag{2.3}$$

Hence, the error of σ_I behaves as $1/\sqrt{N}$. When compared with other methods, like for example the Trapezoidal rule or Simpson numerical integration, where for a d dimensional case the error goes with $N^{-2/d}$ and $N^{-4/d}$ respectively, we conclude we are facing an inefficient numerical method of integration. However, equations 2.2 and 2.3, have exactly the same form whether we are working in 1 or in d dimensional space. Therefore, the error in a MC integration always behaves as $1/\sqrt{N}$, regardless of the integration space dimension d. We conclude that, for high dimensional integration, the MC method is more efficient, and consequently the preferred one in particle physics, due to the frequently high number of final state particles in each collision, which leads to high dimensional phase spaces.

In order to improve the convergence rate of $1/\sqrt{N}$ there are mainly two variations of the above MC integration: *Stratifed sampling* and *Importance sampling.* In *Stratifed sampling* the integrand phase space domain is divided into k^d subspaces, where k is the total number of divisions performed in each dimension. Each subspace is then a hypercube where MC integration can be separately performed. The full integral I will be the sum of partial integrals I_j, with $j = 1, ..., k^d$, which can be written as

$$I = \sum_{j=1}^{k} \frac{Vol(M_j)}{N_j} \sum_{i}^{N_j} f(x_i^j), \tag{2.4}$$

where N_j is the total number of sample points taken in the M_j hypercube. The corresponding variance is

$$\sigma_I = \sum_{j=1}^{k} \frac{Vol(M_j)^2}{N_j} \sigma_f^2(M_j). \tag{2.5}$$

This result does not guarantee that *Stratifed sampling* has a faster convergence behaviour. From 2.5 we can only say that if we are able to choose the M_j hypercubes, in such a way that the variance is reduced in each individual hypercube, then we are sure to have a faster convergence rate. This is where *Importance sampling* comes into play. In this sampling method, the random points are orientated through a probability density function (pdf), in such a way that the integral variance will be smaller as compared to the case of uniformly generated random points. The pdf can be introduced via a change of variables as shown in equation 2.6.

$$\begin{gathered}\int f(x)dx = \int \frac{f(x)}{p(x)}p(x)dx = \int \frac{f(x)}{p(x)}dP(x),\\ \text{where} \quad p(x) = \frac{\partial^d}{\partial x_1 ... \partial x_d}P(x) \quad \text{and} \int p(x)dx = 1. \end{gathered} \tag{2.6}$$

The integral is obviously equivalent to the one in equation 2.1, and the statistical error is again given by $V\sigma_f/\sqrt{N}$

$$\begin{aligned} E &= V\frac{1}{N}\sum_{i=1}^{N}\frac{f(x_i)}{p(x_i)} \\ \sigma_f^2 &= \frac{1}{N}\sum_{i}^{N}\left(\frac{f(x_i}{p(x_i)}\right)^2 - E^2. \end{aligned} \tag{2.7}$$

The variance now depends on the pdf one uses, and therefore it can be minimised by an appropriate pdf definition. A perfect choice would be $p(x) = cf(x)$, which by using equation 2.7 would result in $\sigma_f = 0$, and therefore a precise result. However, the use of this pdf would require sampling points from it, and that in turn would mean that the integral I was known; but I is precisely the quantity we want to calculate! Therefore one usually chooses a pdf that can reproduce as reliable as possible the shape of the integrand function reducing the final variance.

The VEGAS-algorithm is an iterative combination of these two methods: *Stratifed* and *Importance sampling.* The algorithm starts by defining a grid by dividing the phase space into the k^d subspaces mentioned above. In each of these d-dimensional cubes a simple MC integration is performed, which then results in a grid readjustment according to the weight each region has in the integral. After this step, a new iteration starts, with the sampling points weighted according to the new grid. In many MC tools, like event generators, this method is implemented in a two step calculation. The first one aims to find the best possible grid, for which several iterations are performed with a small number of MC integration sampling points. In the second step, a single iteration is defined, and a considerable number of MC sampling points are requested, resulting in a very good precision for the final integral. The final integral estimation is obtained by combining cumulatively all iterations. For each one we get the following estimate E_j and variance σ_j^2

$$E_j = V \frac{1}{N_j} \sum_{i=1}^{N_j} \frac{f(x_i)}{p(x_i)} \quad , \quad \sigma_j^2 = \frac{1}{N_j} \sum_{i=1}^{N_j} \left(\frac{f(x_i)}{p(x_i)} \right)^2 - E_j^2 \tag{2.8}$$

where N_j is the number of sampling points in the iteration j. The final result reads

$$E = \frac{\left(\sum_{j=1}^{m} E_j \left(\frac{E_j^2}{\sigma_j^2} \right) \right)}{\left(\sum_{j=1}^{m} \frac{E_j^2}{\sigma_j^2} \right)} \quad , \quad \sigma_I = E \left(\frac{E_j^2}{\sigma_j^2} \right)^{-1/2} , \tag{2.9}$$

which is no more than a weighed average over all iterations.

In MEtop (chap. 7) all cross section integrations are calculated using the VEGAS algorithm embedded in the Cuba library (20).

2.2.2 Regularization

A common issue when dealing with the $|M|^2$ integration is the problem of singularities. It is known that almost all transition amplitudes contain dangerous propagators, that are likely to result in possible divergences. These singularities arise mainly due to poles of virtual particles propagators of the form

$$\frac{1}{q^2 - m^2}, \tag{2.10}$$

which diverge in the case where virtual particles become on-shell. A common method to solve this problem is to include an extra term in the denominator of equation 2.10, so that the on-shell divergent point is avoided. The introduction of this new factor is justified by considering higher order corrections to the propagator and it is usually written as

$$\frac{1}{q^2 - m^2 - i\Gamma m}, \tag{2.11}$$

where Γ is the particle's width. In the current physical production processes implement in MEtop, there are two of these potentially dangerous poles: one from top quark and another from W boson propagators. In both cases, this correction has been implemented and the value of the top and W widths can be defined in the parameters file ”param.txt”.

Another problem one has to deal with, when performing MC integrations, is the lack of precision in peaked regions. It will always result in large contributions to the final variance, even with the VEGAS algorithm, originating a poor precision in the MC integration. A common solution is to perform a *regularization*, in order to transform these peaks in smooth and/or flat regions, easier to integrate. As an example we consider the case where the peaked region has its origin in an s-channel propagator; in that case one usually applies a change of variables to the integral

$$\int_{s_{min}}^{s^{max}} d\hat{s}, \tag{2.12}$$

where s represents here the off-shell particle's squared momentum. To regularize it we start by applying the following identity:

$$\int_{s_{min}}^{s^{max}} d\hat{s} = \int_{s_{min}}^{s^{max}} d\hat{s}\frac{g(s)}{g(s)} \quad , \quad g(s) = \frac{\Gamma M}{\tan^{-1}(\frac{s-M^2}{\Gamma M}) - \tan^{-1}(\frac{s_{min}-M^2}{\Gamma M})}. \tag{2.13}$$

The new integration variable is defined by:

$$\rho = \tan^{-1}(\frac{s-M^2}{\Gamma M}), \tag{2.14}$$

which results in the transformation

$$d\hat{s}g(s) = \frac{d\rho}{\tan^{-1}(\frac{s-M^2}{\Gamma M}) - \tan^{-1}(\frac{s_{min}-M^2}{\Gamma M})} \tag{2.15}$$

and in the final integration

$$\int_{\rho_{min}}^{\rho^{max}} d\rho\frac{(\Gamma M\tan(\rho))^2 + M^2\Gamma^2}{\Gamma M} \quad , \quad \rho_{\substack{max\\min}} = \tan^{-1}(\frac{s_{\substack{max\\min}} - M^2}{\Gamma M}). \tag{2.16}$$

In the production processes introduced in MEtop, there are only two dangerous divergent poles that one needs to regularize. These peaks come from the resonant behaviour of the top quark and W boson propagators. In MEtop, regularization was introduced in the cross section integration as well in the event generation.

2.2.3 Event generation

The next step in a MC event generator is, as expected, to generate events. One starts by sampling points from the phase space according to their configuration weights, which are given by the transition amplitude $|M|^2$. One of the first problems one has to deal with is that in order to perform such sampling the inverse of $|M|^2$ must be used. However, for a typical high energy scenario this is usually impossible, due to the its highly complicated form. Therefore, just like *importance sampling* uses a pdf to sample the integration points, the same idea can be used, in combination, once more, with *stratified sampling*, to sample the phase space points where the integrand has its larger contributions. Now, instead of calculating an average, and therefore a MC integration, we just have to apply an acceptance-rejection method algorithm (Von Neumann) in order to save, or not, our final event coordinates. In figure 2.1 a simple example of this method is exemplified. In a), the pdf adopted is $Ch(x)$, where the $C \geq 1$ and $h(x)$ a uniform distribution whose value is equal to the maximum of $f(x)$ (in the example $C = 1$). The phase space points (here x) are sampled according to $Ch(x)$, and the event is accepted if and only if $uCh(x_i) \leq f(x_i)$, where x_i is the phase-point in question, and u a uniform random number between 0 and 1. In b), an improvement is obtained. Here, the pdf is a step function, and the points are sampled according to the same algorithm, with the difference that now the random x are more likely to be inside the section where the function has its peak, producing a more efficient event generation.

In MEtop, the event generation is performed using this accept-rejection algorithm, where a d-dimensional grid is defined, with d being the number of independent variables for the physical process in question. The first step is to find the maximum value for each cube. This is done throwing a total of 250 random points per cube. The largest value is then multiplied by a factor $C = 1.5$. With the grid calculation performed, a cumulative function is then built and the event generation is ready to be started. As in the example above, a cube is found according to its weight and the event configuration is saved according to the accept-rejection algorithm.

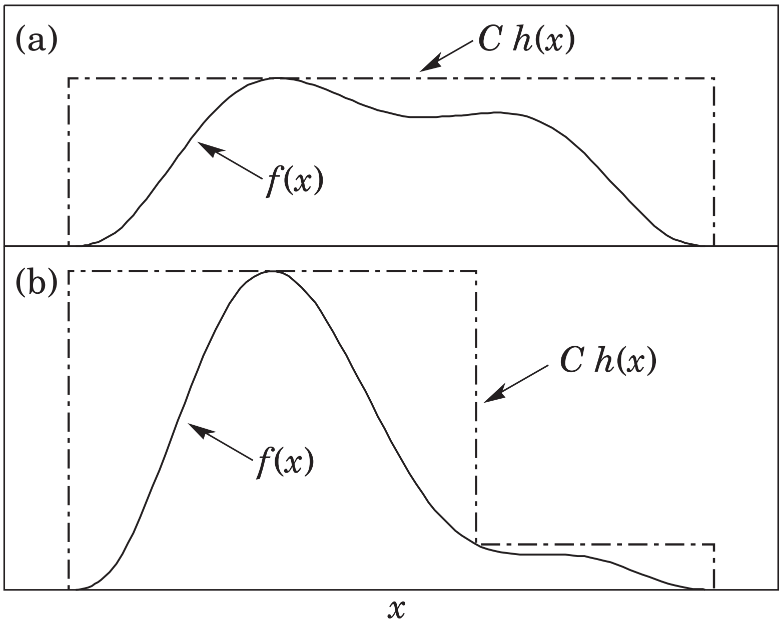

Figure 2.1: Acceptance-Rejection method. From (21)

2.2.4 LHE format

When one event configuration is accepted, all the information regarding the parton (momentum, spin, etc.) should be written in a standard format, so that any external software is able to read it. Additionally, in most cases events are generated at the partonic level only and therefore all subsequent physical processes, like for example showering and hadronization, must be handled by other software like PYTHIA (22) or HERWIG (23). Hence, MEtop outputs the event information in the known LHE (24) format. This is a standard format containing all relevant information about a partonic event, and can be read by most high energy MC generators.

2.3 Theory of Hadronic collisions

2.3.1 Hard Process

A parton level cross section is characterised by the interaction between asymptotically free states, which do not exist in Nature in a stable state. In order to connect these partonic collisions with the real process, we must take into consideration the fact that initial partons are "extracted" form colliding beams of nucleons. This is the case of the LHC, which is a proton-proton collider. The real process is related to the parton level one through the introduction of the so-called parton distributions functions (PDF). In short, these functions give us the probability "to extract" the initial partons from the nucleon under consideration, for a given momentum p and a specific factorization scale μ_F. In doing this, we assume a factorization process, which means we consider the partonic process to be independent of the nucleon configuration. The extraction and the collision are interpreted to occur at different "times", which allow us to perform each calculation separately. The convoluted cross section can then be written as:

$$\sigma_{H_1H_2}(p_1,p_2)=\sum_{ij}\int dx_1x_2f_i^{H_1}(x_1,\mu_F)f_j^{H_2}(x_2,\mu_F)\hat{\sigma}_{ij}(x_1p_1,x_2p_2), \qquad (2.17)$$

where $\hat{\sigma}$ and σ represent the partonic and total cross section, respectively. The sums over i and j are included in order to account for all possible production processes originating the same final state. The f functions are the already mentioned PDF. They are phenomenologically modelled by several groups, like for example CTEQ (25) or MRST (26), and depend on the momentum fraction x_i (the ratio of the parton momentum to the nucleon momentum), as well as on the factorization scale μ_F. Typically, this scale is chosen to be of the same order as that of the hard scattering process. For example, for all physical processes in this work, which concern top quark production, we use $\mu_F = M_{top}$. In the section where parton showers are discussed we will elaborate on the reasons for this choice.

The partonic cross section, $\hat{\sigma}$, is calculated through a perturbative series. In QCD, this series is an expansion in the strong coupling constant α_S, where the first term correspond to what is usually called Leading Order (LO), the second term Next-to-Leading Order (NLO), and so on. Once we start calculating these higher order corrections, unwanted though unavoidable divergences will arise. In order to have a better understanding of these issues, we will now analyse in more detail an example of a NLO calculation.

2.3.2 NLO calculation

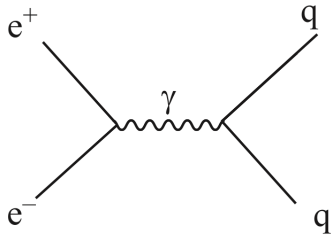

Figure 2.2: Born diagram of $e\bar{e} \to q\bar{q}$. From (27)

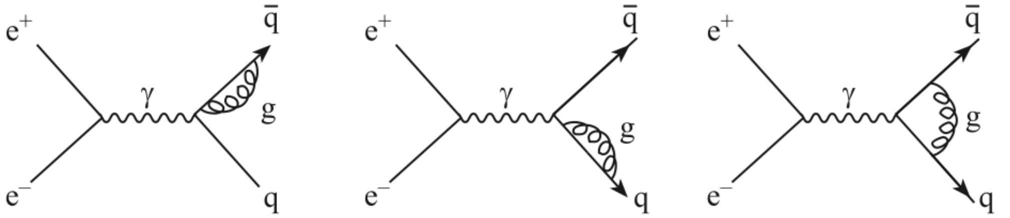

Figure 2.3: Virtual corrections to $e\bar{e} \to q\bar{q}$. From (27)

The LO calculation is the first term in a QCD perturbative calculation. Although in most calculations the LO is the largest contribution to the cross section, its theoretical uncertainty together with the need to match the attained experimental accuracy forces the calculation of higher order contributions to the cross section. Matching the experimental precision at colliders and in particular at the LHC requires high precision calculations in order to test the SM limits, or search for physics beyond it. Therefore, NLO calculations should be performed whenever possible. We present an overview on how this type of calculation is performed. To simplify, we show the NLO calculation of the process $e\bar{e} \to q\bar{q}$, where only the photon exchange is considered. In figure 2.2 we show the Born diagram for such process. Its cross section is proportional to $|M^B_{qq}|^2$ (where M_{qq} is the transition amplitude and the superscript B stands for Born-level) , and since there are no QCD interactions involved, it is labelled as order α^0_S. The inclusion of virtual corrections is done by simply inserting QCD loops in the Born diagram. This is shown in figure 2.3. As a result, the total cross section is proportional to $|M^B_{qq} + M^V_{qq}|^2$, which results in a sum of the form: $A\alpha^0_S + B\alpha^1_S + C\alpha^2_S$. The NLO cross section is the sum of the first and second terms. For this process, the Born cross section is easily calculated to give (28):

$$\sigma_{q\bar{q}} = N_c Q_q^2 \frac{4\pi\alpha^2}{3s}, \tag{2.18}$$

where N_c is the total number of colours and Q_q is the quark charge. By including loop diagrams, unavoidable divergences will emerge. These can be divided in two types: Ultraviolet (UV) and Infrared (IR) divergences. UV divergences are related to ill-defined distribution in QFT and for some theories they can be removed by the so-called process of renormalization. Whenever it is possible to remove all UV divergences the theory is said to be renormalisable. The infinities appear in the bare parameters like masses and coupling constants, and are removed by addition of counterterms in such a way that the renormalised parameters are fixed by experiment. This is called renormalisation procedure. One of the most used techniques to deal with the infinities is *dimensional regularization.* The phase space integration is performed not in $D = 4$ but in $D = 4 - 2\epsilon$ dimensions, where the limit $\epsilon \to 0$ is taken at the end. This technique is used because the divergences can be clearly isolated in powers of ϵ.

In this particular example we are presenting, i.e., $e^+e^- \to q\bar{q}$, the UV NLO QCD corrections cancel when we add all diagrams and therefore there is no dependence on the renormalization scale. We should emphasise however that in general there is a dependence in the renormalization scale that has to be taken into account. We now move to the study of IR divergences as they are the main purpose of this section. In equation 2.19 we present the virtual corrections the cross section for $e\bar{e} \rightarrow q\bar{q}$ (28):

$$\sigma^V_{q\bar{q}} = \sigma_{q\bar{q}} 3Q_q^2 \frac{C_F \alpha_S}{2\pi} H(\epsilon)[-\frac{2}{\epsilon^2} - \frac{3}{\epsilon} - 8 + O(\epsilon)] \tag{2.19}$$

$$H(\epsilon) = \frac{3(1-\epsilon)^2}{(3-2\epsilon)\Gamma(2-2\epsilon)}, \tag{2.20}$$

where $C_F = \frac{N_c^2-1}{2N_c}$ and Γ is the Euler Gamma function. In this expression only IR divergences appear and the final result is obtained by taking the limit $\epsilon \rightarrow 0$. As we can see the divergences are isolate in poles of ϵ. The $1/\epsilon$ is related to the collinear divergences while $1/\epsilon^2$ concerns the soft divergence terms. We have now to consider another process of the same order in the strong coupling constant, the real emission process. As we will see, this process will remove the infinities introduced by the virtual corrections. The reason to introduce the real emission diagrams is the detector's resolution limitations in any experiment, which makes a process with a collinear or soft real emission indistinguishable from the same process with no emission. Therefore, since one must account for all possible processes to be detected, the real emission diagram with a low energy gluon or a gluon collinear with a quark must be considered. For the present case the diagrams are shown in figure 2.4.

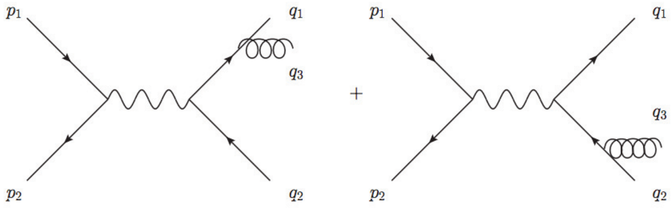

Figure 2.4: Real radiation correction. From (27)

Applying again dimensional regularization the result can be written as (28):

$$\sigma_{q\bar{q}g} = \sigma_{q\bar{q}} 3Q_q^2 \frac{C_F \alpha_S}{2\pi} H(\epsilon)[\frac{2}{\epsilon^2} + \frac{3}{\epsilon} + \frac{19}{3} + O(\epsilon)]. \tag{2.21}$$

It is clear that all poles have the opposite sign of the ones in equation 2.19.

Therefore, when adding the contributions, the final result is free of divergences. We should mention that when dealing with NLO corrections of processes with quarks in the initial state, the soft divergences also cancel but the collinear singularity is absorbed by a redefinition of the quark distribution function. The soft terms cancellation works for any physical process as proved by the so-called KLN theorem (29, 30). This property is called *infrared safety*.

Regarding UV divergences, we have stated that all divergences cancel out at NLO. However, when one calculates the NNLO corrections, a renormalization of the coupling constant α_s must be introduced. There are several ways to implement this renormalization procedure and as a consequence the final result will have a scale dependence. This scale is what is usually called renormalization constant μ_R, and, in principle, if one would be able to sum to all orders in α_S, the dependence on μ_R constant would disappear. As it is well known, it is impossible to sum to all orders in α_S. Therefore μ_R is usually chosen by looking for the region where the calculated physical observable change less with μ_R, i.e., the *plateau* region. Since this is not a truly reliable method to remove unwanted scale sensitivity, μ_R is considered to be a contribution to the systematic error of any physical observable, and to determine this error the scale is usually varied between $\mu_R/2$ and $2\mu_R$.

We now show in equation 2.22 the general formula for a production process with n partons in the final state at NLO,

$$d\sigma^{NLO} = B(\Phi_n)d\Phi_n + V(\Phi_n)d\Phi_n + R(\Phi_{n+1})d\Phi_{n+1} \tag{2.22}$$

where $B(\Phi_n)$ stands for the Born contribution, $V(\Phi_n)$ are the virtual corrections and $R(\Phi_{n+1})$ the real emission process, which is characterised by having a different number of final state particles, specifically $n+1$ partons. This leads to an additional problem when event simulation with NLO precision is required. As we saw above, this does not present an analytical problem since the divergences are isolated and cancelled through the *dimensional regularization* method. However, when an event simulation is needed, one cannot use the same technique due to the fact that 4-dimensional numerical points must be used. This problem will be addressed bellow.

2.4 Parton Showers

2.4.1 Introduction

Just like electric charges emit electromagnetic radiation through *bremsstrahlung* emission, a coloured particle, quark or gluon, will also radiate "QCD radiation", i.e., gluons, due to "colour charge" acceleration. This emission process occurs before and after the hard process takes place, and is characterised by a cascade of *collinear* and *soft* gluons. These emissions result in a radiation bunch that can be viewed as a shower of partons, which, in consequence of hadronization, are the experimentally observed jets.

In principle, we could apply the ideas explained above and calculate the full final "showered state Matrix Element". Of course, because of the high number of final partons, this is far from doable and therefore an alternative procedure must be used. Besides, even if we would manage to calculate and integrate such ME, we would still had to deal with all divergences associated with collinear and soft partons, typical in a fixed-order ME calculation.

2.4.2 $e\bar{e} \to \gamma \to q\bar{q}$

In order to solve this problem we start by analysing again in more detail the simple production process $e\bar{e} \to \gamma \to q\bar{q}$. The amplitude $|M|_{q\bar{q}}$ can be written as:

$$\mathcal{M}_{q\bar{q}} = iQ_q e^2 \bar{v}(p_2)\gamma_\mu u(p_1)\frac{g^{\mu\nu}}{s}\bar{u}_a(q_1)\gamma_\nu \delta_{ab} v_b(q_2), \tag{2.23}$$

where p_1 and p_2 are the positron and electron momenta, q_1 and q_2 the external quarks momenta, and a, b the colour running indices. After squaring and integrating it, we get the following cross section:

$$\sigma_{q\bar{q}} = N_c Q_q^2 \frac{4\pi\alpha^2}{3s}. \tag{2.24}$$

As discussed this is the LO result (order α_S^0) which is free of divergences. In order to calculate the NLO correction we follow the steps summarised in equation 2.22.

For the real part we just have to include a gluon emission from each of the external leg as shown in figure 2.4. The correspondent amplitude is given by:

$$\begin{aligned} \mathcal{M}_{q\bar{q}g} &= iQ_q e^2 \bar{v}(p_2)\gamma_\mu u(p_1)\frac{g^{\mu\nu}}{s}\bar{u}(q_1) i g_s \not{\epsilon}^a t^a \frac{i(\not{q}_1 + \not{q}_3)}{(q_1+q_3)^2}\gamma_\nu v(q_2) && (2.25) \\ & -iQ_q e^2 \bar{v}(p_2)\gamma_\mu u(p_1)\frac{g^{\mu\nu}}{s}\bar{u}(q_1) i g_s \not{\epsilon}^a t^a \frac{i(\not{q}_2 + \not{q}_3)}{(q_2+q_3)^2}\gamma_\nu v(q_2), && (2.26) \end{aligned}$$

which leads to

$$\frac{1}{4}\sum |\mathcal{M}_{q\bar{q}g}|^2 = 24 C_F Q_q^2 e^4 g_s^2 \frac{(q_1.p_1)^2 + (q_1.p_2)^2 + (q_2.p_1)^2 + (q_2.p_2)^2}{(p_1.q_2)(p_1.q_3)(q_2.q_3)}. \tag{2.27}$$

In order to integrate it we use the phase space formula

$$\int d\Phi_3 = \frac{s}{128\pi^3}\int dx_1 dx_2 \quad , \quad x_i = \frac{2E_i}{\sqrt{s}}, \tag{2.28}$$

where the integral runs over a Dalitz plot contour, and the x_i variables are related with the particle's momentum through:

$$x_1 = 1 - \frac{2(q_2.q_3)}{s} \tag{2.29}$$

$$x_2 = 1 - \frac{2(q_1.q_3)}{s} \tag{2.30}$$

$$x_3 = 1 - \frac{2(q_1.q_2)}{s}, \tag{2.31}$$

where $x_1 + x_2 + x_3 = 1$. These analytical manipulations are quite useful because the final real emission cross section can be written in the simple formula

$$d\sigma_{q\bar{q}g} = \sigma_{q\bar{q}} C_F \frac{\alpha_s}{2\pi}\frac{x_1^2 + x_2^2}{(1-x_1)(1-x_2)} dx_1 dx_2. \tag{2.32}$$

We can easily check that this cross section is singular for $x_1 \to 1$ and $x_2 \to 1$, which correspond to the soft and collinear singularities. In order to distinguish them we use equations 2.29-2.31 to rewrite:

$$q_1.q_3 = \frac{s}{2}(1 - x_2) = E_1 E_3 (1 - \cos\theta_{13}) = \frac{s x_1 x_3}{4}(1 - \cos\theta_{13}) \tag{2.33}$$

$$q_2.q_3 = \frac{s}{2}(1 - x_1) = E_2 E_3 (1 - \cos\theta_{23}) = \frac{s x_2 x_3}{4}(1 - \cos\theta_{23}), \tag{2.34}$$

which results in

$$1 - x_1 = \frac{x_2 x_3}{2}(1 - \cos\theta_{23}) \tag{2.35}$$

$$1 - x_2 = \frac{x_1 x_3}{2}(1 - \cos\theta_{13}). \tag{2.36}$$

Additionally, we can write the following relation:

$$\frac{x_1^2 + x_2^2}{(1 - x_1)(1 - x_2)} = \frac{1 + x_2}{x_1 - 1} + \frac{1 + x_1}{x_2 - 1}. \tag{2.37}$$

These equations clarify the origin of the problematic singularities. The collinear divergences are both originated from the $\cos\theta_{13} \to 1$ and $\cos\theta_{23} \to 1$ limits. Each one can be interpreted as a collinearity between the emitted gluon and each of external quarks. $\cos\theta_{23} \to 1$ corresponds to a collinearity between partons 2 and 3 and $\cos\theta_{13} \to 1$ to a collinearity between partons 1 and 3. Besides these two, we can still point out a third singular point, $x_3 \to 0$, which physically represents the soft singularity. A second conclusion that can be drawn from equation 2.37 is that the final result can be written as the product of two distributions. This means that the real radiation process, $e\bar{e} \to q\bar{q}g$, can be viewed as two distinct physical processes: a first one where the hard process occurs, namely $e\bar{e} \to q\bar{q}$, followed by an independent gluon emission from either one of the external quarks. Therefore, we are again facing the possibility of factorization, which on one the hand allow us to simplify the calculations, and on the other hand to apply the same idea recursively. We can now start to picture how we will simulate the total collision process. Applying this same idea iteratively in a Monte Carlo type algorithm, we will be able to "dress" the hard process with successive emissions. This process is what is called a parton shower that ultimately corresponds to the observed jets.

In order to implement these emissions iteratively, we first make a suitable change of variables. Defining p_{T} as the gluon transverse momentum and z the energy fraction with respect to its hadron's parent energy, we can write:

$$\begin{aligned} x_1 &= \frac{p_{\mathrm{T}}^2}{s} + z && (2.38) \\ x_2 &= \frac{p_{\mathrm{T}}^2}{s(z-1)} + 1 && (2.39) \\ dx_1 dx_2 &= z(1-z)(1-z-\frac{z}{z-1}\frac{p_{\mathrm{T}}^2}{s}). && (2.40) \end{aligned}$$

Because the cross section is heavily enhanced in the $p_{\mathrm{T}} \to 0$ region, a p_{T}^2 expansion of equation 2.32 can be performed. In the low p_{T} region we can then write

$$d\sigma_{q\bar{q}g} = \sigma_{q\bar{q}} \sum_{partons} C_F \frac{\alpha_s}{2\pi} \frac{dp_{\mathrm{T}}^2}{p_{\mathrm{T}}^2} dz \frac{1+z^2}{1-z}. \qquad (2.41)$$

The collinear divergences are now located in the regions where $p_{\mathrm{T}} \to 0$ while the soft singularities appear in the limit $z \to 1$. In order to deal with them we first need to understand what is the physical reason behind their existence. In an exclusive analysis, we would be looking for a final state with two partons (or two-jet state to be more realistic) in the case of $e\bar{e} \to q\bar{q}$, or a final state with three partons (three jet state) in the case of $e\bar{e} \to q\bar{q}g$. However, we are already aware that it is not possible to observe such definite final states. First, because there is no way to tell weather we are detecting just one parton or two collinear partons with the same momentum. Second, because it is not possible to experimentally detect a single parton with a negligibly small amount of energy. One solution is to introduce a resolution parameter in our analysis, so that one is able to parametrize the detector's physical limits. This parameter can be the parton energy, the total or the transverse momentum, or any other discriminating variable. In this case we define a cutoff Q_0 on the p_{T} variable, and a minimum energy ϵ to regulate the energy fraction z. These resolution parameters will play a double role. On the one hand they will produce finite cross sections and on the other hand they will allow us to distinguish between exclusive n jets and $n+1$

jets final states. In terms of these resolution parameters the cross section from equation 2.41 will be proportional to

$$\frac{\alpha_s}{2\pi}\log(\frac{p_{\mathrm{T}}^2}{Q_0}) \quad \text{and} \quad \frac{\alpha_s}{2\pi}\log(\frac{p_{\mathrm{T}}^2}{Q_0})\log(\frac{1}{\epsilon}), \tag{2.42}$$

where the single logarithm correspond to the collinear divergence only, and the double logarithm to a collinear and soft divergence.

We could be tempted to think that by applying this cutoff we would be loosing part of the cross section (for the $\sigma_{q\bar{q}g}$ case), because the full phase space integration region is not entirely covered. In fact, the cross section obtained for $\sigma_{q\bar{q}g}$ after the cuts ($p_{\mathrm{T}} < Q_0$ and $z < \epsilon$) must be added to the exclusive two-jet cross section, which together with the virtual terms $d\sigma^V_{q\bar{q}}$, will cancel the unwanted singularities, resulting in a final cross section free of singularities.

Universal factorization

We now return to equation 2.41. Although it refers to the $e\bar{e} \rightarrow q\bar{q}g$ process, the z dependence structure is "universal". It can be shown that a general σ_{n+g} case (where n stands for a given hard process) can be written, in the collinear limit, as a product of σ_n and an emission term. The emission factors are called Altarelli-Parisi splitting functions (31), and give us the branching probability as a function of the fraction of energy z, carried by the final parton (z can also be defined for example as the momentum fraction). They play a central role in the shower simulation. There are a total of three possible branchings: $q \rightarrow qg$, $g \rightarrow gg$ and $g \rightarrow q\bar{q}$. The respective splitting functions (spin averaged) are given by:

$$\begin{aligned} P_{q,qg}(z) &= C_F\frac{1+z^2}{1-z} && (2.43)\\ P_{q,qg}(z) &= C_A\left(\frac{z}{1-z}+\frac{1-z}{z}+z(1-z)\right) && (2.44)\\ P_{q,qg}(z) &= T_F\left(z^2+(1-z^2)\right), && (2.45)\end{aligned}$$

where $C_F = \frac{N_c^2-1}{2N_c}$, $C_A = N_c$ and $T_R = \frac{1}{2}$. A final comment about equation 2.41: besides transverse momentum, other kinematic variables, like the angle or parton virtuality, could be used as well. The criteria is that the kinematic dependence should be proportional to the branching angle. Currently, several parton shower simulators use different definitions, and the most common are:

$$\text{virtuality} \quad : \quad t = (k+l)^2 \sim E^2\theta^2 z(1-z) \tag{2.46}$$

$$\text{transverse momentum} \quad : \quad p_T^2 = l_T^2 \sim E^2\theta^2 z^2(1-z)^2 \tag{2.47}$$

$$\text{angular variable} \quad : \quad \theta^2 \tag{2.48}$$

As we can see, all of these three definitions depend on θ and obey

$$\frac{d\theta^2}{\theta^2} = \frac{dp_{\mathrm{T}}^2}{p_{\mathrm{T}}^2} = \frac{dt}{t}\,. \tag{2.49}$$

Soft divergences and angular ordering

Until now we have assumed a collinear approximation. However, we still have to deal with the cases where we face a soft singularity in a wide angle scenario. The treatment is similar to the collinear case. We have shown that the total $\sigma_{q\bar{q}g}$ cross section can be factorized into $\sigma_{q\bar{q}}$ times a gluon emission probability factor. In the soft emission case it can also be shown that the processes can be factorized in a similar way but only at the amplitude level. In fact, factorization is not possible after the amplitude is squared. It can be shown (see (28)) that, in a soft emission scenario, a $n+1$-parton distribution can be written as a function of n-parton through the relation:

$$d\sigma_{n+1} = d\sigma_n \frac{dE_g}{E_g}\frac{d\Omega}{2\pi}\frac{\alpha_S}{2\pi}\sum_{ij} C_{ij}W_{ij}, \tag{2.50}$$

where E_g is the emitted gluon energy, Ω the solid angle for the emitted gluon, C_{ij} a color factor that must be computed case by case, and W_{ij} the so-called *radiation function* given by:

$$W_{ij} = E_g^2 \frac{p_i.p_j}{(p_i.p_g)(p_j.p_g)} = \frac{1 - \cos\theta_{ij}}{(1 - \cos\theta_{ig})(1 - \cos\theta_{jg})}. \tag{2.51}$$

In equation 2.50 the sum runs over all partons pairs, which is a consequence of a non-negligible interference terms (the sum runs over all possible pair combinations from where the gluon can be radiated). For the $e\bar{e} \to q\bar{q}g$ process, the sum has one term only. In figure 2.5 we show the emission of a gluon from a quark with momentum p_1. The angle θ_{k1} is the angle between the emitted gluon and p_1, θ_{k2} is the equivalent angle for quark 2 with momentum p_2 and θ_{12} is the angle between p_1 and p_2. For the present case W_{ij} is given by:

$$W_{12} = \frac{1 - \cos\theta_{12}}{(1 - \cos\theta_{k1})(1 - \cos\theta_{k2})}. \tag{2.52}$$

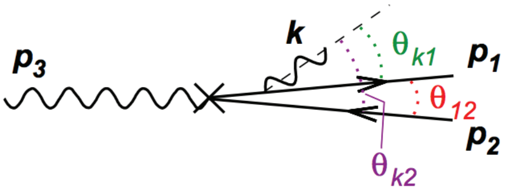

Figure 2.5: QCD coherence. The emission outside the cone of angle θ_{12} is suppressed.

We now analyse three case scenarios. A first one where $\theta_{k1} << \theta_{k2} \simeq \theta_{12}$, a second one where $\theta_{k2} << \theta_{k1} \simeq \theta_{12}$ and a third one with $\theta_{12} << \theta_{k1} \simeq \theta_{k2}$. By using $\cos\theta \sim 1 - \theta^2/2$ for small angles we obtain:

- $\theta_{k1} << \theta_{k2} \simeq \theta_{12} : W_{12} \propto \frac{1}{\theta_{k1}^2}$
- $\theta_{k2} << \theta_{k1} \simeq \theta_{12} : W_{12} \propto \frac{1}{\theta_{k2}^2}$
- $\theta_{12} << \theta_{k1} \simeq \theta_{k2} : W_{12} \propto \frac{\theta_{12}^2}{\theta_{k1}^2}$.

We can confirm the expected $1/\theta^2$ behaviour in the first two scenarios which is due to the collinear divergence. However, the same is not true for the third scenario. In this case, the W_{12} function is highly suppressed. Therefore, we can conclude that gluon emissions where the angle lies outside the cone drawn by the two partons momenta are suppressed (it can be shown that there is in fact no emission outside this cone). Note that the polar angle of the solid angles around p_1 and p_2 are equal to the angle between p_1 and p_2. This property is called "angular ordering" and can be generalised to any pair of partons. To sum up, it says that the emitted radiation from any pair of partons is limited to the volume produced by the sum of both solid angles drawn from each parton line (see figure 2.6 - the radiation is limited to the volume defined by the red and blue cones).

In conclusion, in a QCD showering all emitted radiation will be angular ordered, i.e., as the shower goes on, the radiation will be emitted at increasingly smaller angles. As we saw in the previous section, this ordering does not present a problem in the case the shower is simulated through the angle variable θ. However, if one uses the transverse momentum p_{T}, or the virtuality t, the angular ordering is not guaranteed and therefore a correction must be implemented.

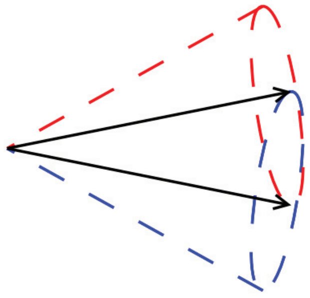

Figure 2.6: QCD soft gluon emission region.

2.4.3 General case

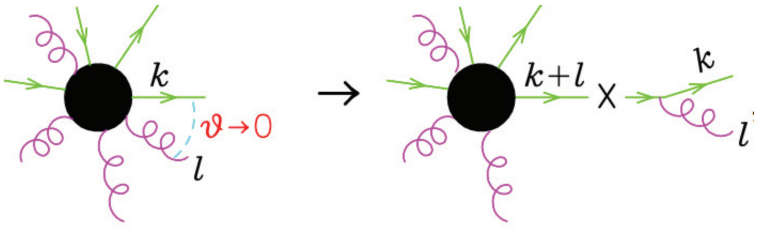

Figure 2.7: Collinear Factorization. From (32)

We are now ready to generalise the shower algorithm. In figure 2.7 we show a schematic diagram representing the factorization of a $n+1$-parton into a n-parton process radiating a gluon from one of the external legs. The procedure can be written

$$|M_{n+1}|^2 d\Phi_{n+1} \implies |M_n|^2 d\Phi_n \frac{\alpha_S}{2\pi}\frac{dt}{t}P_{q,qg}(z)dz\frac{d\phi}{2\pi}, \tag{2.53}$$

where M_j represents the respective l-parton squared amplitude. The variables t,z and ϕ describe the branching kinematics, and their definitions are the same as for the electron-positron example discussed above. Since in this case we are considering a gluon emission, the splitting function $P_{q,qg}(z)$ must be used. Finally, the phase space is defined as

$$d\Phi_n(P;p_1,...,p_2) = \delta^4(P - \sum_{i=1}^{n} p_i)\prod_{i=1}^{n}\frac{d^3p_i}{(2\pi)^3 2E_i}. \tag{2.54}$$

As we mentioned above, there are several ways to define the virtuality t (equalities shown in equations 2.46-2.48). This "virutality" controls the order of the branching cascade, creating an ordered shower with respect to t (or p_{T}^2 or θ). The parton shower simulation is performed by recursively applying a Markov-Chain type of algorithm, using the factorization shown in equation 2.53 , where in each step a new t is calculated. This is shown in figure 2.8.

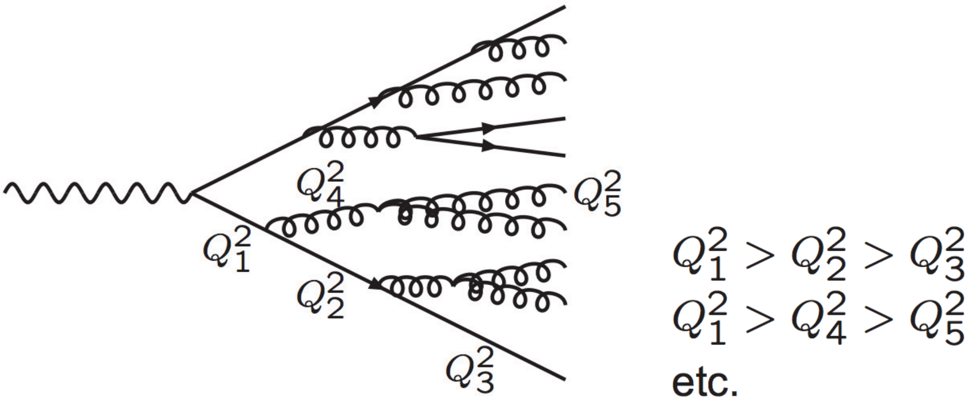

Figure 2.8: Q^2 ordered shower. From (33)

We also note that in order to introduce higher order corrections to gluon emissions we must consider a running coupling constant $\alpha_S(t)$, rather than a fixed one (34). As a consequence the final state configuration will be affected. Since $\alpha_S(t)$ increases as the scale gets lower, the probability of emission will increase as well, and therefore, as we approach the cut-off scale Q_0, more emissions will occur. Additionally, we must make sure that the cut-off Q_0 is above QCD scale, Λ_{QCD}. This follows from the fact that bellow Λ_{QCD}, α_S is above 1, which means that QCD can no longer be considered a perturbative theory.

Sudakov Factor

Let us now consider the probabilistic term from equation 2.53

$$dP_i = \frac{\alpha_S}{2\pi}\frac{dt}{t}P_{i,ij}(z)dz\frac{d\phi}{2\pi}. \tag{2.55}$$

It give us the probability of a gluon j being emitted from parton i, with "virtuality" between t and $t + dt$, for a given z and ϕ configuration. Now, together with this information, we must know the non-emission probability factor. This information is needed because the branching generation will be equivalent to a nuclear decay simulator, i.e., in order to describe an emission for a given time t', we need to know the decay probability for t' and the probability of no decay between the initial time t_0 and time t'. From unitary we have

$$P_{\text{no emission}}(t_1 > t > t_0) = 1 - P_{\text{emission}}(t_1 > t > t_0). \tag{2.56}$$

Using this expression we can calculate the total non emission probability (NE) as function of the emission probability (E). This is done by diving the t domain in infinitesimal segments:

$$\begin{aligned} P_{\text{NE}}(t_1 > t > t_0) &= \lim_{N\to\infty}\prod_{n=0}^{N-1}\left(1 - P_{\text{E}}(t_{n+1} > t > t_n)\right), t_{n+1} = \frac{t_1 - t_0}{N} && (2.57)\\ &= \exp\left(-\lim_{N\to\infty}\sum_{n=0}^{N-1} P_{\text{E}}(t_{n+1} > t > t_n)\right) && (2.58)\\ &= \exp\left(-\int_{t_0}^{t_1}\frac{dP_{\text{E}}(t)}{dt}dt\right). && (2.59) \end{aligned}$$

We then arrive to the general formula:

$$\Delta_i(t_1, t_0) = \exp\left(-\sum_{jl}\int_{t_0}^{t_1} dt\frac{\alpha_S(t)}{2\pi}\int dzP_{i,jl}(z)\right), \tag{2.60}$$

where azimuthal symmetry has been assumed, as well a sum over all possible emissions to account for other branching possibilities. This $\Delta(t_0, t_1)$ function is the so-called Sudakov form factor, and plays a central role in the shower simulation. It is the probability of non emissions between the scales t_1 and t_0. Once this information is included in the parton shower algorithm, we can claim that the final states generated are fully exclusive, rather than inclusive. They allow us to generate fixed multi-parton configurations, weighted according to the probability of no additional partons being present. This is a fundamental improvement, since the simulation of exclusive events from ME, at fixed-order, is constrained due to the known infra-red divergences. Additionally, with the use of the Sudakov form factor virtual corrections are actually being included. This is a direct result of unitary. The main idea is that an α_S order cross section is the sum of the virtual part, the non resolved one and resolved real emission. Unitarity implies this sum must be equal to 1. But again, and also because of unitary, the resolved real emission probability is equal to 1 minus the non emission probability, and therefore the sum of virtual and real unresolved terms is equal to the Sudakov factor. We should mention that this is only true in the collinear and soft approximation we are working in (designated by Leading Log (LL) approximation).

2.4.4 Final State Radiation

We now have all the tools to simulate the shower. We start by considering a phase space configuration weighted according to the n-parton Matrix Element (ME). The next step is to generate a branching from one of the external partons. For that a starting scale must be specified, which in equation 2.60 is referred to as t_1. Let us call this scale Q. The starting scale value is usually a debatable point since there are no analytical arguments predicting which scale should be chosen. The most usual choice is the one defined by the typical hard process scale. For example in the case of FCNC direct top production (final state with just a top quark in the hard parton process), which will be discuss in detail later, we choose $Q = M_{top}$. There is an heuristic argument that supports this approach. Suppose we start the shower in a much higher scale and therefore the first branching occurs also at a very high scale. It can happen that this configuration will be double counted from one originated in an external leg from a hard process that radiates a soft gluon. In such case, we could make a simple veto in order to correct this problem. However, it would be much better to veto the one with the hard emission, since the shower algorithm is built within the approximation of soft and collinear emissions. Therefore, it is simpler to prevent this to happen in first place by setting the starting scale equal to the scale of the hard scattering process.

Having defined the initial scale Q, we can now start the shower algorithm. Its main steps are:

1. Set $t_1 = Q$ (the starting scale);
2. Generate a uniform random number r with $0 < r < 1$ and solve the equation $r = \Delta_i(t_1, t)$ for t;
3. If $t \ < t_0$, the shower ends and no more emission occurs;
4. If $t \geq t_0$, the first branching scale has been found. From $P_{jl}(z)$, generate a z value, and from z the energies $E_j = zE_i$ and $E_l = (1-z)E_i$. The azimuthal angle is uniformly generated within the domain $[0, 2\pi]$, and the angle θ between partons j and l is obtained from the scale t, using equations 2.46-2.48;
5. Reconstruct the full momentum;
6. Set $t_1 = t$ for each of the final partons and go back to point 2.

The final scale t_0 will act here as the cut-off mentioned above and is needed to regularize singular regions as well as to include the detector resolution limit. This limit is usually defined to be of order 1 GeV, which is the typical minimum scale at which the radiation is no longer resolvable. As we have previously showed, this algorithm can reproduce, in a first approximation, higher order corrections of the full event. Moreover, it has the advantage of being computationally less expensive. This is a very important point because of the extremely high statistics needed to simulate the events.

After the shower the next simulation step is a process called hadronization. This is the phase where the final partons combine to form bound states, the hadrons. Until now there is no fundamental model on how hadronization occurs and therefore its simulation is based on phenomenological models adjusted from experimental data. The main reason for this ignorance is the fact that hadronization occurs at scale Λ_{QCD}, which prevent us to apply perturbative QCD.

Finally, we note that although these 4 steps seem quite simple to implement, there are some subtleties (mainly technical) that make the coding of the algorithm not so straightforward. For example, special attention must be paid in solving the equation in point 2 since it is not analytically solvable. Also, momentum-energy conservation implies that the branching mechanism has to be performed trough an off-shell particle. This brings an additional problem as the collinear approximation is based on on-shell (external) final state particles. Therefore, a momentum reshuffling has to be done at the end of the branching. There is no unique way to perform this reshuffling and depending on the parton showers generators, different recipes are applied.

2.4.5 Inital State Radiation

Until now we have considered radiation emitted from the final state partons only. This is called Final State Radiation (FSR). In order to simulate the real process one must also take into account radiation from the initial partons, known as Initial State Radiation (ISR). The simulation of this process is very similar to simulating the FSR. In ISR we must take into account the fact that the partons are originated from a hadron, with some associated PDF, and that the initial hard parton may itself have its origin in the QCD radiation. Therefore, in order to simulate this radiation process, we must simulate the entire chain, i.e., from the hadron to the hard process, with several possible branchings. We show an example in figure 2.9. The main difference between ISR from FSR is the fact that now

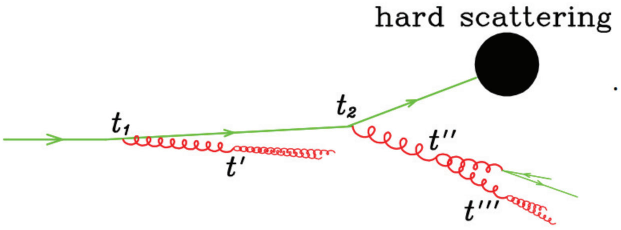

Figure 2.9: Initial State Radiation. From (32).

the incoming partons have space-like virtualities, i.e., $t_i = -q_i^2$, with increasing values towards the hard process. This is shown in figure 2.9 where $t_1, t_2 < 0$ and $t_2 > t_1$. Simulating ISR following the FSR algorithm would mean to begin from the colliding hadron and to numerically run all possible scale configurations such that, after several branchings, we would end up with an incoming parton with hard scale $t_{final} = -Q^2$. Obviously, this would be a very computationally expensive task. To solve this problem, shower simulators invert the process and simulate ISR originated from the hard process until the hadron scale is reached. As in the FSR case, this scale is usually set to $t_0 \sim 1$ GeV. This is called *backward evolution*. The algorithm is very similar to the FSR one, with the difference that now we consider that the colliding parton did not originate from the hadron's "parton sea" but rather from a previous QCD radiation. The first emission probability must then take into account three terms: the non-emission probability from the starting scale t_1 to the splitting scale t', the branching probability of parton i to be radiated from some parton j at the scale t', and the probability of extracting parton j from the "quark sea" with scale t'. Putting everything together we get

$$dP_{first} = \sum_j f_j^{(h)}(z, t') \frac{\alpha_S(t')}{2\pi} P_{ij}(x/z) \Delta_i(t_1, t') \frac{dt_1}{t_1} \frac{dz}{z} \frac{d\phi}{2\pi}, \tag{2.61}$$

where $f_j^{(h)}$ is the PDF of parton j, which is radiated the colliding parton i; P_{ij} is the splitting function for the branching $j \to i$, and Δ_i the Sudakov factor. In order to find the first branching scale, we must know how this probability evolves with t'. After some algebra (see (32)) this evolution can be written as:

$$\frac{dP_{first}}{dt'} = \frac{\partial}{\partial t'}[f_i^{(h)}(x,t')\Delta_i(t_1,t')], \tag{2.62}$$

which means that in respect to the branching scale t', the product $f_i^{(h)}(x,t')\Delta_i(t,t')$ as a direct correspondence in respect to the first branching probability. Therefore, in order to find the first emission one just had to solve the equation

$$r = \frac{f_i^{(h)}(t',x)\Delta(t,t')}{f_i^{(h)}(t,x)} \tag{2.63}$$

for t' ,where r is a uniform random number within the domain $0 < r < 1$. We note that the denominator was introduced in order to normalize the equation for the case where $t = t'$. Apart from this step, the ISR algorithm is equivalent to the FSR one. We also note that the radiation emitted can originate additional radiation and therefore a shower simulation must be performed starting from these partons. Since they are now final state partons, this simulation must use the FSR procedure.

2.4.6 Matching

In the previous sections we discussed two different approaches to simulate the final state events in a collider. In the first one the full matrix element is used and in the other a parton shower. The later was introduced for two main reasons. First, to calculate the ME for a multi-final parton state is an almost impossible task; second, even if this was possible, ME fixed-order calculations always contain unwanted divergences beyond leading order. The use of parton showers solved this problem, but it assumes however a collinear and soft radiation approximation. Consequently, event simulation will be characterised by a lack of precision in the hard and wide angle jet regions. This problem can be avoided by using the full ME element, since the ME contain the full kinematics information. Also, the ME would always be preferable because quantum interferences are included by construction and are not included in the PS. However, when PS are used the divergent logarithms equivalent to the ones in equation 2.42 are reproduced, which does not happen if one had used ME only. Also, realistic multiple final state partons, which in the end give origin to the observed jets can only be simulated via PS. Therefore, one must conclude that a good simulation is one that combines both approaches: in the collinear and soft regions the events are simulated through a PS and in the hard and wide angle regions they are simulated through the correspondent ME. The process of joining these two methods is known as *Matching*.

One of the first issues that must be taken into consideration, when *Matching* is implement in a MC generator, is the *double counting* problem. Back to the $e\bar{e} \rightarrow \gamma \rightarrow q\bar{q}$ example, we can easily see that the real radiation correction (figure 2.4) can be simulated, within specific limits, from either of the two methods:

- through the use of the exact Matrix-Element,
- through a parton shower mechanism, where the real radiation would be the first emission.

Therefore, if *Matching* is performed without any considerations regarding what phase space is being covered, there is a chance to generate several events with the same kinematic configuration. This overestimation is known as the *double counting* problem. In order to solve this problem one must separate the final phase space in two regions where each region undergoes with a different type of simulation. The collinear/soft region will be best simulated by using a PS while the hard and wide angle by using the ME. This phase space separation can be done by defining one or more resolution parameters, depending on how many final state particles we will be working with. For example, the MEtop generator, to be discussed later, performs a merging between a $2 \rightarrow 1$ and a $2 \rightarrow 2$ processes, where only a single resolution parameters is needed (in our case the top p_{T}). The matching is then usually done in an event-by-event basis, so that in case one event is generated in a "forbidden" phase space region, an event veto will be imposed. In section 7.4 a more detailed explanation will be given about which matching procedure is used in the MEtop generator.

2.5 Markov Chain Monte Carlo

2.5.1 Introduction

As we will see in the next chapter, the main theoretical background to the FCNC studies dealt with this thesis is a framework where we assume a phenomenological approach through effective Lagrangians. A high number of effective operators are considered in order to probe physics beyond the SM. In case one wants to use the available experimental data to inquire which operator or set of operators can best describe the measurable observables, one needs statistical tools to help us discriminate between operators or/and to point us out which operators perform better. A common method to deal with this problem is to use a Bayesian approach, where ”several models” are proposed and tested, through fits to the most updated experimental data. A note must be added about these so-called ”models”. Technically, they are not theoretical models, since we will always be working within the effective Lagrangians approach. In this framework, the operators will be parametrized through dimensional coupling constants, that will dictate the ”strength” of the new interaction introduced. Therefore, this fitting will be done by adjusting the values of the parameters to the observable data.

2.5.2 The Bayesian approach

Contrary to the Frequentist paradigm, where the probabilities are interpreted as a simple consequence of the outcome data, the Bayesian method assumes that it is possible to define an absolute concept of probability for some specific outcome. This means that one can in principle calculate the probability of some specific model to be correct, i.e., to reproduce some data from our model, as well to determine the probability to obtain some data from a specific model. By using these two concepts, the Bayes’ theorem can be written as

$$p(m|d) = \frac{L(d|m)p(m)}{\int L(d|m')dm'}, \tag{2.64}$$

where $p(m|d)$ is the probability of model m being correct in case data d is measured - this is called the posterior probability -, $L(d|m)$ is the likelihood distribution which give us the probability for d to be reproduced given a model m, and $p(m)$ is the referred probability of model m to be correct, which is named the prior probability. Clearly, it is very unlikely that one can calculate the prior probability $p(m)$, as well as to be able to integrate the likelihood for all models, $L(d|m)$. Nevertheless, since we are interested in comparing "several models" and not in studying a single specific model, we can take the ratio of the posterior probabilities of two hypothetical models:

$$\frac{p(m_1|d)}{p(m_2|d)} = \frac{L(d|m_1)}{L(d|m_2)}, \tag{2.65}$$

where we have assumed that the prior probabilities of all models are equal, that is $p(m_1) = p(m_2)$. Although this assumption seems, at first, quite strong, remember that we will not analyse pure physical models, but rather fit the best set of effective operators to the experimental data, through the respective parameter value variation. Therefore, if we sample this set of parameters search, using flat random numbers, we can interpret models m_1 and m_2 has having equal prior probabilities. This ratio is usually called *Bayes factor* and by using some specific set of experimental data it will tell us which model performs better in fitting that same data.

2.5.3 Markov Chain Monte Carlo

The Markov Chain Monte Carlo (MCMC) approach is based on the last section considerations. We aim to find the best possible fit by successively testing the possible models, with the value of *Bayes factor* as guidance and a pre-defined set of physical observables that will play the *data* role. The search will be performed iteratively, where in each cycle the *Bayes factor* is calculated, and the parameter phase point saved. A chain is then built as the iteration is performed and a map of the full phase space can then be extracted. As we concluded in the previous section, the *Bayes factor* is calculated by taking the ratio of the Likelihood of two competing models. When performing a MCMC, we usually assume that the

Likelihood for each physical observable obeys to a Gaussian distribution:

$$L^j(x_i) = \exp(-\frac{(\mathcal{O}_j(x_i) - \mathcal{O}_j^{exp})^2}{\sigma_j^2}), \tag{2.66}$$

where $\mathcal{O}_j(x_i)$ is the expected observable value for the parameter vector $x_i = \{\alpha_1, ..., \alpha_n\}$, α_i measures the corresponding effective operator, $\mathcal{O}_j^{exp}$ is the experimental observable and σ_j is the correspondent experimental error. The total Likelihood is then the product of all Likelihood functions:

$$L(x_i) = \exp(\sum_j \frac{-(\mathcal{O}_j(x_i) - \mathcal{O}_j^{exp})^2}{\sigma_j^2}). \tag{2.67}$$

We note that the exponential factor is the classical Chi-square factor.

The chain is then constructed from the Metropolis-Hastings algorithm:

1. Generate a flat random starting point x_0 and define a frequency variable $f_0 = 1$ ($f_i = 1$ for the subsequent cases). In the work presented in chapter 6 we set the domain $\alpha_i = [-10, 10]$.

2. Calculate its Likelihood using equation 2.67.

3. Generate an adjacent point x_i starting from the previous x_{i-1}. At this step a generation distribution must be defined. We have used a Gaussian centred at the departing point (x_i), with a 0.1 variance.

4. Calculate the new Likelihood value.

5. Generate an uniformly distributed random number between 0 and 1, and evaluate the inequality condition:

$$rand() < \frac{L(x_{i+1})}{L(x_i)}. \tag{2.68}$$

6. if **True**, save f_i, x_i, the respective Likelihood and physical observables. Set $x_i = x_{i+1}$ and $f_i = 1$. Return to step 3 or stop if the number of iterations has reached its maximum.

7. if **False**, set $f_i = f_i + 1$ and return to step 3 or stop if the number of iterations has reached its maximum.

The variable f_i is used to save the number of times the chain was "stuck" in some possible local maximum. It will also work as a weight, when plotting the chain results. Finally, from the saved chains one can obtain the information needed to perform the fit analysis, and we can extract the maximum likelihood value, which will indicate the best fit scenario, and more important, will give us all the probability distribution and correlations between variables.

3

The Standard Model

3.1 Introduction

The Standard Model (SM) is a fundamental model describing the dynamics of the subatomic particle interactions. It is considered the most reliable description of Nature, and up to now has shown an extraordinary agreement with most of the available experimental data (35). There are however a number of experimental results that the SM fails to describe. The most relevant issues are the baryon asymmetry, the dark matter problem and the neutrino masses. Therefore, it is clear that an extension of the SM is needed and we expect the LHC will give us some hint on new lines of research that could point us to the right extension of the SM.

The SM is a mathematical model within a Quantum Field Theory (QFT) framework and therefore each subatomic particle is represented by a quantum field that obey the quantum interpretation of matter in a four dimensional space-time. Additionally, the respective interactions are written by a Lagrangian density and the dynamics is described by the well-known Euler-Lagrange equations of motion. The final form of this Lagrangian is obtained by the introduction of global and local gauge symmetries making the SM a *gauge theory*. Regarding global invariance, the total Lagrangian is forced to be invariant under the Poincaré group of transformations. This is a direct consequence of the translational and rotational symmetries, together with the fundamental principle of invariance between inertial references frames.

The SM Lagrangian density is then built to be invariant under local gauge translations. Imposing local symmetries imply specific transformation laws for the matter fields which in turn forces the introduction of the so-called gauge fields (the interaction mediators) in order to preserve the symmetries of the Lagrangian. These new fields, the gauge *bosons*, mediate the interactions between matter. The SM gauge symmetries can be written as a continuous group $SU(3) \times SU(2) \times U(1)$. The group $SU(2) \times U(1)$ gives origin to the electroweak interactions which unifies electromagnetism and the weak interactions. The $SU(3)$ group describes the strong interaction and is usually treated as a separate model known as Quantum Chromodynamics (QCD).

The SM describes three of the four known fundamental forces: electromagnetic, weak and strong; being gravity the remaining missing part. Although the first two are now unified in the so-called electroweak interaction, a search for a unified model with the strong interaction is still a subject of research.

3.2 Gauge Theories

We begin with a short account of gauge theories. In this formalism, the physical model is a field theory described by a Lagrangian density, which has been forced to be invariant under a specific continuous group of local transformation. To show how this mechanism works we start with a simple example of a scalar field (ϕ) theory, with mass m. The free Lagrangian for such a field is given by

$$\mathcal{L} = (\partial^\mu \phi_i)^\dagger \partial_\mu \phi_i - m^2 \phi_i^\dagger \phi_i \tag{3.1}$$

where $i = 1, 2, ..., n$, with n the total number of components that ϕ may have. We now impose that the scalar fields are transformed by a dimension N representation $V(x)$, of an internal symmetry G

$$\phi(x) \to \phi'(x) = V(x)\phi \tag{3.2}$$

with $V(x)V^\dagger(x) = 1$. In case of infinitesimal phase transformations, $V(x)$ can be expanded into

$$V(x) = 1 + i\alpha^a(x)t^a \tag{3.3}$$

where t^a are the generators of the group G, and α^a are real parameters. Due to unitarity and the defining representation, the group generators obey the commutation relations

$$[t^a, t^b] = if^{abc}t^c \tag{3.4}$$

$$Tr[t^at^b] = \frac{\delta^{ab}}{2} \tag{3.5}$$

where if^{abc} are the group structure constants. We note that in this case the generators don't commute which means we are dealing a non-abelian gauge theory. The weak and strong interaction are non-abelian while electromagnetism is described by the abelian $U(1)$ group.

Our main objective is to have an invariant Lagrangian under the transformation V. However, if we apply this transformation to equation (3.1), only the second term is invariant

$$\phi^\dagger\phi \to \phi^\dagger\delta V^\dagger\delta V\phi = \phi^\dagger\phi, \tag{3.6}$$

where we have neglected second order terms. Ensuring that the kinematic term of (3.1) is also invariant lead us to replace ∂_μ by the covariant derivative D_μ shown in eq. (3.7) which transforms according to equation (3.8)

$$D_\mu = \partial_\mu - igA_\mu^a t^a \tag{3.7}$$

$$(D_\mu\phi)' = V(D_\mu\phi). \tag{3.8}$$

In this covariant derivative a new field is introduced, namely A_μ. This is the gauge field and it will be responsible for making the total Lagrangian invariant under the transformation. The gauge field transformation law follows directly from equation (3.8) and is given by

$$A^a_\mu \to A^a_\mu - \frac{1}{g}(\partial_\mu \alpha^a) + f^{abc}\alpha^b A^c_\mu. \tag{3.9}$$

With the introduction of the new gauge vector field we can now write the invariant Lagrangian as

$$\mathcal{L} = (D^\mu \phi)^\dagger (D_\mu \phi) - m^2 \phi^\dagger \phi. \tag{3.10}$$

Although the full Lagrangian is now invariant, nothing prevent us from introduction further gauge invariant terms built with the new gauge field A^a_μ. This can be done by introducing a new quantity $[D_\mu, D_\nu]$, that from (3.8) transforms as

$$[D_\mu, D_\nu] \to V(x)[D_\mu, D_\nu]\phi. \tag{3.11}$$

Using the definition of the covariant derivative D_μ we then have

$$\begin{aligned}[D_\mu, D_\nu]\phi &= -ig\Big[\partial_\mu A^a_\nu - \partial^a_\nu + g f^{abc} A^b_\mu A^c_\nu\Big] t^a \phi \\ &= -ig F^a_{\mu\nu} t^a \phi \end{aligned} \tag{3.12}$$

with $F^a_{\mu\nu}$ given by equation (3.13). This is called field strength tensor and is the analogue to the electromagnetic field tensor.

$$F^a_{\mu\nu} = \partial_\mu A^a_\nu - \partial_\nu A^a_\mu + g f^{abc} A^b_\mu A^c_\nu. \tag{3.13}$$

From $F^a_{\mu\nu}$ we can build the quantity $\frac{1}{4} F^a_{\mu\nu} F^{a\mu\nu}$, which is a gauge-invariant term dependent only on the gauge field, A^a_μ. We redefine the Lagrangian to:

$$\mathcal{L} = (D^\mu \phi)^\dagger (D_\mu \phi) - m^2 \phi^\dagger \phi - \frac{1}{4} F^a_{\mu\nu} F^{a\mu\nu}. \tag{3.14}$$

We have just laid out the guiding principles of how to build a gauge theory. This is the starting point and it's juts enough to allow us to move on to the next section where the Lagrangian for the electroweak and strong interactions will be introduced.

3.3 Electroweak interaction

Historically, the final version of the unified electroweak theory is attributed to the work of three authors: Glashow (36), Salam (37) and Weinberg (38). This fundamental theory incorporates two interactions. One is the classical electromagnetic interaction known since the 19^{th} century and described by Maxwell's equations; the second is the weak force which was discovered as a consequence of *beta decay* studies. Theoretically, the weak force was originally described as a four-fermion interaction in the context of an effective formalism (we will address this mechanism in more detail).

Today, the electroweak interaction is understood within the context of gauge symmetries as described in the previous section. Unification is in some sense attained by the introduction of one semisimple group $SU(2) \times U(1)$, where $SU(2)$ is the special unitary group of dimension 2, and $U(1)$ the group of all 1×1 unitary matrices. The $SU(2)$ generators can be represented by the matrices $\tau^i = \sigma^i/2$, where σ^i are the Pauli matrices. The $SU(2)$ charge is called isospin, I, while the $U(1)$ charge is named hypercharge, Y. The $SU(2)$ generators commutation rules are given by

$$[\tau^i, \tau^j] = i\epsilon^{ijk}\tau^k \tag{3.15}$$

$$[\tau^i, Y] = 0. \tag{3.16}$$

The full $SU(2) \times U(1)$ invariant Lagrangian has the form

$$\mathcal{L} = \mathcal{L}_G + \mathcal{L}_F + \mathcal{L}_H + \mathcal{L}_M. \tag{3.17}$$

The first term in equation (3.17), $\mathcal{L}_G$, is the Yang-Mills Lagrangian, the equivalent to what was presented in equation 83.13) for the $U(1)$ case. These are the gauge boson kinematic terms together with the self-interaction ones which arise because the group is non-Abelian. It can be written as

$$\mathcal{L}_G = -\frac{1}{4}F^i_{\mu\nu}(W)F^{i,\mu\nu}(W) - \frac{1}{4}F_{\mu\nu}(B)F^{\mu\nu}(B), \tag{3.18}$$

with

$$F^i_{\mu\nu}(W) = \partial_\mu W^i_\nu - \partial_\nu W^i_\mu + g\epsilon^{ijk}W^j_\mu W^k_\nu \tag{3.19}$$

$$F_{\mu\nu}(B) = \partial_\mu B_\nu - \partial_\nu B_\mu, \tag{3.20}$$

where $W^i_\mu = \{W^1_\mu, W^2_\mu, W^3_\mu\}$ are the $SU(2)$ gauge fields while B_μ is the $U(1)$ field. Their corresponding infinitesimal gauge transformations are given by

$$\delta B_\mu = \partial_\mu \theta \tag{3.21}$$

$$\delta W^i_\mu = \partial_\mu \theta^i - g\epsilon^{ijk}\theta^j W^k_\mu = D^{ij}_\mu \theta^j, \tag{3.22}$$

where g is the $SU(2)$ gauge coupling constant, and θ and θ^i are real parameters.

In order to describe Nature with the $SU(2) \times U(1)$ gauge group, the matter (spin 1/2) fields have to decompose in chirality eigenstates. These eigenstates, the left and right components of the spinor, are built from the chirality operators γ_L and γ_R such that

$$f_R = \gamma_R f = \frac{1}{2}(1+\gamma_5)f \tag{3.23}$$

$$f_L = \gamma_L f = \frac{1}{2}(1-\gamma_5)f \tag{3.24}$$

where f is a spinor field. The reason for this decomposition is that the electroweak interactions do not conserve chirality. The left chirality components are vectors under $SU(2)$ while the right components are scalars under the same gauge group. That is, the right component has zero weak quantum number (weak

Isospin $I = 0$). In this context fermions are organised as shown in the table 3.1. The index i runs over the three known generations of quarks and leptons. We note that in the lepton family the neutrinos exist only as left-handed (we are treating the neutrinos as massless particles). Finally, there is mixing between the three quark generations which is accounted for by the introduction of the Cabibbo-Kobayashi-Maskawa matrix V_{CKM}, to be described below.

Quarks	$q^i_L = \binom{u^i_L}{d'^i_L}$, $d'^i_L = V_{CKM} d_L$	left-handed quark doublets
	$u^i_R \quad d^i_R$	right-handed quark singlets
Leptons	$l^i_L = \binom{\nu^i_L}{e^i_L}$	left-handed lepton doublets
	e^i_R	right-handed lepton singlets

Table 3.1: Fermions families. The subscript i runs over three generations.

The second term in equation (3.17), $\mathcal{L}_F$, corresponds to the fermion's kinetic terms and their interactions with the gauge fields. Taking into account the previous chirality description, we can write $\mathcal{L}_F$ as

$$\mathcal{L}_F = i\bar{l}^i_L D_L l^i_L + i\bar{e}^i_R D_R e^i_R + i\bar{q}^i_L D_L q^i_L + i\bar{u}^i_R D_R u^i_R + i\bar{d}^i_R D_R d^i_R, \tag{3.25}$$

where the corresponding covariant derivatives and the fermion transformation rules are given by

$$D_{L,\mu} = \partial_\mu - ig\frac{\sigma^i}{2}W^i_\mu - ig'\frac{Y}{2}B_\mu \tag{3.26}$$

$$D_{R,\mu} = \partial_\mu - ig'\frac{Y}{2}B_\mu \tag{3.27}$$

$$\delta\psi = (ig'\frac{Y}{2}\theta(x) + ig\frac{\sigma^i}{2}\theta^i(x))\psi, \tag{3.28}$$

where g' is the $U(1)$ gauge coupling constant. The charge operator is defined by the relation $Q = I_3 + Y/2$, where I_3 it's one of third isospin components.

So far the Lagrangian written in equations (3.18) and (3.25) has no mass terms. The next step is to introduce the Lagrangian terms that give a particle's mass. In the previous section a mass term was introduced in equation (3.1), with the form $m^2\phi^\dagger\phi$ and therefore one would be tempted to apply the recipe here. However, including mass terms int the same way would explicitly break the $SU(2)$ gauge symmetry. This was a known problem for a long time and it was solved by the introduction of the so-called Higgs mechanism. In this mechanism the fermions as well the gauge bosons mass terms are not present in the initial Lagrangian but rather "hidden" in newly introduced invariant terms built with a new postulated scalar field, the Higgs boson. Masses will be generated when this field acquires a non-zero vacuum expectation value which will result in the spontaneous breaking of the $SU(2) \times U(1)$ symmetry to the electromagnetic $U(1)$ symmetry. With this mechanism the theory remains manifestly locally invariant and the symmetry is broken at lower energies only.

The Higgs field is a complex $SU(2)$ doublet, with hypercharge $Y = 1$, that can be written as

$$\Phi = \begin{pmatrix} \phi^+ \\ \phi^0 \end{pmatrix} \equiv \begin{pmatrix} \frac{1}{\sqrt{2}}(\phi_1 + i\phi_2) \\ \frac{1}{\sqrt{2}}(\phi_3 + i\phi_4) \end{pmatrix} \tag{3.29}$$

and is incorporated in the total Lagrangian through the insertion of a kinematical and a potential term

$$\mathcal{L}_H = (D_{L,\mu}\Phi)^\dagger(D_L^\mu\Phi) - V(\Phi), \tag{3.30}$$

where the potential is given by

$$V(\Phi) = \mu^2\Phi^\dagger\Phi + \lambda(\Phi^\dagger\Phi)^2. \tag{3.31}$$

In case $\mu^2 < 0$, the minimum of the potential Φ is given by

$$(\Phi^\dagger\Phi)_{min} = -\frac{2\mu^2}{\lambda} = \frac{v^2}{2}. \tag{3.32}$$

As a consequence, the potential develops a vacuum expectation value (vev), which is given by:

$$< \Phi >= \begin{pmatrix} 0 \\ \frac{v}{\sqrt{2}} \end{pmatrix}, \tag{3.33}$$

where $v \approx 246$ GeV. All calculations will now be performed perturbatively from the final Lagrangian density. This mean that the particle spectrum as well as all interactions will be described by an expansion around the minimum energy. This expansion has to be done with respect to the vev shown in equation (3.33). The minimum condition can be written as

$$(\phi_1^2 + \phi_2^2 + \phi_3^2 + \phi_4^2) = v^2, \tag{3.34}$$

which describes a 3-dimensional surface with an infinite number of minima. To implement the perturbative expansion around a minimum implies the choice of a specific direction in the fields space. This choice is the spontaneous breaking of the symmetry. The point which is usually chosen is

$$\phi_1 = \phi_2 = \phi_4 = 0 \quad , \quad \phi_3^2 = v^2. \tag{3.35}$$

Around this point the expansion is written as

$$\Phi = \frac{1}{\sqrt{2}} \begin{pmatrix} \theta_2 + i\theta_1 \\ v + h(x) - i\theta_3 \end{pmatrix}, \tag{3.36}$$

where $h(x)$ is the Higgs field and θ_i are the Goldstone bosons. These are non-physical fields that arise whenever a global symmetry is broken (Golsdstone's theorem). They can be removed by a judicious choice of the gauge we will be working in. In particular, choosing the unitary gauge allow us to write the field expansion as

$$\Phi = \frac{1}{\sqrt{2}} \begin{pmatrix} 0 \\ v + h(x) \end{pmatrix}. \tag{3.37}$$

Replacing this field into equation (3.30), and considering only the terms that will originate the gauge bosons masses, we have

$$\begin{aligned} |(-ig\frac{\sigma^i}{2}W_\mu^i - i\frac{g'}{2}B_\mu)\Phi|^2 &= \frac{1}{8}(vg)^2[(W_\mu^1)^2 + (W_\mu^2)^2] && (3.38) \\ &+ \frac{1}{8}(g'B_\mu - gW_\mu^3)(g'B^\mu - gW^{3,\mu}). && (3.39) \end{aligned}$$

At this point it is convenient to diagonalize the mass matrix, so that we can explicitly obtain the mass states

$$W^{\pm}_{\mu} = \frac{1}{\sqrt{2}}(W^1_{\mu} \mp W^2_{\mu}) \quad , \quad M_W = \frac{gv}{2} \tag{3.40}$$

$$Z_{\mu} = \frac{1}{g^2 + g'^2}(gW^3_{\mu} + g'B_{\mu}) \quad , \quad M_Z = \frac{1}{2}\sqrt{(g^2 + g'^2)\,v} \tag{3.41}$$

$$A_{\mu} = \frac{1}{\sqrt{g^2 + g'^2}}(g'W^3_{\mu} + gB_{\mu}) \quad , \quad M_A = 0, \tag{3.42}$$

where $W^{\pm}_{\mu}$ and Z_{μ} are the gauge bosons mediators of the weak interaction and A_{μ} is the photon. The rotation from the group eigenstates to the mass eigenstates of the neutral bosons is usually written as

$$\begin{pmatrix} A_{\mu} \\ Z_{\mu} \end{pmatrix} = \begin{pmatrix} \cos\theta_W & \sin\theta_W \\ -\sin\theta_W & \cos\theta_W \end{pmatrix} \begin{pmatrix} B_{\mu} \\ W^3_{\mu} \end{pmatrix}, \tag{3.43}$$

where θ_W is the *weak mixing angle* defined by

$$\cos\theta_W = \frac{M_W}{M_Z}\,. \tag{3.44}$$

The remaining terms in this Lagrangian will give origin to the Higgs mass as well as to its interactions with the gauge bosons.

The fermionic masses arise from a similar mechanism. This is the fourth term, $\mathcal{L}_M$, in equation (3.17), and is called Yukawa Lagrangian

$$\mathcal{L}_M = -y_{e,ij}\bar{l}^i_L \Phi e^j_R - y_{d,ij}\bar{q}^i_L \Phi d^j_R - y_{u,ij}\bar{q}^i_L (i\sigma^2\Phi) u^j_R + h.c., \tag{3.45}$$

where y are the Yukawa matrices. We have shown that the gauge boson masses are just a consequence of having a non-zero vev. In the fermion case the masses are generated by its interaction with the Higgs field.

We will now discuss the appearance of the CKM matrix in the weak interactions. Equation (3.45) suggests that quark generation mixing could occur (in principle also lepton mixing). Let us concentrate on the mass terms only. In order to obtain the mass terms we have to rotate the fermion fields from the gauge basis to the mass basis. In other words we have to reduce the Yukawa matrix into a diagonal form. The diagonalization procedure can be written as

$$y_{u,d} \rightarrow (U^{L,R})^{-1}_{u,d} y U^{L,R}_{u,d} \; = D_{u,d} \tag{3.46}$$

where u and d refer to up and down type fermion respectively and L, R are chirality indices. This means we need a total of four unitary matrices to diagonalize the quark terms. Back to equation (3.45), we then have, for example, for the second term

$$y_{d,ij}\bar{q}^i_L \Phi d^j_R \rightarrow \bar{d}^i_L (U^{-1})_{ij} y_{d,jk} (U)_{kl} d^l_R \frac{v+h}{\sqrt{2}} \tag{3.47}$$

$$= D_{ii} \bar{d}^i_L d^i_R \frac{v+h}{\sqrt{2}}, \tag{3.48}$$

which when summed with the hermitian conjugate term originates the down quark mass terms. Note that the matrix that diagonalizes the masses is the same that diagonalizes the Higgs field. Therefore the neutral interactions are flavour diagonal and that is why FCNC are highly suppressed in the SM. Now, this rotation has a different effect in the charged sector. It is in fact this rotation that originates the CKM matrix. Back to the Lagrangian term $\mathcal{L}_F$, written in equation (3.25), and considering only the charged sector we obtain

$$i\bar{q}^i_L D_L q^i_L \rightarrow \frac{-g}{\sqrt{2}} W^+_\mu \bar{u}^i_L \gamma^\mu d^i_L \tag{3.49}$$

$$\rightarrow \frac{-g}{\sqrt{2}} W^+_\mu \bar{u}^i (U^L_u)^\dagger \gamma^\mu \gamma_L (U^L_d d^i) \tag{3.50}$$

$$= \frac{-g}{\sqrt{2}} W^+_\mu \bar{u}^i \gamma^\mu \gamma_L V_{ij} d_j, \tag{3.51}$$

where i and j run over the quark generations. As mentioned above, V_{ij} is the

CKM matrix and it results in:

$$V_{CKM} \equiv (U_L^u)^\dagger U_L^d = \begin{pmatrix} V_{ud} & V_{us} & V_{ub} \\ V_{cd} & V_{cs} & V_{cb} \\ V_{td} & V_{ts} & V_{tb} \end{pmatrix} . \tag{3.52}$$

As mentioned above, its presence will result in quark mixing, namely Flavour Changing Currents (FCC), mediated by the gauge boson $W_\mu^\pm$. In principle this mixing could be observed in the lepton families as well. However, the rotation matrices we used to construct the CKM matrix would depend on the neutrino masses which from today's measurements are extremely low (for a long time they were actually thought to be zero) which makes the mixing extremely small.

We end this section with a short comment about gauge fixing and Faddeev-Popov (FP) ghosts. At the quantum level two more pieces of the Lagrangian should be included, namely the gauge fixing Lagrangian and FP Lagrangian. The gauge fixing Lagrangian has to be introduced to define the gauge we will be working in. The same happens in ordinary electromagnetism. We define a four-component field for the photon while we know that the photon has only two degrees of freedom. Due to this freedom the path integral formulation is ill-defined. Faddeev and Popov have devised a method to solve the problem by introducing unphysical particles called ghosts. These particles can only appear inside loops and allow for a consistent way of performing perturbation theory using the Feynman diagramatic approach.

3.4 Quantum Chromodynamics

Quantum Chromodynamics (QCD) is the gauge theory that describes the strong force. The strong force acts between quarks only and is mediated through a gauge boson named *gluon*. It is the force responsible for baryons and mesons binding, like for example the proton or the Kaon. Theoretically, this interaction is described by a gauge theory along the same lines of the electroweak interaction.

The QCD Lagrangian is invariant under the group $SU(3)$ and is given by

$$\mathcal{L}_{QCD} = \bar{\psi}(i\gamma^{\mu} D_{\mu} - m)\psi + \frac{1}{4} G^{a}_{\mu\nu} G^{a,\mu\nu}, \tag{3.53}$$

where the covariant derivative and the gluon field strength have the form

$$D_{\mu} = \partial_{\mu} + i g_s \frac{\lambda^a}{2} G^{\mu}_{a} \tag{3.54}$$

$$G^{a}_{\mu\nu} = \partial_{\mu} G^{a}_{\nu} - \partial_{\nu} G^{a}_{\mu} - g_s f_{abc} G^{b}_{\mu} G^{b}_{\nu}. \tag{3.55}$$

where λ^a are the group generators, also known as Gell-Mann matrices, which obey the following commutation relations

$$[t^a, t^n] = i f_{abc} t^c \quad , \quad t^a = \frac{\lambda^a}{2}, \tag{3.56}$$

and f_{abc} are the group structure constants. Besides being characterised by the usual quantum numbers like charge or spin, the quarks have now a new quantum number. This new quantum number was suggested by the Δ^{++} baryon which is made of three u quarks resulting in a $J^P = \frac{3}{2}^{+}$ state. This would violate Pauli's exclusion principle since the interchange of two quarks would not be anti-symmetric. As a consequence a new degree of freedom, the *colour* quantum number, was proposed. Each quark has one in a total of three colours: red, green or blue. The quark colour is a *colour charge* of $SU(3)$ in much the same sense as the electric charge is charge of the electromagnetic $U(1)$. Also, just like there are positive and negative electric charges, anti-quarks have anti-colour charge: anti-red, anti-green and anti-blue.

In the context of group symmetries, the quark fields are then described as vectors in a 3-dimensional fundamental representation of the gauge group $SU(3)$ and the antiquarks are in the complex conjugate representation. The gauge field G^{a}_{μ} is said to be in the adjoint representation of $SU(3)$ which is an octet (a total of eight fields) where each one carries a combination of one colour and one anti-coulor charge.

An interesting fact about QCD is that up to now only stable colour singlets have been observed. This means that no free quarks or gluons were ever observed but rather composite states like baryons or mesons. This is a unique characteristic of QCD and is due to a property called *colour confinement*. This effect is a direct result of the peculiar behaviour of the strong coupling constant with the system energy. Calculating its dependence with the energy scale, Q, we obtain

$$\alpha_s(Q) \sim \frac{1}{b_0 \ln(Q/\Lambda)}, \tag{3.57}$$

where b_0 is a coefficient related with the number "available" flavours, and Λ are the QCD scale. This scale dependence shows an increase of the strong interaction strength with decreasing energy scale. Hence, if we try to separate the quarks inside some stable hadron (through a high energetic collision) the binding will respond with an increasing "density tube" of gluons. If enough energy is present, spontaneous generation of extra quarks will occur such that new stable and less energetic hadrons will be created. This colour confinement is the property responsible for the appearance of jets in particle collisions rather than individual quarks or gluons. These jets are "bunches" of hundreds, or thousands, of baryons that were created through this mechanism. This process is called *hadronization*.

Another important property that is a consequence of equation (3.57) is that QCD is *asymptotically free*. That is, when the binding energy increases the coupling strength decreases. This means that in case quarks are in a very high energy state, like for example in a LHC proton-proton collision, the strong interaction between them will be very weak and we may consider them as free colliding particles.

4

Effective Lagrangians

4.1 Introduction

The main idea behind effective theories is the concept of scale. Any physical problem is solved at a given scale even if most of the times that scale is not stated clearly. The energy scale is usually the defining variable that sets the physical domain we are working in and consequently will point us to the best approach (theory or model) we should use. High Energy Particle Physics is no exception. The energy scale is used to define what should be taken into account when studying a given physical process. For instance, gravitational effects are not important when one considers a high energy particle collision - they belong to a different energy scale. Additionally to this selection criteria, one should also take into account which is the most appropriate description to the study of some physical process. Once more, the energy scale will play the role of the discriminant variable helping us to decide which theory or model should be used. It is in this context that the concept of effective theories is introduced. They can be interpreted as simplifications of some underlying model, known or not, that allow us to work with a simpler version of the model and that can also make calculations easier. It should be stressed that sometimes the approximation refers to an unknown model and therefore effective theories are sometimes a means to gain some insight on the underlying theory. A simple example of an effective approach

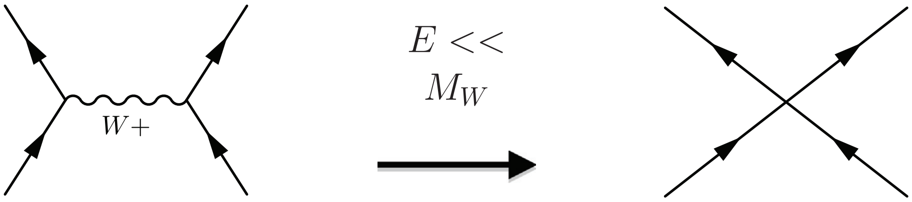

$$\frac{g^2}{8}\frac{1}{p_W^2-M_W^2}(\psi_L^i\gamma^\mu\psi_L^j)(\psi_L^k\gamma_\mu\psi_L^l)$$

$$\frac{G_F}{\sqrt{2}}(\psi_L^i\gamma^\mu\psi_L^j)(\psi_L^k\gamma_\mu\psi_L^l) + O(\frac{p_W^2}{M_W^2})$$

Figure 4.1: Fermi Effective Theory

in a case where we know the underlying theory is Special Relativity kinematics. Certainly no one would use Special Relativity to perform basic calculations of average speed from home to work. Newtonian Mechanics is a much simpler and easier model do deal with this range of velocities. In this case effectiveness means that the speeds involved are well below the speed of light and that we can take the limit $c \to \infty$.

Effective theories are not, and do not aim to be, fundamental models of Nature, and they are only proposed as an **appropriate** description of the physical process under study. Quoting Georgi:

> ”It is not necessary to use an effective theory, if you think that you know the full theory of everything. You can always compute anything in the full theory if you are sufficiently clever. It is, however, very convenient to use the effective theory. It makes calculations easier, because you are forced to concentrate on the important physics.” (39).

A classical example of an effective approach in Particle Physics is Fermi’s theory of the weak interaction (40). In this description, the W boson responsible for the weak interaction (see Figure (4.1)) was integrated out and the result is a process described by a contact four-fermion interaction. Provided that the working energies are well below the W and Z masses this is a good approximation. It can be shown that there is in fact a good matching between the two descriptions at sufficiently low energies. The unknown parameter in the effective approach example is the Fermi's constant G_F which was parametrized by experiment. In this example a *top-down* approach is followed since we already know the fundamental model and the effective approach is no more than a simplification. However, we can also follow the opposite approach. Instead of starting with some already known fundamental model, we can assume that there is some other fundamental model not yet known and that for instance the SM is just an effective theory. In this case the SM will now be the low energy asymptotic limit of the unknown model and will play the role of an effective theory resulting from integrating out the heavy fields from the underlying model. In this *bottom-up* approach the main objective is to study possible new interactions and processes that are not predicted by the SM as they only occur at energy scales of the order of the heavy fields. Therefore, the initial idea of effective theories gains versatility. The main purpose is no longer just a simplification but rather to introduce a method to study physics beyond the SM. This effective approach is usually implemented by the introduction of a set of effective operator with the SM symmetries. These operators will be used to parametrize the possible existence of new physics from experimental data. They can be build from combinations of the already existing fields or with the addition of new fields. Therefore, we are in the presence of a model where we can concentrate on the possible new physics we are interested in. The ordering of the operators, regarding their contribution to the physical processes, is done by accounting for the operator's mass dimension. This expansion is shown in equation (4.1)

$$\mathcal{L} = \mathcal{L}^{MP} + \sum_{i}^{\infty} \mathcal{C}_i \mathcal{O}_i. \tag{4.1}$$

For dimension $d \leq 4$ there is a finite set of renormalizable effective operators, while for $d > 4$ there is an infinite set of non-renormalizable operators. The parametrization is done through the constants $\mathcal{C}_i$, known as *Wilson Coefficients* and defined as

$$\mathcal{C}_i = \frac{\alpha_i}{\Lambda^{d_i - 4}}, \tag{4.2}$$

where the constants α_i are dimensionless and Λ has dimension of mass. In this approach the new interactions can be treated in the traditionally perturbative way (provided Λ is large enough) which in turn means we can interpret the α parameters as coupling constants that measure the strength of the interaction.

As previously mentioned, there is an infinite number of effective operators that can be added to the renormalizable piece of the Lagrangian. Consequently there is also an infinite number of constants α_i parametrizing the interactions. This means that in principle we would need an infinite number of experimental observables to either calculate or limit the constants α_i. To solve this problem we can begin by applying the *Appelquist-Carazzone* (41) theorem, which in short states that if the effective operators will not produce heavy masses when the scale parameter Λ goes to infinity, then the action derived from the total Lagrangian can be expanded in a power series in $\frac{1}{\Lambda}$. In practical terms we are saying that the heavy fields responsible for the new interaction have an infinite mass and their contribution for new physics at a given scale is negligible. This property is known as *decoupling* which we assume as a postulate in the reminder of this work. We should now establish a limit on the precision intended in order to truncate the power series in $\frac{1}{\Lambda}$. Since the work we will be presenting concerns the top quark, we focus on the present measurement of the top mass with its error $(173.07 \pm 0.52 \pm 0.72)$ GeV (35) which amounts to an experimental precision of 0.5%. From each additional contribution to the SM we expect and increment of approximately

$$\left(\frac{E}{\Lambda}\right)^{k-4}, \tag{4.3}$$

where E is the typical energy of the processes under study, k the effective operator mass dimension and Λ the energy scale that we take to be 1 TeV. So, due to the fact that the partonic processes under study will always concern top quark production, it is reasonable to assume $E = M_{top}$. For this energy the maximum value of k that would result in a clearly measurable contribution is $k = 6$. This results in operators with a maximum dimension of six

$$\mathcal{L}^{Total} = \mathcal{L}^{MP} + \frac{1}{\Lambda}\mathcal{L}^{(5)} + \frac{1}{\Lambda^2}\mathcal{L}^{(6)} + O(\frac{1}{\Lambda^3}). \tag{4.4}$$

After the dimensional truncation we can now start to impose additional physical constraints in order to further reduce the total number of effective operators. We follow the work of Buchmuller and Wyler (42) that have developed the first systematic approach to build the most general dimension six Lagrangian constrained by the SM symmetries. First, no additional fields are considered when building the operators. The underlying model may have some new heavy fields but as mentioned above we consider that we are working at energy scales where these fields can be *integrated out*. Therefore we use just the SM fields shown in table 4.1. Second, we impose baryon and lepton number conservation. As a consequence, no dimension five operators can be built which limits our set to dimension six operators only. Third, we force the underlying model to be invariant

$q_L^i = \binom{u_L^i}{d_L^i} \quad , \quad i = (1,2,3)$	left-handed quark doublets
$u_R^i \quad d_R^i \quad , \quad i = (1,2,3)$	right-handed quark doublets
$\phi \quad , \quad \tilde{\phi} = i\sigma_2\phi$	Higgs boson doublet
$G_\mu^a \quad , \quad a = 1, ..., 8$ $G_{\mu\nu}^a = \partial_\mu G_\nu^a - \partial_\nu G_\mu^a + g_s f^{abc} G_\mu^b G_\nu^c$	Gluon Gluon Strength Field Tensor
$W_\mu^I \quad , \quad I = 1, 2, 3$ $W_{\mu\nu}^a = \partial_\mu W_\nu^I - \partial_\nu W_\mu^I + g\epsilon^{IJK} W_\mu^J W_\nu^K$	W boson W Strength Field Tensor
B_μ $B_{\mu\nu}^a = \partial_\mu B_\nu - \partial_\nu B_\mu$	B boson B Strength Field Tensor

Table 4.1: Particle Fields considered.

under the SM symmetry group. Therefore, the effective operators must be invariant with respect to $SU(3) \times SU(2) \times U(1)$. Even with these three conditions the total number of operators can still be reduced using the equations of motion as well as Fierz transformations. In (42) Buchumeller and Wyler initially proposed a total of 80 independent operators but latter Grzadkowski *et al* (43) reduced this number to 59 operators. Previously, Saavedra (44) had reduced the independent set of operators one has to take into account to study top quark physics. It is this set we will be using in our analysis.

4.2 Flavour Changing Neutral Current (FCNC)

FCNC processes are interactions that at the partonic level conserve charge but not flavour. These processes are highly suppressed in the SM by the known Glashow-Iliopoulos-Maiani (GIM) (45) mechanism and are only present at higher order in perturbation theory. This suppression can be easily understood from equations (3.49)-(3.51). In order to obtain these equations we have rotated the fermion fields into a mass basis, which gave origin to the mass terms in the Yukawa Lagrangian. We saw that as a consequence we got the CKM matrix which induces quark flavour mixing with charged currents. Now, if we proceed in the same manner but with the neutral currents Lagrangian term, we will end up with a diagonal mixing matrix. Note that this would not be true if we had more than one Higgs doublet. Therefore, within the SM all FCNC currents are forbidden at tree level, and can only occur at loop level. One example of such a case is shown in figure 4.2. From this diagram, we see that the FCNC current is suppressed by a loop factor $(1/(16\pi^2))$ and by the W propagator m_b^2/M_W^2. Additionally, due to the

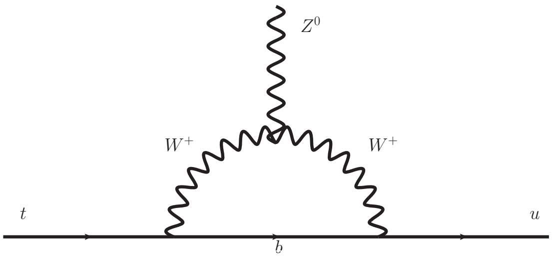

Figure 4.2: SM top quark FCNC loop diagram.

off diagonal CKM matrix elements included, which in the example shown would be $V_{bu} \sim 10^{-3}$, we end up with a total transition amplitude highly suppressed. The SM prediction for the largest top quark FCNC branching ratios is for $t \to gc$ decay and is of order $\sim 10^{-12}$ (46) (1). This value is a long way from the most recent measurement which gives rise to the limit $Br(t \to ug) < 2.9 \times 10^{-4}$ (35). However, other models predict much larger values for these branching ratios, like for example the *Two Higgs Doublet Model* (47) (2HDM), where the FCNC branching ratios can be larger by up to eight orders of magnitude. In table 4.2 we show the branching ratios for top quark FCNC decay in five different models: with $Q = 2/3$ quark singlets (QS), a general 2HDM, a flavour-conserving (FC) 2HDM, the *Minimal Supersymmetric Standard Model* (MSSM) and with R parity violating SUSY.

$BR(t \to FCNC)$ in several modes						
	SM	QS	2HDM	FC 2HDM	MSSM	R SUSY
$t \to q\gamma$	$\sim 10^{-14}$	$\sim 10^{-9}$	$\sim 10^{-6}$	$\sim 10^{-9}$	$\sim 10^{-6}$	$\sim 10^{-6}$
$t \to qZ$	$\sim 10^{-14}$	$\sim 10^{-4}$	$\sim 10^{-7}$	$\sim 10^{-10}$	$\sim 10^{-6}$	$\sim 10^{-5}$
$t \to qg$	$\sim 10^{-12}$	$\sim 10^{-7}$	$\sim 10^{-4}$	$\sim 10^{-5}$	$\sim 10^{-5}$	$\sim 10^{-4}$

Table 4.2: top quark FCNC branching ratios comparison (1).

Taking into account the extremely low branching ratio values for the SM and the striking disagreement with several other models, top quark FCNC creates a perfect opportunity to study physics beyond the SM. Our starting point to perform top FCNC related studies is to write the effective Lagrangian. This means writing all effective operators where at least one top quark is present. As previously stated the Lagrangian is available in (44) where a minimum set of operators for top studies has been determined. We should note that the total number of operators will now depend on the physical process under study. In this work three types of production processes were considered

- **Direct top**: production of one top quark.
- **Single top**: production of one top quark and one additional jet.
- **t$\bar{\textbf{t}}$**: production of a top anti-top pair $t\bar{t}$.

Following the notation of (44), we now present a list of the total set of operators taken from (42) which describe top strong and electroweak FCNC interactions. Due to the specificity of each physical process, the four-fermion operators sets will be considered together with each production process.

4.2.1 Effective operators in the strong sector

For the strong FCNC interaction we can have three effective operators:

$$\mathcal{O}^{ij}_{uG\phi} = \bar{q}^i_L \, \lambda^a \, \sigma^{\mu\nu} \, u^j_R \, \tilde{\phi} \, G^{a\mu\nu} \,, \tag{4.5}$$

and

$$\mathcal{O}^{ij}_{uG} = \bar{u}^i_R \, \lambda^a \, \gamma_\mu D_\nu u^j_R \, G^{a\mu\nu} \,, \quad \mathcal{O}^{ij}_{qG} = \bar{q}^i_L \, \lambda^a \, \gamma_\mu D_\nu q^j_L \, G^{a\mu\nu} \,, \tag{4.6}$$

where $G^a_{\mu\nu}$ is the gluonic field tensor, u^i_R stands for a right-handed quark singlet and q^i_L represents the left-handed quark doublet. FCNC occurs because one of the indices is always equal to 3 while the other is either 1 or 2, that is, there is always one (and one only) top-quark present in the operator; the remaining fermion field in the interaction is either a u or a c-quark. Throughout this thesis we assume that $\mathcal{O}^{ij}$ and $\mathcal{O}^{ji}$ are independent operators and the hermitian conjugate of all the operators are included in the final Lagrangian.

4.2.2 Effective operators in the electroweak sector

There are also effective operators stemming from the electroweak sector that would give rise to new FCNC interactions involving the top quark (48, 49). We start by listing the chirality flipping operators which are the equivalent to the ones in the strong sector, the only difference being the gluonic tensor replaced by the $U(1)$ and $SU(2)$ field tensors. They can be written as

$$\mathcal{O}^{ij}_{uB\phi} = \bar{q}^i_L \, \sigma^{\mu\nu} \, u^j_R \, \tilde{\phi} \, B_{\mu\nu} \,, \quad \mathcal{O}^{ij}_{uW\phi} = \bar{q}^i_L \, \tau_I \, \sigma^{\mu\nu} \, u^j_R \, \tilde{\phi} \, W^I_{\mu\nu} \,, \tag{4.7}$$

and

$$\mathcal{O}_{uB}^{ij} = \bar{u}_R^i \gamma_\mu D_\nu u_R^j B^{\mu\nu}, \quad \mathcal{O}_{qB}^{ij} = \bar{q}_L^i \gamma_\mu D_\nu q_L^j B^{\mu\nu}, \quad \mathcal{O}_{uW}^{ij} = \bar{q}_L^i \tau_I \gamma_\mu D_\nu q_L^j W_{\mu\nu}^I, \tag{4.8}$$

where $B^{\mu\nu}$ and $W_{\mu\nu}^I$ are the $U(1)_Y$ and $SU(2)_L$ field tensors, respectively. There are also equations of motion in the electroweak sector that relate the operators in (4.7) with the ones in (4.8) and with four-fermion operators (50). Therefore, according to the production process we are interested in, one will be able to discard some of these operators.

Besides chirality-flipping operators there are chirality conserving FCNC operators. Their flavour conserving counterparts are already present in the SM Lagrangian at tree-level. In fact, the vertex $\bar{t}tZ$ has two vector contributions of different magnitudes, one proportional to $\gamma_\mu \gamma_L$ and the other proportional to $\gamma_\mu \gamma_R$. Hence the flavour conserving contribution would modify the Z boson neutral current. All the chirality conserving operators involve the Higgs doublet. As the Higgs field is electrically neutral, there are more effective operators which will only contribute to new Z FCNC interactions. This set of operators can be written as

$$\mathcal{O}_{\phi u}^{ij} = i\,(\phi^\dagger D_\mu \phi)\,(\bar{u}_R^i \gamma^\mu u_R^j), \tag{4.9}$$

$$\mathcal{O}_{\phi q}^{(1),ij} = i\,(\phi^\dagger D_\mu \phi)\,(\bar{q}_L^i \gamma^\mu q_L^j), \quad \mathcal{O}_{\phi q}^{(3),ij} = i\,(\phi^\dagger \tau_I D_\mu \phi)\,(\bar{q}_L^i \gamma^\mu \tau_I q_L^j), \tag{4.10}$$

and

$$\mathcal{O}_{D_u}^{ij} = (\bar{q}_L^i D^\mu u_R^j)\, D_\mu \tilde{\phi}, \quad \mathcal{O}_{\bar{D}_u}^{ij} = (D^\mu \bar{q}_L^i u_R^j)\, D_\mu \tilde{\phi}. \tag{4.11}$$

4.3 Direct top

FCNC Direct top production can be represented by the tree level diagram shown in figure 4.3 It was shown in (44) that the strong sector for top FCNC can be reduced to a single effective operator, which is shown in equation (4.12). This is the same of operator of equation (4.5) but shown here in a different notation. The next-to-leading (NLO) QCD correction to Direct top production was calculated in (51). They found that this correction amounts to a cross section enhancement of

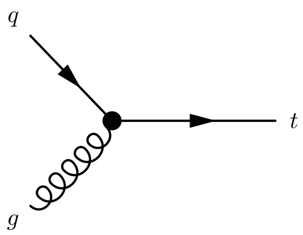

Figure 4.3: Direct top production, $q = u, c$.

up to 60% for the Tevatron and 40% for LHC at 14 Tev, relative to the tree-level result. Therefore we face a non negligible correction that should be taken into account. Part of the work we will be presenting here concerns the development of a parton-level event generator for FCNC Direct top production at NLO (a full chapter will be dedicated to this process).

$$\mathcal{O}_S = g_s \frac{k^i}{\Lambda} \bar{t} \sigma^{\mu\nu} T^a (f^i + i h^i \gamma_5) q G^a_{\mu\nu} \quad q = u, c \tag{4.12}$$

4.4 FCNC Single top

FCNC Single top production refers to a partonic final state of a top quark plus a jet from a light quark. In principle we could also have a gluon as a jet in the final state but this process will be treated as the real radiation part of the FCNC Direct top at NLO. The FCNC Single top can arise both at an electron-positron or at a hadronic collider. We will determine the minimum effective Lagrangian for each case.

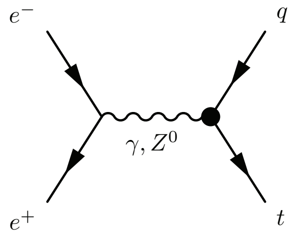

Figure 4.4: *top* + *jet* production from e^+e^-, $q = u, c$.

4.4.1 $e^+e^- \to t\bar{q}$

From (42), (52) and (43) there are 13 effective operators that contribute to the process $e^+\,e^- \;\to t\,\bar{q}$, with $q = u, c$. Eight of them are four-fermion operators

$$\begin{aligned}
\mathcal{O}_{lq}^{11k3} &= (\bar{l}_{L1}\,\gamma^\mu\,l_{L1})\,(\bar{q}_{Lk}\,\gamma_\mu\,q_{L3}), && (4.13)\\
\mathcal{O}_{eu}^{11k3} &= (\bar{e}_R\,\gamma^\mu\,e_R)\,(\bar{u}_{Rk}\,\gamma_\mu\,u_{R3}), && (4.14)\\
\mathcal{O}_{lu}^{13k1} &= (\bar{l}_{L1}\,u_{R3})\,(\bar{u}_{Rk}\,l_{L1}), && (4.15)\\
\mathcal{O}_{qe}^{k113} &= (\bar{q}_{Lk}\,e_R)\,(\bar{e}_R\,q_{L3}), && (4.16)\\
\mathcal{O}_{lq\epsilon}^{11k3} &= (\bar{l}_{L1}\,e_R)\,[(\bar{q}_{Lk}\,\epsilon)^T\,u_{R3}], && (4.17)\\
\mathcal{O}_{lq\epsilon}^{113k} &= (\bar{l}_{L1}\,e_R)\,[(\bar{q}_{L3}\,\epsilon)^T)\,u_{Rk}], && (4.18)\\
\mathcal{O}_{ql\epsilon}^{k113} &= (\bar{q}_{Lk}\,e_R)\,[(\bar{l}_{L1}\,\epsilon)^T u_{R3}], && (4.19)\\
\mathcal{O}_{ql\epsilon}^{311k} &= (\bar{q}_{L3}\,e_{R1})\,[(\bar{l}_{L1}\,\epsilon)^T\,u_{Rk}], && (4.20)
\end{aligned}$$

with k = 1, 2. The remaining five come from the contribution through FCNC electroweak couplings with the top quark:

$$\mathcal{O}_{\phi q}^{(1,ij)}, \mathcal{O}_{\phi q}^{(3,ij)}, \mathcal{O}_{\phi u}^{ij} \qquad (4.21)$$

$$\mathcal{O}_{uW}^{ij}, \mathcal{O}_{uB\phi}^{ij}, \qquad (4.22)$$

where we have introduced the flavour indices i, j in the second set of operators to distinguish the top-up ($i, j = \{1, 3\}, \{3, 1\}$) from the top-charm $i, j = \{2, 3\}, \{3, 2\}$ anomalous coupling. To sum up, the total effective Lagrangian for $e^+\,e^- \;\to t\,\bar{q}$ is constituted by the operators in Table 4.3.

$\mathcal{O}_{lq}^{11k3}$	$\mathcal{O}_{\phi q}^{(1,ij)}$
$\mathcal{O}_{eu}^{11k3}$	$\mathcal{O}_{\phi q}^{(3,ij)}$
$\mathcal{O}_{lu}^{13k1}$	$\mathcal{O}_{\phi u}^{ij}$
$\mathcal{O}_{qe}^{k113}$	$\mathcal{O}_{uW}^{ij}$
$\mathcal{O}_{lq\epsilon}^{11k3}$	$\mathcal{O}_{uB\phi}^{ij}$
$\mathcal{O}_{lq\epsilon}^{113k}$	
$\mathcal{O}_{ql\epsilon}^{k113}$	
$\mathcal{O}_{ql\epsilon}^{311k}$	

Table 4.3: Minimum set of effective operators for $e^+e^- \to t\bar{q}$.

In principle the operators $\mathcal{O}_{qW}^{ij}$, $\mathcal{O}_{qB}^{ij}$, $\mathcal{O}_{uB}^{ij}$, $\mathcal{O}_{Du}^{ij}$ and $\mathcal{O}_{\bar{D}u}^{ij}$ should also be considered but as shown in (44) these operators can be written as a linear combination of the ones in table 4.3 which makes them redundant. We note however that although the operator $\mathcal{O}_{qW}^{13}$ concerns only the FCNC coupling between a top and a u-quark, its equation of motion includes the $\mathcal{O}_{uW}^{32}$ operator which contributes to the FCNC coupling between a top and a c-quark. Therefore, when discarding these redundant operators we will also include the operators with top quark couplings to c-quarks. The final minimal Lagrangian for the process is shown in equation (4.23).

$$
\begin{aligned}
\mathcal{L}_{e^+\,e^-\to t\,\bar{q}} \;=\; & \sum_{\substack{i,j=1,3\\ or\\ i,j=2,3\\ i\neq j}} \Big(\alpha_{uW}^{ij} \mathcal{O}_{uW}^{ij} + \alpha_{uB\phi}^{ij}\, \mathcal{O}_{uB\phi}^{ij} + \alpha_{\phi u}^{ij}\, \mathcal{O}_{\phi u}^{ij} + \alpha_{\phi q}^{(3,ij)}\, \mathcal{O}_{\phi q}^{(3,ij)} + \alpha_{\phi q}^{(1,ij)}\, \mathcal{O}_{\phi q}^{(1,ij)} \Big) \\
& + \sum_{k=1}^{2} \Big[\alpha_{lq}^{11k3}\, (\bar{e}_L\, \gamma^\mu\, e_L)(\bar{u}_{Lk}\, \gamma_\mu\, t_L) - \frac{1}{2} \alpha_{lu}^{13k1} (\bar{e}_L\, \gamma^\mu\, e_L)(\bar{u}_{Rk}\, \gamma_\mu\, t_R) \\
& - \frac{1}{2} \alpha_{qe}^{k113} (\bar{e}_R\, \gamma^\mu\, e_R)(\bar{u}_{Lk} \gamma_\mu t_L) + \alpha_{eu}^{11k3} (\bar{e}_R\, \gamma^\mu\, e_R)(\bar{u}_{Rk} \gamma_\mu t_R) \\
& \Big(\frac{\alpha_{ql\epsilon}^{k113}}{2} + \alpha_{lq\epsilon}^{11k3} \Big) (\bar{u}_{Lk}\, t)(\bar{e}_L\, e) + \frac{1}{8} \alpha_{ql\epsilon}^{k113} (\bar{u}_{Lk} \sigma^{\alpha\beta} t)(\bar{e}_L \sigma_{\alpha\beta} e) \\
& + \Big(\frac{\alpha_{ql\epsilon}^{311k*}}{2} + \alpha_{lq\epsilon}^{113k*} \Big) (\bar{u}_{Rk}\, t)(\bar{e}_R\, e) + \alpha_{ql\epsilon}^{311k*} (\bar{u}_{Rk} \sigma^{\alpha\beta} t)(\bar{e}_R \sigma_{\alpha\beta} e) \Big] . \qquad (4.23)
\end{aligned}
$$

4.4.2 $qq \to tq$

For hadronic FCNC single top quark production we only considered gluons and $q = u, \bar{u}$ quarks in the initial state. We adopt this simplification since processes with other quarks in the initial state will be suppressed with respect to u quarks and gluons due to their low PDF values. This means that the cross section for e.g. $cc \to tc$ is much smaller than the equivalent cross section for $uu \to tu$. At most we could have included processes that have d quarks in the initial state but this would massively increase the final number of operators. For this reason we decided to exclude these cases.

Again from (42), (52) and (43) we extract the 16 effective operators that contribute to FCNC single top production in hadronic collisions, i.e, to the processes $gq \to tg$, $qq \to tq$ and $gg \to tq$. Nine of them are four-fermion operators

$$\begin{aligned}
\mathcal{O}_{qq}^{ijkl} &= \frac{1}{2}(\bar{q}_{Li}\,\gamma^{\mu}\,q_{Lj})\,(\bar{q}_{Lk}\,\gamma_{\mu}\,q_{Ll}), && (4.24)\\
\mathcal{O}_{qq'}^{ijkl} &= \frac{1}{2}(\bar{q}_{Lia}\,\gamma^{\mu}\,q_{Ljb})\,(\bar{q}_{Lkb}\,\gamma_{\mu}\,q_{Lla}), && (4.25)\\
\mathcal{O}_{uu}^{ijkl} &= \frac{1}{2}(\bar{u}_{Ri}\,\gamma^{\mu}\,u_{Rj})\,(\bar{u}_{Rk}\,\gamma_{\mu}\,u_{Rl}), && (4.26)\\
\mathcal{O}_{ud}^{ijkl} &= (\bar{u}_{Ri}\,\gamma^{\mu}\,u_{Rj})\,(\bar{d}_{Rk}\,\gamma_{\mu}\,d_{Rl}), && (4.27)\\
\mathcal{O}_{ud'}^{ijkl} &= (\bar{u}_{Ria}\,\gamma^{\mu}\,u_{Rjb})\,(\bar{d}_{Rkb}\gamma_{\mu}\,d_{Rla}), && (4.28)\\
\mathcal{O}_{qu}^{ijkl} &= (\bar{q}_{Li}\,u_{Rj})\,(\bar{u}_{Rk}\,q_{Ll}), && (4.29)\\
\mathcal{O}_{qu'}^{ijkl} &= (\bar{q}_{Lia}\,u_{Rjb})\,(\bar{u}_{Rkb}q_{Lla}), && (4.30)\\
\mathcal{O}_{qd}^{ijkl} &= (\bar{q}_{Li}\,d_{Rj})\,(\bar{d}_{Rk}\,q_{Ll}), && (4.31)\\
\mathcal{O}_{qd'}^{ijkl} &= (\bar{q}_{Lia}\,d_{Rjb})\,(\bar{d}_{Rkb}q_{Lla}), && (4.32)\\
& && (4.33)
\end{aligned}$$

where $i, j, k, l = 1, 2, 3$ are flavour indices and the indices a, b represent the contraction of colour indices, only if this pairing is different from the one for the spinor contraction. In (52) this set of operators is further simplified to the set of operators show in table 4.4. There are in total 24 different combinations coming from setting two of the indices i, j, k equal to 1 while the other is set to 1 or 2. These 24 can be reduced to 12 operators since for single top production we are just interested in operators that have a single FCNC coupling. This is not the case, for example, for the operator $(\bar{c}_R \gamma^\mu u_R)(\bar{u}_L \gamma_\mu t_L)$ which introduces two FCNC fermionic flows. Finally, the 12 independent four-fermion operators are implemented by setting $k = j = 1$ and $i = 1, 2$.

$\frac{1}{2}(\alpha_{qq}^{kji3} + \alpha_{qq'}^{ijk3})(\bar{u}_{Lk}\gamma^\mu u_{Lj})(\bar{u}_{Li}\gamma_\mu t_L)$	$-\frac{1}{2}\alpha_{qu'}^{k3ij}(\bar{u}_{Lk}\gamma^\mu u_{Lj})(\bar{u}_{Ri}\gamma_\mu t_R)$
$-\frac{1}{2}\alpha_{qu'}^{ijk3}(\bar{u}_{Rk}\gamma^\mu u_{Rj})(\bar{u}_{Li}\gamma_\mu t_L)$	$\frac{1}{2}\alpha_{uu}^{kji3}(\bar{u}_{Rk}\gamma^\mu u_{Rj})(\bar{u}_{Ri}\gamma_\mu t_R)$
$-\frac{1}{2}\alpha_{qu}^{k3ij}(\bar{u}_{Lka}\gamma^\mu u_{Ljb})(\bar{u}_{Rib}\gamma_\mu t_{Ra})$	$-\frac{1}{2}\alpha_{qu}^{ijk3}(\bar{u}_{Rka}\gamma^\mu u_{Rjb})(\bar{u}_{Lia}\gamma_\mu t_{La})$

Table 4.4: Four-fermion operators to FCNC single top production.

The remaining seven effective operators come from the FCNC electroweak and strong couplings with the top quark

$$\mathcal{O}_{u\phi}^{ij}, \mathcal{O}_{\phi q}^{(1,ij)}, \mathcal{O}_{\phi q}^{(3,ij)}, \tag{4.34}$$

$$\mathcal{O}_{\phi u}^{ij}, \mathcal{O}_{uG\phi}^{ij}, \mathcal{O}_{uW}^{ij}, \tag{4.35}$$

$$\mathcal{O}_{uB\phi}^{ij}. \tag{4.36}$$

As before we have discarded the operators $\mathcal{O}_{qG}^{ij}$, $\mathcal{O}_{qW}^{ij}$, $\mathcal{O}_{qB}^{ij}$, $\mathcal{O}_{uG}^{ij}$, $\mathcal{O}_{uB}^{ij}$, $\mathcal{O}_{Du}^{ij}$ and $\mathcal{O}_{\bar{D}u}^{ij}$ since they can be proved redundant using the equations of motion (44).

Regarding four-fermion operators and focusing on the top-charm anomalous couplings we can have the following classes of operators: $(\bar{u}\,\Gamma^\mu\, u)(\bar{c}\,\Gamma_\mu\, t)$, $(\bar{c}\,\Gamma^\mu\, u)(\bar{u}\,\Gamma_\mu\, t)$ and $(\bar{u}\,\Gamma^\mu\, c)(\bar{u}\,\Gamma_\mu\, t)$. The later will not be considered because any Fierz transformation will result in two "FCNC" currents. Because the second operator can be Fierz transformed into the first one, the final Lagrangian is therefore

$$\begin{aligned} \mathcal{L}_{qq,qg,gg\to t\,\bar{q}} \quad = \quad & \sum_{\substack{i,j=1,3 \\ or \\ i,j=2,3 \\ i\neq j}} \Big(\alpha_{uG}^{ij}\mathcal{O}_{uG\phi}^{ij} + \alpha_{uW}^{ij}\mathcal{O}_{uW}^{ij} + \alpha_{uB\phi}^{ij}\,\mathcal{O}_{uB\phi}^{ij} + \alpha_{\phi u}^{ij}\,\mathcal{O}_{\phi u}^{ij} + \alpha_{\phi q}^{(3,ij)}\,\mathcal{O}_{\phi q}^{(3,ij)} \\ & + \alpha_{\phi q}^{(1,ij)}\,\mathcal{O}_{\phi q}^{(1,ij)} + \alpha_{u\phi}\,\mathcal{O}_{u\phi}^{ij} \Big) + \mathcal{L}_{4fu} + \mathcal{L}_{4fc} \end{aligned} \tag{4.37}$$

where $\mathcal{L}_{4fu}$ is the four-fermion Lagrangian for anomalous top-up coupling

$$\begin{aligned}
\mathcal{L}_{4fu} &= \frac{1}{2}(\alpha_{qq}^{1113} + \alpha_{qq'}^{1113})(\bar{u}_L\, \gamma^\mu u_L)(\bar{u}_L \gamma_\mu t_L) \\
&\quad -\frac{1}{2}(\alpha_{qu'}^{1311} + \frac{1}{3}\alpha_{qu}^{1311})(\bar{u}_L \gamma^\mu u_L)(\bar{u}_R \gamma_\mu t_R) \\
&\quad -\frac{1}{2}(\alpha_{qu'}^{1113} + \frac{1}{3}\alpha_{qu}^{1113})(\bar{u}_R \gamma^\mu u_R)(\bar{u}_L \gamma_\mu t_L) \\
&\quad +\frac{1}{2}\alpha_{uu}^{1113}(\bar{u}_R \gamma^\mu u_R)(\bar{u}_R \gamma_\mu t_R) \\
&\quad -\frac{1}{4}\alpha_{qu}^{1311}(\bar{u}_L \gamma^\mu \lambda^a u_L)(\bar{u}_R \gamma_\mu \lambda^a t_R) \\
&\quad -\frac{1}{4}\alpha_{qu}^{1113}(\bar{u}_R \gamma^\mu \lambda^a u_R)(\bar{u}_L \gamma_\mu \lambda^a t_L) \qquad (4.38)
\end{aligned}$$

and $\mathcal{L}_{4fc}$ is the four-fermion Lagrangian for anomalous top-charm coupling

$$\begin{aligned}
\mathcal{L}_{4fc} &= \frac{1}{2}(\alpha_{qq}^{1123} + \alpha_{qq'}^{2113} + \frac{1}{3}\alpha_{qq}^{2113} + \frac{1}{3}\alpha_{qq'}^{1123})(\bar{u}_L\, \gamma^\mu u_L)(\bar{c}_L \gamma_\mu t_L) \\
&\quad -\frac{1}{2}(\alpha_{qu'}^{1321} + \frac{1}{3}\alpha_{qu}^{1321})(\bar{u}_L \gamma^\mu u_L)(\bar{c}_R \gamma_\mu t_R) \\
&\quad -\frac{1}{2}(\alpha_{qu'}^{2113} + \frac{1}{3}\alpha_{qu}^{2113})(\bar{u}_R \gamma^\mu u_R)(\bar{c}_L \gamma_\mu t_L) \\
&\quad +\frac{1}{2}(\alpha_{uu}^{1123} + \frac{1}{3}\alpha_{uu}^{2113})(\bar{u}_R \gamma^\mu u_R)(\bar{c}_R \gamma_\mu t_R) \\
&\quad -\frac{1}{4}\alpha_{qu}^{1321}(\bar{u}_L \gamma^\mu \lambda^a u_L)(\bar{c}_R \gamma_\mu \lambda^a t_R) \\
&\quad -\frac{1}{4}\alpha_{qu}^{2113}(\bar{u}_R \gamma^\mu \lambda^a u_R)(\bar{c}_L \gamma_\mu \lambda^a t_L) \\
&\quad +\frac{1}{4}(\alpha_{qq}^{2113} + \alpha_{qq'}^{1123})(\bar{c}_L \gamma^\mu \lambda^a t_L)(\bar{u}_L \gamma^\mu \lambda^a u_L) \\
&\quad +\frac{1}{4}\alpha_{uu}^{2113}(\bar{c}_R \gamma^\mu \lambda^a t_R)(\bar{u}_R \gamma^\mu \lambda^a u_R) \\
&\quad +(\frac{1}{3}\alpha_{qu'}^{2311} + \alpha_{qu}^{2311})(\bar{c}_L t_R)(\bar{u}_R u_L) + \frac{1}{2}\alpha_{qu'}^{2311}(\bar{c}_L \lambda^a t_R)(\bar{u}_R \lambda^a u_L) \\
&\quad +(\frac{1}{3}\alpha_{qu'}^{1123} + \alpha_{qu}^{1123})(\bar{c}_R t_L)(\bar{u}_L u_R)) + \frac{1}{2}\alpha_{qu'}^{1123}(\bar{c}_R \lambda^a t_L)(\bar{u}_L \lambda^a u_R). \qquad (4.39)
\end{aligned}$$

The operators with the Gell-Mann matrices come from the ones where quark colours indices are explicitly summed, and we have rearranged them in this form

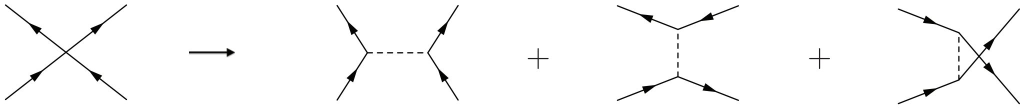

Figure 4.5: Auxiliary field mechanism.

to allow the implementation in LanHEP (53) which is a Feynman rules generator.

All four-fermion operators presented in equation (4.38) and (4.39) join four colour particles in one vertex, which is a type of interaction LanHEP is not able to handle automatically, due to the complex colour flow. Therefore, we had to implement these operators using an auxiliary field mechanism (54), where the 4-colour vertex is replaced by 3-colour vertices that when combined in s, t and u channels, will reconstruct the 4-fermion interaction. This is shown in Figure 4.5. These 3-colour vertices are implemented by introducing the interaction terms in the initial Lagrangian together with a unit mass field with a point-like propagator. In equation (4.40) a vectorial auxiliary field example is shown. We can easily check that the equation of motion for the X^μ field results in the initial Lagrangian.

$$\mathcal{L}_{4F} = (\bar{\psi}_L^i \gamma^\mu \psi_L^j)(\bar{\psi}_L^k \gamma_\mu \psi_L^l) \rightarrow (\bar{\psi}_L^i \gamma^\mu \psi_L^j) X_\mu + X^\nu (\bar{\psi}_L^k \gamma_\nu \psi_L^l) + \frac{1}{2} X_\mu X^\nu \qquad (4.40)$$

4.5 $t\bar{t}$

As previously discussed, the effective operator selection will always depend on the physics process under study. In this section we discuss the case of $t\bar{t}$ FCNC production (to be discussed in detail in chapter 6). The physics case was the deviation from the SM of the $t\bar{t}$ asymmetries measured at Tevatron. The goal was to check weather the deviation could be explained by FCNC top interactions. Like before we consider dimension-six operators only as dimension-five were excluded due to baryon and lepton number conservation.

We divide the dimension six operators in two groups: the four-fermion (4F) operators and the non-4F operators. The latter can then be grouped according to the gauge boson present in the triple vertex. As we are discussing $t\bar{t}$ production, the non-4F operators contributing to the process have at least one top quark in the interaction. Operators with one top quark, a light up-quark and one gauge boson will be called FCNC operators. If the gauge boson is a gluon they are classified as strong FCNC operators (55, 56); otherwise they will be called electroweak FCNC operators (48, 49).

Before studying the possible dimension six FCNC operators that would explain the $t\bar{t}$ asymmetry, we make a small comment on anomalous $gt\bar{t}$ interaction. They can also originate $t\bar{t}$ production through diagrams shown in figure 4.6, and so we could as well think of it as a source of such asymmetry. However, because the initial state is symmetric, these diagrams will only contribute to the cross section but not to the asymmetry. Therefore, any differences produced by these operators would change only the cross section, but not the asymmetry where the discrepancy is.

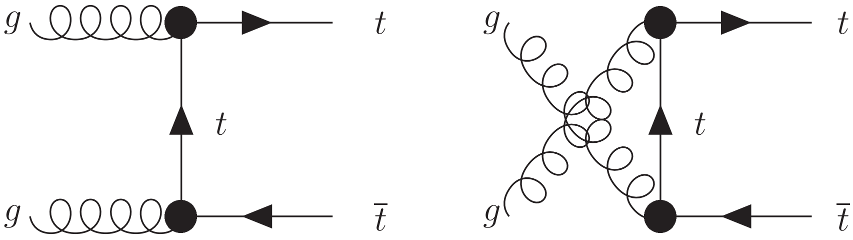

Figure 4.6: Feynman diagrams for $t\,\bar{t}$ production via anomalous $gt\bar{t}$ interaction.

In the FCNC case, there are two sets of diagrams one has to consider: the ones initiated by gluons and the ones initiated by light quarks. For the same reasons discussed above, the contribution from the diagrams in fig 4.7 should also be negligible. Therefore there are only contributions coming from the diagrams in fig 4.8. Regarding those diagrams (fig 4.8), and taking into account that the contribution of the c-quark is much smaller in respect to the u-quark, all contributions with a c quark in the initial state, were discarded. Note that there are no s-channel contributions for the FCNC case because we have a top-antitop pair in the final state. Finally, we will consider all four-fermion operators

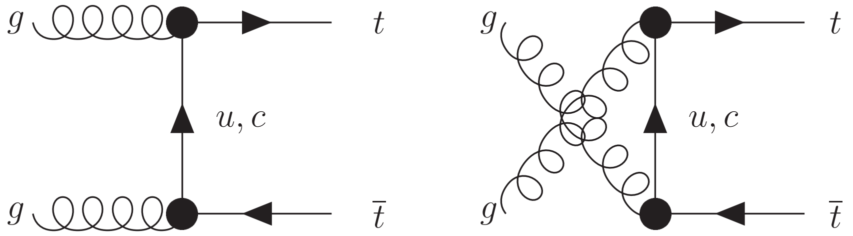

Figure 4.7: Feynman diagrams with FCNC operators for $t\,\bar{t}$ production via gluon fusion.

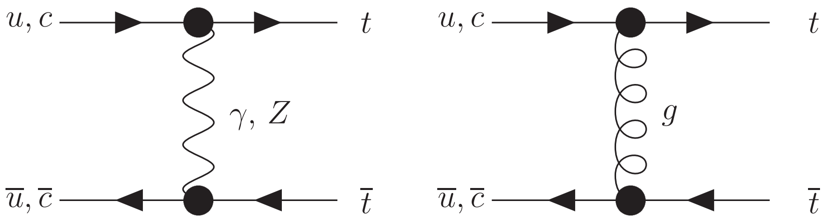

Figure 4.8: FCNC Feynman diagrams for $t\,\bar{t}$ production via $q\bar{q}$ fusion.

which will produce the diagram of figure 4.9. Additionally, we will consider not only the interference term with the SM contribution, of order $1/\Lambda^2$ but also the modulus-square terms of order $1/\Lambda^4$. We will now discuss the minimum number of operators to be used in our analysis.

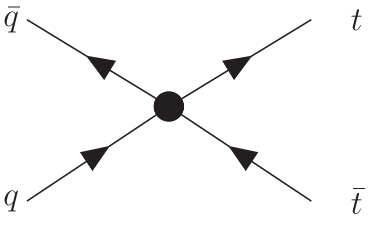

Figure 4.9: Four-fermion Feynman diagrams for $t\,\bar{t}$ production.

4.5.1 Strong and Electroweak sector

For the strong FCNC interaction, we can have three effective operators:

$$\mathcal{O}^{ij}_{uG\phi}, \tag{4.41}$$

and

$$\mathcal{O}^{ij}_{uG}\,, \quad \mathcal{O}^{ij}_{qG}. \tag{4.42}$$

The operators in (4.41) are related to the operators in (4.42) through equations of motion that also involve 4F operators (42, 43, 50, 55, 56). However, the four-fermion operators appearing in those equations have either one or three top-quarks (50), which means the operators in (4.6) can be discarded as well. The operators presented in this section will give rise to the FCNC vertices of the form $g\,t\,\bar{u}_i$ (with $u_i = u\,,\, c$) and the corresponding hermitian conjugate interaction with an independent coefficient.

In respect to the electroweak sector we have again the same effective operators described above. The first group:

$$\mathcal{O}^{ij}_{uB\phi}, \mathcal{O}^{ij}_{uW\phi} \tag{4.43}$$

and a second group:

$$\mathcal{O}^{ij}_{\phi u}, \tag{4.44}$$

$$\mathcal{O}^{(1),ij}_{\phi q}, \mathcal{O}^{(3),ij}_{\phi q}, \tag{4.45}$$

$$\mathcal{O}^{ij}_{D_u}, \mathcal{O}^{ij}_{\bar{D}_u}. \tag{4.46}$$

Again, the use of the equations of motion allow us to discard the operators in (4.46). In the electroweak sector, there are now four-fermion operators with one top and one anti-top. However, those four-fermion operators always have one b-quark in the interaction or, if not, are CKM suppressed making its contribution to the $t\bar{t}$ asymmetry negligible. Furthermore, as was shown in (50), for all the operators in (4.44) and (4.45), $\mathcal{O}^{ij}$ and $\mathcal{O}^{ji}$ are not independent. This means that the number of independent operators in (4.44) and (4.45) is reduced to three (for each light flavour). Finally, for this particular study, we can group $\mathcal{O}_{\phi q}^{(1),ij}$ and $\mathcal{O}_{\phi q}^{(3),ij}$ under the same Lorentz structure which further reduces the number of independent operators in (4.45) to two for each light flavour.

The above discussion leads us to the conclusion that the minimum number of operators needed to describe the asymmetry is 8 for each light flavour.

4.5.2 Four-fermion operators

We now turn to the four-fermion operators. In order to make the analysis as clear as possible we will reduce the operators to a manageable number making use of all allowed reduction procedures, from equations of motion to Fierz identities. Again, because the largest contribution to $t\bar{t}$ production occurs in $u\bar{u}$ fusion, we will discard all non u-quarks contribution in our study. We end up with a total of 12 operators in agreement with (57), that is, 12 operators for each light up-quark flavour and we do not consider operators with down-quarks in the initial state. This simplification allow us to find hints of the type of operators that can contribute to the asymmetry according to the its Lorentz structure. We write the four fermion lagrangian as

$$\begin{aligned}
\mathcal{L}_6^{4F} &= \frac{g_s^2}{\Lambda^2}\sum_{A,B}\left[C^1_{AB}(\bar{u}_A\gamma_\mu u_A)(\bar{t}_B\gamma^\mu t_B) + C^8_{AB}(\bar{u}_A T^a\gamma_\mu u_A)(\bar{t}_B T^a\gamma^\mu t_B)\right] + \\
&\quad \frac{g_s^2}{\Lambda^2}\sum_{A\neq B}\left[N^1_{AB}\,(\bar{u}_A\gamma_\mu t_A)(\bar{t}_B\gamma^\mu u_B) + N^8_{AB}\,(\bar{u}_A T^a\gamma_\mu t_A)(\bar{t}_B T^a\gamma^\mu u_B)\right]
\end{aligned}$$

where $T^a = \lambda^a/2$, $\{A,B\} = \{L,R\}$, and the exponent 1 and 8 denotes a colour singlet and a colour octet interaction, respectively.

5

top FCNC physics at a Linear Collider

This chapter summarises the work presented at LCWS10/ILC10 and published in http://arxiv.org/abs/1007.2992v1.

5.1 Introduction

In this work we will address the following question: will there still be top FCNC physics to explore after the LHC at an electron-positron and/or at a photon collider? Such a study would require a precise knowledge about the total luminosity that will be collected at the LHC. Moreover, it is still not clear when a new electron-positron or photon-photon collider will be built let alone its centre-of-mass energy and luminosity. Hence, we have chosen as the ”future” the LHC at $100 fb^{-1}$ and have relied on the benchmarks available in the literature for proposed electron-positron and $\gamma\gamma$ colliders. Evidently, the luminosity collected at the LHC could reach $300 fb^{-1}$ or more (with the Super Large Hadron Collider) before any other collider starts operation. However, it is not clear what the effect on bounds obtained for top FCNC related observables would be and it is reasonable to assume that most limits will stay within the same order of magnitude due to the difficulties of operating at very high luminosity. We will focus on the scenario where no evidence for new physics is found - otherwise a different approach has to be taken to understand what is the vertex or vertices that give the main contribution to the new physics observed.

In the next section we will first set the framework for our study; we will then proceed to a review of the results on top FCNC physics and the predictions available for the LHC; finally we will discuss top FCNC physics at a linear collider and at a photon collider.

5.2 The story so far and the LHC

The search for new top FCNC physics started with indirect measurements of the branching ratios of top decaying to qZ, $q\gamma$ and qg at LEP (q stands for the sum of u and c-quarks). Indirect measurement are bounds on the branching ratios that have their origin in bounds on the cross sections of FCNC top production processes, with a subsequent decay $t \to bW$. This translation is correct if only one coupling constant describes the interaction $\bar{t}qV$, where $q = u, c$ and V is a gauge boson. As a simple example, the production cross section for $e^+e^- \to \bar{t}q$, has contribution from operators of the type $\bar{t}qV$ but also from four-fermion operators. Therefore, a measurement of this cross section will not allow, in the most general case, to put a bound on any of the branching ratios $BR(t \to qV)$. Moreover, bounds on cross sections that are converted on bounds on the branching ratios rely on the fact that the experimental analysis is not contaminated with other physical processes that would invalidate the conversion. In table 5.1 (see (49) for a complete list of references) we present the experimental limits obtained at LEP, HERA and Tevatron. The superscript "d" refers to bounds obtained from direct

	LEP	HERA	Tevatron
$Br(t \to q\,Z)$	$< 7.8\%$	$< 49\%$	$< 3.7\%^{\,d}$
$Br(t \to q\,\gamma)$	$< 2.4\%$	$< 0.64\%(u)$	$< 3.2\%^{\,d}$
$Br(t \to q\,g)$	$< 17\%$	$< 13\%$	$< 0.045\%$

Table 5.1: Current experimental bounds on FCNC branching ratios. The superscript "d" refers to bounds obtained from direct measurements, as explained in the text.

measurements, that is, from $t\bar{t}$ production with one of the top-quarks decaying to bW and the other to qV, with $q = u, c$ and $V = Z, \gamma$. The best bounds are now at the % level, except for the indirect bound on $t \to qg$ which is 0.045%, from the measurement of the direct top production cross section at the Tevatron.

The gauge structure of the SM implies that a given dimension 6 operator with an impact on top interactions can also have a parallel effect on processes involving only bottom quarks. The most recent analysis for top-FCNC operators using all available B physics data was performed in (58) (see also (59)). The underlying SM gauge structure gives rise to a hierarchy of constraints: the gauge structure manifests more strongly in the operators denoted by LL in (58) as these operators are built with only $SU(2)$ doublets. Operators RR, built with singlets alone, are obviously the least constrained as no relation exists between a R-top and a R-bottom. In Table 5.2 we present the set of constraints on the branching ratios obtained in (58) when only one operator is taken at a time. Considering the prediction for the LHC with an integrated luminosity of 100 fb^{-1} (60, 61, 62), as shown in Table 5.3, it is clear that, in this approximation, operators of the type LL are already constrained beyond the reach of the LHC. This is true for operators of type LL, while limits on LR and RL operators are close to what is expected to be measured at the LHC. B factories and the Tevatron are still collecting data and therefore these constraints will be even stronger by the time

	$\mathcal{O}_{\phi}^{LL}$	$\mathcal{O}_{tW\phi}^{RL}$	$\mathcal{O}_{tB\phi}^{RL}$	$\mathcal{O}_{tW\phi}^{LR}$	$\mathcal{O}_{tB\phi}^{LR}$	$\mathcal{O}_{\phi t}^{RR}$
$Br(t \to c\,Z)$	$\mathcal{O}(10^{-6})$	3.4×10^{-5}	8.4×10^{-6}	4.5×10^{-3}	d	d
$Br(t \to c\,\gamma)$	–	1.8×10^{-5}	4.8×10^{-5}	2.3×10^{-3}	d	d
$Br(t \to u\,Z)$	$\mathcal{O}(10^{-5})$	4.1×10^{-5}	1.2×10^{-4}	3.2×10^{-3}	d	d
$Br(t \to u\,\gamma)$	–	2.1×10^{-5}	6.7×10^{-4}	1.6×10^{-3}	d	d

Table 5.2: Bounds from B-physics obtained in (58).

	ATLAS & CMS (10 fb^{-1})	ATLAS & CMS (100fb^{-1})
$Br(t \to q\,Z)$	2.0×10^{-4}	4.2×10^{-5}
$Br(t \to q\,\gamma)$	3.6×10^{-5}	1.0×10^{-5}
$Br(t \to q\,g)$ (ATLAS)	1.3×10^{-3}	4.2×10^{-4}

Table 5.3: Direct bounds based on the processe $pp \to t\bar{t} \to bW\,\bar{q}X$ at 95 % CL.

the LHC starts to analyse data. As B physics only constraints operators with origin in the electroweak sector the best bound on $Br(t \to q\, g)$ is still the Tevatron indirect bound. Note that the prediction for the LHC at 14 TeV for $Br(t \to q\, g)$ (and $100\, fb^{-1}$) is similar to the indirect Tevatron bound. Again, this is because the Tevatron's is an indirect bound - a similar analysis for direct top production at the LHC for a 14 TeV center-of-mass energy and $10\, fb^{-1}$ integrated luminosity (ATLAS only) gives $Br(t \to q\, g) < 9 \times 10^{-5}$ (63).

So far we have discussed bounds on the branching ratios even if some of them stem from limits on the productions cross sections, where FCNC is present, by taking one operator at the time. However, those bounds can also be used to place restrictions on the operators themselves. This is particularly true when four-fermion operators are present because those operators do not contribute to any of the top FCNC branching ratios discussed so far. In fact, four-fermion operators contribute only to $Br(t \to q\, e^+ e^-)$, a process that was not studied at the LHC. Both theoretical (64) and experimental (LEP) (65) studies were performed for the four-fermion operators and restrictions on the four-fermion coupling constants were set. It was shown in (64) that the direct bounds on the four-fermion coupling constants will improve at a future electron-positron collider which is a consequence of the corresponding production cross sections growth with energy. Therefore, this is clearly a case where bounds on couplings will definitely improve with the next generation of electron-positron colliders.

5.3 Is there top FCNC left to explore?

Several studies dedicated to top production and decay involving FCNC couplings were performed for electron-positron colliders. Direct bounds based on the process $e^+e^- \to t\bar{t} \to bW\, \bar{q}X$ were calculated in (66, 67) for $\sqrt{s} = 500$ GeV and $\sqrt{s} = 800$ GeV. In Table 5.4 we present limits for $Br(t \to q\, Z)$ and $Br(t \to q\, \gamma)$ taken from (66, 67) for $\sqrt{s} = 500$ GeV and $300 fb^{-1}$ of integrated luminosity. The bounds degrade as the center-of-mass energy rises due to a decreasing $t\bar{t}$ production cross section and improve as the center-of-mass energy approaches the $t\bar{t}$ threshold. There are several analysis of single top production where FCNC is

	$\sqrt{s} = 500$ GeV ($300 fb^{-1}$)
$Br(t \to q\, Z)$	$\mathcal{O}(10^{-3})$
$Br(t \to q\, \gamma)$	$\mathcal{O}(10^{-4})$

Table 5.4: Direct bounds based on the process $e^+e^- \to t\bar{t} \to bW\, \bar{q}X$ at 95 % CL.

present in the production process and not in the decay. Process $e^+e^- \to t\bar{c} + c\bar{t}$, where $t \to bW$, was studied in (68) in an effective Lagrangian approach, using the most general top FCNC three-point interactions. The same process was discussed in the same approach but with the inclusion of the four-fermion operators in (64). Other top-FCNC production processes like $e^+e^- \to t\bar{c}\nu\bar{\nu}$ and $e^+e^- \to t\bar{c}e^+e^-$ were studied in (64, 69). We will use the results obtained for future electron-positron colliders to understand if these predictions can improve the bounds on all or some of the FCNC branching ratios after the LHC has collected 100 fb^{-1} per experiment at $\sqrt{s} = 14$ TeV.

5.3.1 Electron-positron collider

To simplify our study we have considered all coupling constants real. We have made a further simplification by requiring that operators of type O_{ij} cannot be distinguished from operators of type O_{ji}, that is, all operators are independent of where the top quark is placed. We have checked that these approximations do not affect our conclusions. We have randomly generated 400K points for the coupling constants written as "$a\, 10^b$", with $-5 < a < 5$ and $-8 < b < -1$. In Figure 5.1 we present the $e^+e^- \to t\bar{c} + c\bar{t}$ cross section, for $\sqrt{s} = 500$ GeV as a function of the branching ratio $BR(t \to q\gamma)$ (up) and $BR(t \to q\gamma) + BR(t \to qZ)$ (down) with $q = u, c$. First we should note that when all couplings are taken into account, there is no simple proportionality between cross section and branching ratio. However a bound on the cross section can still be translated to a bound on a branching ratio. In the figures we draw a horizontal line that correspond to the upper limit set by the analysis in (68) for $\sqrt{s} = 500\, GeV$ and a luminosity of 500 fb^{-1}. The vertical line in Figure 5.1 corresponds to the 14 TeV LHC prediction for 100 fb^{-1}. We conclude that, because the lines cross inside the painted region, even if close to the border, the bound can only be improved with either an increase

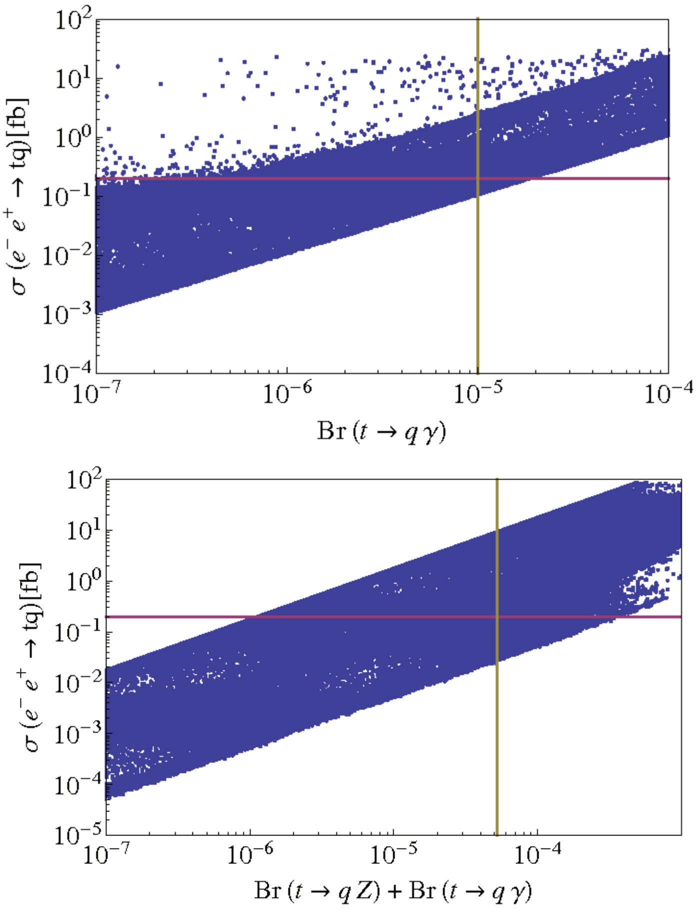

Figure 5.1: $\sigma_{e^+e^-\to t\bar{c}+c\bar{t}}$ as a function of the branching ratio $BR(t \to q\gamma)$ (up) and $BR(t \to q\gamma) + BR(t \to qZ)$ (down) with $q = u, c$ for $\sqrt{s} = 500$ GeV.

in luminosity or in center-of-mass of the electron-positron machine (68).

In Figure 5.2 we discuss how the inclusion of just one set of operators can affect the bounds on the branching ratios. There is still no bound or prediction available for $BR(t \to qe^+e^-)$, but the LHC has the means to do it. It will probably be of the same order of magnitude of the one for $BR(t \to Zq)$, that is, $\mathcal{O}(10^{-4})$. In the up panel we present the cross section for $e^+e^- \to t\bar{q} + q\bar{t}$ as a function of $BR(t \to qe^+e^-)$ with only four-fermion operators. The horizontal line is the same as the one in the previous plots while the vertical line points to a rough estimate of the bound that would be set on $BR(t \to qe^+e^-)$. When only four-fermion operators are taken into account this bound is $\mathcal{O}(10^{-9})$. In the down panel we present the same plot but without the four-fermion operators. In

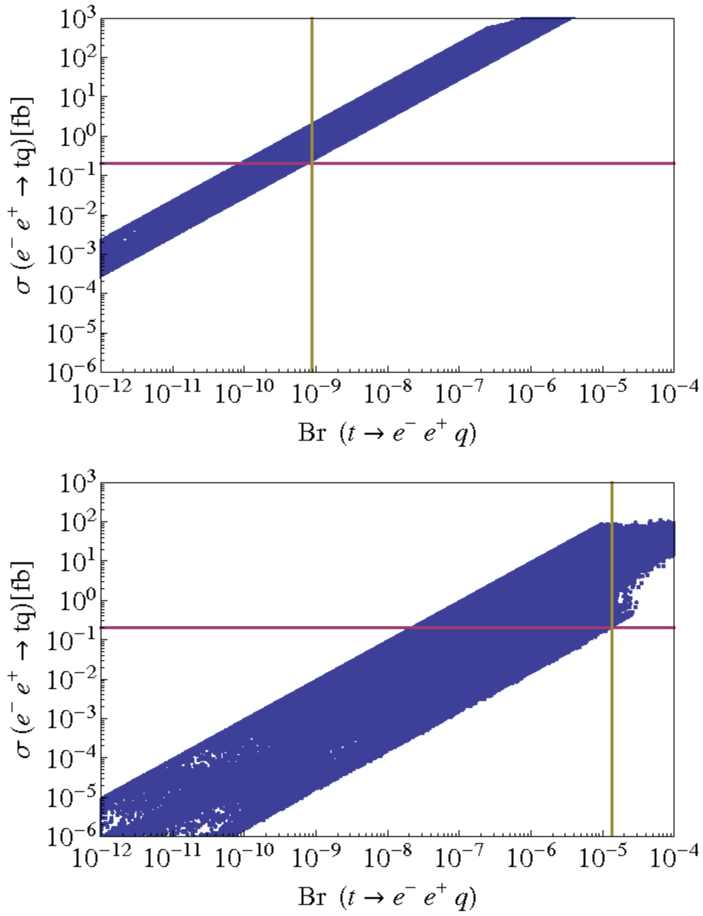

Figure 5.2: $\sigma_{e^+e^- \to t\bar{q}+q\bar{t}}$ as a function of the branching ratio $BR(t \to qe^+e^-)$ with $q = u, c$ with only four-fermion operators (up) and no four-fermion operators (down).

this case the bound is $\mathcal{O}(10^{-5})$. If all operators are taken into account the bound becomes unreliable due to interference terms but if any it will always be worst than $\mathcal{O}(10^{-5})$.

The simplest process that could probe is the strong FCNC branching ratio is $e^+e^- \to t\bar{q}g$. In this case FCNC could come either from the strong, from the electroweak, or from the four-fermion sector. We have checked that the bound is several orders of magnitude worst than what is expected for the equivalent indirect bound at the LHC.

5.3.2 $\gamma\gamma$ collider

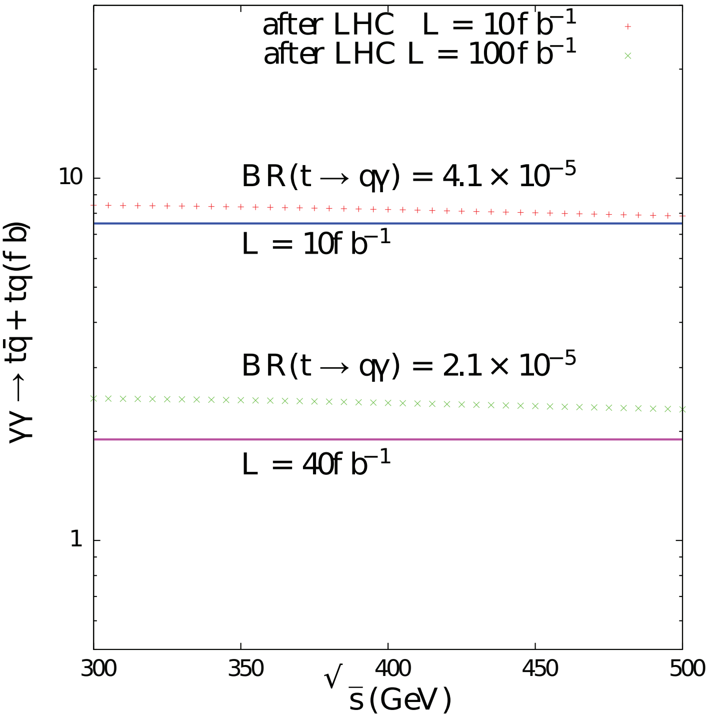

Figure 5.3: $\sigma_{\gamma\gamma\to t\bar{c}+c\bar{t}}$ as a function of $\sqrt{s}$. We present the LHC bounds for $BR(t \to q\gamma)$ for integrated luminosities of 10 and 100 fb^{-1}.

Finally we will just briefly comment on the bounds that can be obtained for a $\gamma\gamma$ collider. This is a particularly interesting case because, in our framework, there is only one coupling constant involved in the process $\gamma\gamma \to t\bar{q} + q\bar{t}$ which means that it can be unambiguous translated onto a limit on $BR(t \to \bar{q}\gamma)$. A detailed study was presented in (70) (see also (71)) for $\sqrt{s} = 400, 500,$ and 800 GeV center-of-mass energies. Using their results and the predicted bounds for $BR(t \to q\gamma)$ with $q = u, c$ for the 14 TeV LHC for integrated luminosities of 10 and 100 fb^{-1}, it is clear that the LHC bound on $BR(t \to q\gamma)$ has a good chance to be improved at a future $\gamma\gamma$ collider. Figure 5.3 shows that a total luminosity of 40 fb^{-1} would be enough to overcome the LHC 100 fb^{-1} bound almost independently of the $\gamma\gamma$ collider center-of mass energy.

5.4 Conclusions

In this chapter we have discussed what will be left to study in top FCNC physics after the LHC has reached a stage where no significant change in FCNC bounds will occur. We have concentrated on the scenario where no evidence for new physics is found - otherwise, the role of a linear collider has still to be investigated. Taking into account the predictions done so far for an electron-positron ($\gamma\gamma$) collider our conclusions are as follows:

- In this scenario, improving the LHC bounds on the BR, depends on the energy and especially on the luminosity of the future collider. Taking as a benchmark the available studies no significant improvement on the bounds of the branching ratios is expected. If new physics is found particular operators can be probed with definite observables.
- Regarding the four-fermion operators, the bounds on the coupling constants will certainly improve due to rise of cross section with the collider's energy.
- Improvement on other specific couplings taken one at a time can also be achieved. We did not consider those scenarios in our study.
- A photon-photon collider will most certainly improve the bound on the $t \to q\gamma$ FCNC branching ratio.
- Finally, NLO QCD corrections to top FCNC decays to Z and γ were shown to be negligible for our choice of operators (72). Correction to $t \to qg$, $q = u, c$ were shown to be of the order of 20 % (72).

6

$t\bar{t}$ Asymmetry

This chapter summarises the work published in the reference:
Phys. Rev. **D**86, 014016 (2012).

6.1 Introduction

The most recent measurement of the forward-backward asymmetry, $A_{FB}^{t\bar{t}}$, in top quark pair production at the Tevatron (15, 73) was performed by the CDF collaboration using a data sample with 5.3 fb^{-1} of integrated luminosity (74). After background subtraction, the value of $A_{FB}^{t\bar{t}}$ in the center-of-mass (CM) frame of the top quarks is

$$A_{FB}^{t\bar{t}} = 0.158 \pm 0.074 \tag{6.1}$$

which constitutes about two standard deviations above the Next-to-Leading-Order (NLO) Standard Model (SM) prediction (16, 17)

$$A_{FB}^{t\bar{t},\mathrm{SM}} = 0.058 \pm 0.009. \tag{6.2}$$

Despite the discrepancy in $A_{FB}^{t\bar{t}}$, the total $t\bar{t}$ production cross section is in good agreement with the SM prediction. In fact, with 4.6 fb^{-1} collected luminosity, the top quark pair production cross section (75) yields the result

$$\sigma_{t\bar{t}}^{\text{Measured}} = 7.70 \pm 0.52 \quad pb \tag{6.3}$$

for a top quark of mass 172.5 GeV, which is in good agreement with the theoretical prediction (76)

$$\sigma_{t\bar{t}}^{\text{SM}}(\text{MCFM}) = 7.45^{+0.72}_{-0.63} \quad \text{pb} \tag{6.4}$$

where MCFM stands for Monte Carlo for FeMtobarn processes (77). Measurements of the $t\bar{t}$ differential cross section with the $t\bar{t}$ invariant mass ($m_{t\bar{t}}$), $d\sigma/dm_{t\bar{t}}$ were also performed by the CDF collaboration (78). With an integrated luminosity of 2.7 fb^{-1}, CDF has tested the $m_{t\bar{t}}$ spectrum for consistency with the SM prediction. The results are presented in table 6.1. They have concluded that there is no evidence of non-SM physics in the $m_{t\bar{t}}$ distribution of the cross section. Hence, whatever new physics explains the forward-backward asymmetry in $t\bar{t}$ production, it has to comply with all other measurements that are in agreement with the SM. Finally, measurements of the asymmetry for two regions of the top-antitop rapidity difference (ΔY) and for two regions of the invariant mass ($m_{t\bar{t}}$) were performed by the CDF collaboration in (74). The results are presented in table 6.2 together with the theoretical predictions. The asymmetry at high mass is 3.4 standard deviations above the NLO prediction for the charge asymmetry of QCD. Recently, the electroweak contributions to the asymmetry were re-analysed (79, 80) just to conclude that the observed mass-dependent forward-backward asymmetry still shows a 3σ deviation in the high mass region. Inclusion of corrections beyond NLO does not change this picture as well (81). The separate results at high mass and large ΔY contain partially independent information on the asymmetry mechanism. Therefore, a total of 14 observables were measured at the Tevatron. This set of experimental values will be used to investigate whether the complete set of effective dimension six operators is able to describe any new physics responsible for the observed discrepancies while retaining the measurements in agreement with the SM. Note that we will use only the 8 bins presented in table 6.1 of the 9 bins measured in (78) together with the total cross section. To those 9 observables we add the 4 observables shown in table 6.2 for the asymmetry together with the total asymmetry. Hence, we use 14 observables in total and it can be easily seen that they are all independent. Recently D0 (82) has measured $A^{t\bar{t}}_{FB}$ with 5.4 fb^{-1} of collected luminosity. As discussed in (83), their analysis does not observe a significant rise of the folded detector level asymmetry with respect to $m_{t\bar{t}}-$ and ΔY. Until these results are unfolded they can not be directly compared to the CDF ones, even if at the detector level they appear to be consistent within errors. We did not use the results (82) in our analysis.

Bin (GeV)	σ (CDF result) (pbarn)	σ (SM-NLO) (pbarn)
350-400	3.115 ± 0.559	2.450
400-450	1.690 ± 0.269	1.900
450-500	0.790 ± 0.170	1.150
500-550	0.495 ± 0.114	0.600
550-600	0.285 ± 0.071	0.400
600-700	0.230 ± 0.073	0.310
700-800	0.080 ± 0.037	0.100
800-1400	0.041 ± 0.021	0.036

Table 6.1: CDF measurements of $d\sigma/dm_{t\bar{t}}$ (78) (integrated in each bin). We bin-wise scale our SM result (at LO) to match the SM-NLO result to emulate a $m_{t\bar{t}}$ dependent k-factor for fitting. The SM-NLO values are extracted from the plot in (84).

Observables	CDF result	SM prediction
$A^{t\bar{t}}_{FB}(\lvert\Delta Y_t\rvert < 1.0)$	(0.026 ± 0.118)	(0.039 ± 0.006)
$A^{t\bar{t}}_{FB}(\lvert\Delta Y_t\rvert > 1.0)$	(0.611 ± 0.256)	(0.123 ± 0.008)
$A^{t}_{FB}(m_{t\bar{t}}-)$	(-0.116 ± 0.153)	(0.040 ± 0.006)
$A^{t}_{FB}(m_{t\bar{t}}+)$	(0.475 ± 0.114)	(0.088 ± 0.013)

Table 6.2: CDF measurements (74) and SM predictions for the Forward-Backward Asymmetry for two regions of ΔY_t and for two regions of $m_{t\bar{t}}$. $A^{t}_{FB}(m_{t\bar{t}}+)$ stands for $A^{t\bar{t}}_{FB}(m_{t\bar{t}} > 450$ GeV), while $A^{t}_{FB}(m_{t\bar{t}}-)$ stands for $A^{t\bar{t}}_{FB}(m_{t\bar{t}} < 450$ GeV).

There have been several attempts to explain this discrepancy. The most popular collection of models among theorists when trying to account for the Tevatron results are the ones with new gauge bosons, and in particular, axigluons, W' and Z' bosons (85, 86, 87, 88, 89, 90, 91, 92, 93, 94, 95, 96, 97, 98, 99, 100, 101, 102, 103, 104, 105, 106, 107, 108, 109, 110, 111, 112, 113, 114). Explanations in the framework of supersymmetric models were discussed in (115, 116). Other possible justifications for the inconsistency between theory and experiment in the asymmetry, while leaving the cross section for $t\bar{t}$ production within measured uncertainties, include s-channel coloured unparticle contributions (117) or s-channel new colour octet vector bosons contributions (118, 119, 120, 121, 122, 123), extra dimensions (124, 125, 126, 127), $SO(5) \otimes U(1)$ gauge-Higgs unification models (128), new heavy quarks (129) and diquark models (130, 131, 132, 133).

The search for resonances decaying into $t\bar{t}$ has also been carried out at the Tevatron (134) (see also (135)) with negative results. CDF has tested vector resonances with masses between 450 GeV and 1500 GeV with widths equal to 1.2 % of their mass. With 4.8 fb^{-1} of integrated luminosity they found no evidence of resonant production of $t\bar{t}$ candidate events. This result supports the argument of integrating out new heavy fields and strengthens the idea of adopting a model independent approach in explaining the measured asymmetry at the Tevatron. An independent approach, using dimension-six operators was already discussed in (136, 137, 138, 139, 140, 141, 142). In this work we propose to study the effect of dimension six flavour changing neutral current (FCNC) operators together with four fermion (4F) operators. In order to find the best set of parameters that fits the data we will use a Markov Chain Monte Carlo (MCMC) approach.

6.2 Parameter sampling method

In order to find the best set of parameters that fits the data we use a Markov Chain Monte Carlo (MCMC) approach (see section 2.5). We have constructed 10 chains, each started with a different random starting point. In all calculations of the top production cross sections we use the top mass as the renormalization and factorization scale. We take $m_t = 175$ GeV and to take into account the NLO corrections we have chosen a $k-$factor of 1.41 (76, 77). Further, we use a bin-wise scaling for the $m_{t\bar{t}}$ distribution to emulate the $m_{t\bar{t}}$ dependent $k-$factor. Once again we note that the 14 observables used as input in this study as measured by the CDF and D0 collaborations are all independent. These 14 observables are described in the previous section. We notice that the chains resulted in a very good convergence behaviour.

6.3 Strong and Electroweak operators

In order to simplify the notation we have replaced the original constants from the operators in the strong and electroweak sectors by α_i with $i = 1, 8$. This correspondence between constants α_i and the operators themselves is presented in table 6.3. As an example, the first operator $\mathcal{O}^{ut}_{uG\phi}$ would appear in the effective Lagrangian as

$$\frac{\alpha^{ut}_{uG\phi}}{\Lambda^2}\,\mathcal{O}^{ut}_{uG\phi} \quad . \tag{6.5}$$

Considering $\Lambda = 1$ TeV then α_1 is defined as

$$\alpha_1 = \frac{\alpha^{ut}_{uG\phi}}{\Lambda^2}\,\mathrm{TeV}^2 \tag{6.6}$$

which renders α_1 dimensionless. Similar definitions hold for the remaining α_i constants. Table 6.3 shows the relations between all the constants shown in the plots and the independent FCNC operators in the strong and electroweak sectors.

We first present our results for the Strong and Electroweak FCNC operators (SEFCNC). In fig 6.1 we present the χ^2 as a function of α_1, α_3 and α_7, keeping only one of the coefficients non-zero at a time. These three curves are representative of the χ^2 distribution behaviour for the complete set of SEFCNC operators. In fact, we can group operators α_1 and α_2 as for both $\alpha_1 = 0$ and $\alpha_2 = 0$ are the most favoured values. The operators that are preferentially non zero when taken one at a time are α_3, α_4, α_5 and α_6. In this case the preferred values are close to $\alpha_i = \pm 4$ (see α_3 in fig 6.1). Finally both α_7 and α_8 seem to be completely unconstrained as they have an almost flat χ^2 distribution for the entire α_i range presented.

Constant	Operator
α_1	$\mathcal{O}^{ut}_{uG\phi}$
α_2	$\mathcal{O}^{tu}_{uG\phi}$
α_3	$\mathcal{O}^{ut}_{uW\phi}$
α_4	$\mathcal{O}^{tu}_{uW\phi}$
α_5	$\mathcal{O}^{ut}_{uB\phi}$
α_6	$\mathcal{O}^{tu}_{uB\phi}$
α_7	$\mathcal{O}^{ut}_{\phi u} + \mathcal{O}^{tu}_{\phi u}$
α_8	$\mathcal{O}^{(3,tu)}_{\phi q} + \mathcal{O}^{(3,ut)}_{\phi q}$

Table 6.3: Relation between the constants presented in the plots and the independent FCNC operators in the strong and electroweak sectors.

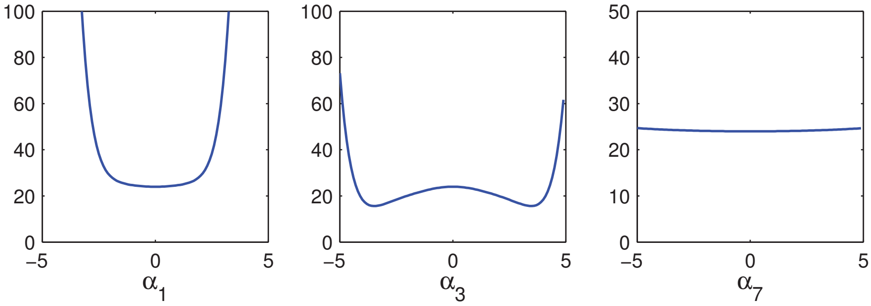

Figure 6.1: The χ^2 as a function of α_1, α_3 and α_7 with each parameter taken non-zero one at a time. The most favoured values are $\alpha_1 = 0$ and $|\alpha_3| \neq 0$. There are no preferred values for α_7.

We have then proceeded to scan over the 8 parameters (α_i, $i = 1-8$) using the MCMC method with flat prior as described in the previous section. The range for all parameters was chosen to be $-10 < \alpha_i < 10$. The complete set of 14 experimental observables, presented in the introduction, is used to calculate the χ^2 and hence the likelihood. After the likelihood mapping for the model, we have obtained the one dimensional likelihood distribution of the parameters which is presented in fig 6.2. It is clear from the figure that both α_1 and α_2, the FCNC operators stemming from the strong sector, are strongly constrained to be in the range -2 to 2. Operators α_3 to α_6, the chirality-flipping FCNC operators coming from the electroweak sector, have to be in the range -4 to 4.

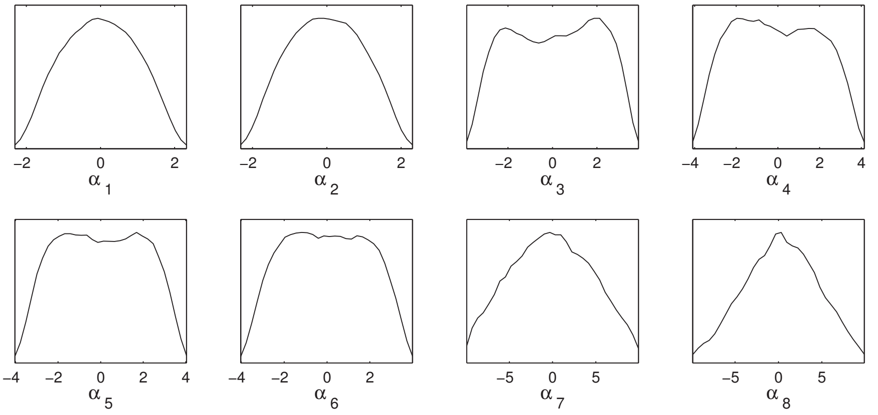

Figure 6.2: One dimensional likelihood distribution of the parameters α_1 to α_8 after the fit.

Finally the chirality-conserving operators from the electroweak sector, α_7 and α_8 are very mildly constrained and, as we will show later, the center-peaked shape of the distribution is only a reflection of the correlations of these parameters with the constrained ones. In order to understand how well the model fits into

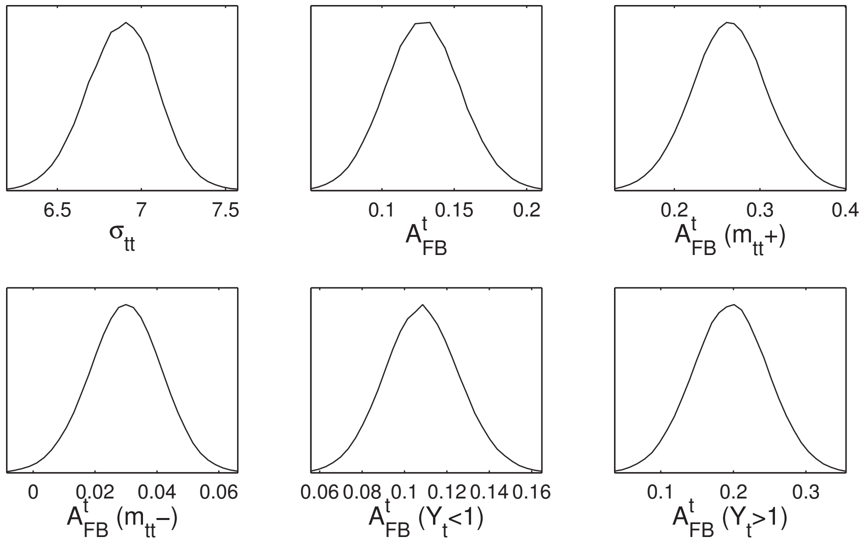

Figure 6.3: One dimensional likelihood distribution of the total cross section and all asymmetries after the fit.

the experimental observables we present in fig 6.3 the one dimensional likelihood distribution of the observables after the fit. Considering the central values of the observables presented in the introduction, we conclude that the SEFCNC set of operators prefer a lower value of the cross section while generating suitable values for the total forward-backward asymmetry. The values for $A^t_{FB}(m^+_{tt})$ and $A^t_{FB}(y^+_t)$ are below their experimental central values but well within the error bands. This shows that there is some compromise between the values of the parameters in the attempt to fit all observable simultaneously giving rise to a slight difference between the input observables and the ones originated from the posterior probability distribution functions (pdfs).

We now move to the study of the possible two-dimensional correlation between pairs of parameters. In fig 6.4 we present the two-dimensional correlation plots for the most representative scenarios. It is clear from the figure that there is no correlation between α_1 and α_2. Furthermore, these operators are very strongly constrained. On the other hand, there are several pairs of values that cannot be zero simultaneously. This is the case of (α_3,α_4) – the ones from $SU(2)$, (α_5,α_6) – the ones from $U(1)$ and (α_3,α_5), (α_4,α_6) – these are the $U(1)$ and $SU(2)$ combination where the indices of the operators O^{ij} are the same as for example in $\mathcal{O}^{ut}_{uW\phi}$ and $\mathcal{O}^{ut}_{uB\phi}$. For the pairs ($\alpha_4$,$\alpha_5$) and ($\alpha_3$,$\alpha_6$) the preferred values lie in the region $\alpha_4^2 = \alpha_5^2$ and $\alpha_3^2 = \alpha_6^2$ respectively. This happens to the combination of $SU(2)$ and $U(1)$ operators with the ij indices exchanged. Finally operators α_7 and α_8 do not appear to be much constrained when plotted against the remaining operators. There are however mild correlations - if we take for instance the pair (α_4,α_7) it is clear that for $\alpha_4 < 0$, α_7 prefers to be positive and if $\alpha_4 > 0$, α_7 prefers to be negative.

With the hints from fig 6.4 about which parameters prefer to be non-zero after the fit, we have tried to understand if one could make a more strong statement about the appearance of new physics related to the Strong and Electroweak dimension six FCNC operators. We note that the contributions of α_7 and α_8 are irrelevant because the change in likelihood is very small when these parameters are varied as shown in figures 6.1 and 6.2. On the other hand, α_1 and α_2 can lead to a large change in the likelihood - the preferred points are therefore $\alpha_1 = 0 = \alpha_2$. Hence, we look at the most relevant combinations of the remaining

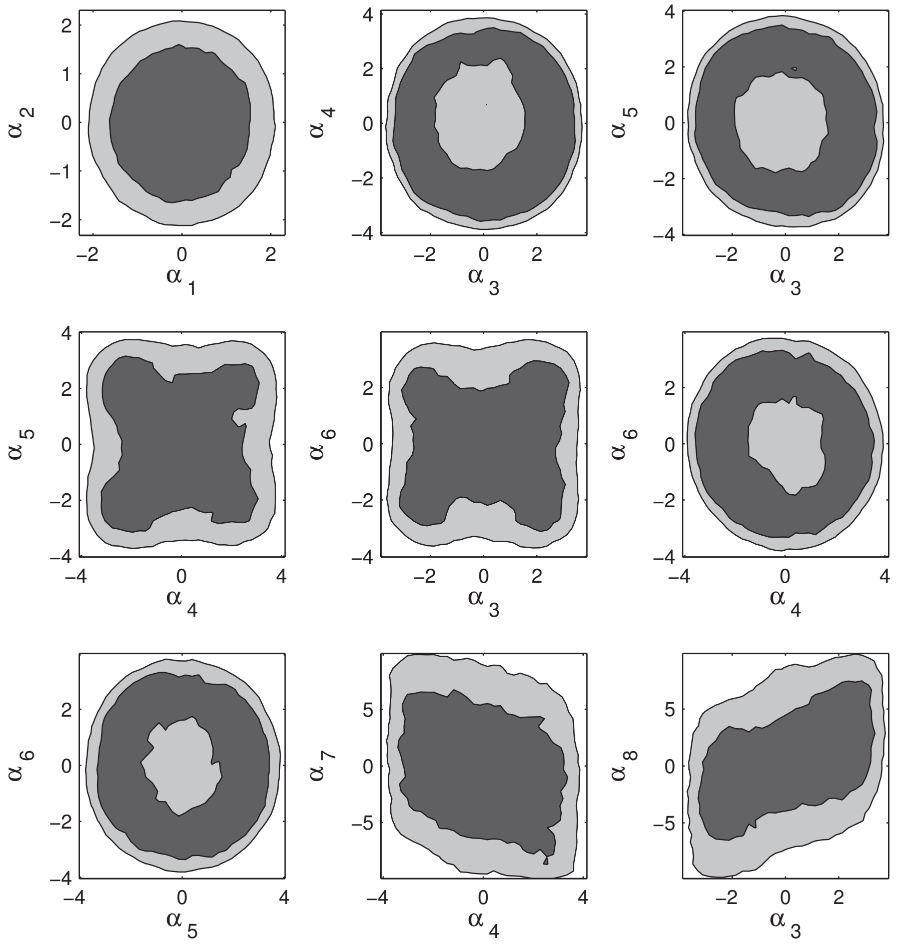

Figure 6.4: Two-dimensional correlation plots for the strong and electroweak FCNC parameters. Only the most relevant correlations are shown. The shaded areas are the ones where the values of α_i reach their highest probability - the darker ones represent 95 % CL while the lighter ones are for 68 % CL

parameters. The likelihood distributions for those combinations are shown in fig 6.5. It is clear that all the correlated pairs of parameters prefer to be non-zero simultaneously, like for instance (α_3,α_4), which have a peak between 5 and 10. Again, the likelihood plot for $\alpha_3^2 - \alpha_6^2$ peaks at 0 indicating that $\alpha_3^2 = \alpha_6^2$ is the preferred parameter choice as also seen in fig 6.4. However, the most interesting case is the likelihood for $\alpha_3^2 + \alpha_4^2 + \alpha_5^2 + \alpha_6^2$ – in this case we are certain that at least one of the four parameters has to be non-zero in order to fit the data. This

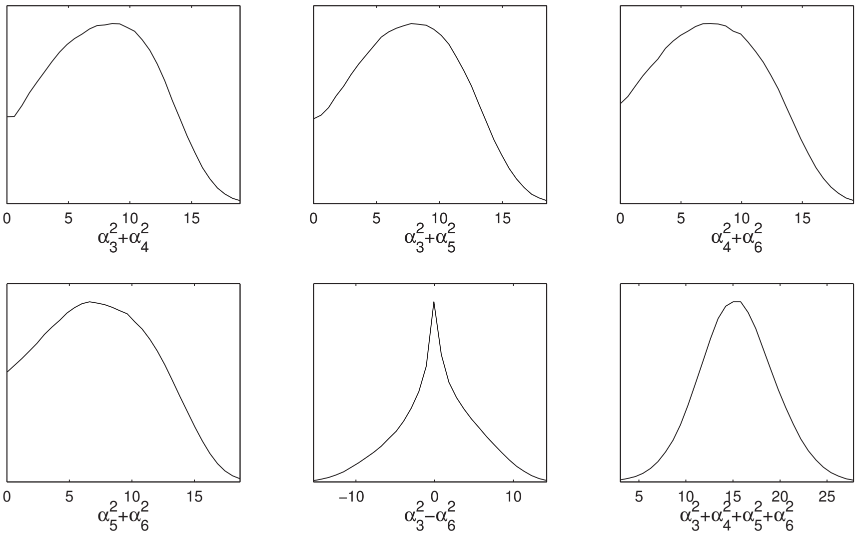

Figure 6.5: Likelihood distributions for the most relevant combination of parameters.

is a very strong statement because it means that new physics coming from these operators can help curing the asymmetry discrepancy and in order to solve it at least one of the operators has to be present.

In fig 6.6 we present the two-dimensional correlation between several observables after the fit. In the first row one can see that there is a negative correlation between asymmetries and total cross section. Hence, to get the right asymmetries the cross section moves to its lower preferred value. On the other hand, all asymmetries have positive correlations and are highly correlated – if one of them increases the other increases as well. Therefore, there is a tension between cross sections and asymmetries that reflects the difficulty of fitting all the observables with the set of SEFCNC operators. Nevertheless, a non-zero contribution from the operators α_3 to α_6 provides a better fit than the SM one.

In table 6.4, we show the best fit values along with 68% and 95% Bayesian confidence intervals (BCI) for all the parameters and selected observables. The BCIs are derived from the one-dimensional marginalized distributions, as shown in figures 6.1 and 6.2, while the best fit point is the one with least $\chi^2 = 14.2$. Thus, the best fit point does not need to be at the center of the marginalized

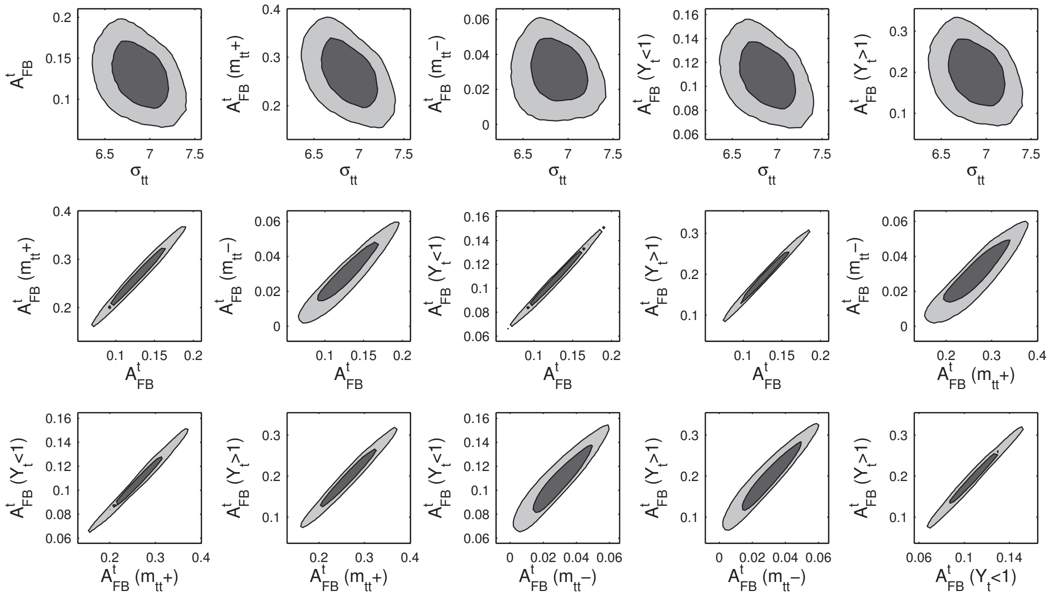

Figure 6.6: Two-dimensional correlations between cross sections and asymmetries and between the different asymmetries.

BCIs. For the SM we have $\chi^2 = 24.0$ and it is the sizeable contributions from $\alpha_3, ..., \alpha_6$ operators that lead to the reduction in the χ^2 for our fits. We again note that the combination $\alpha_3^2 + \alpha_4^2 + \alpha_5^2 + \alpha_6^2 > 7.5$ with 97.5% CL, i.e. it is almost certainly non-zero.

We have also listed the posterior BCI for the cross section and the asymmetries in table 6.4. The best fit value of the total cross section, and also the 95% BCI, are somewhat smaller than the measured central value. The same trend is observed for all the asymmetries except for the integrated asymmetry $A^{t\bar{t}}_{FB}$ which is correctly reproduced and the $A^t_{FB}(m_{tt})$ asymmetry which is most likely positive in our model. As previously discussed, the reduction of the cross section values and asymmetries is a result of the negative correlations between them.

6.4 Four fermion operators

We now turn our attention to the four-fermion (4F) effective Lagrangian. We should start by mentioning that recently (143), a complete calculation of the

		68% interval		95% interval	
Quantities	Best fit	lower	upper	lower	upper
α_1	-0.548	-1.081	1.066	-1.797	1.793
α_2	-0.449	-1.102	1.053	-1.812	1.781
α_3	-2.024	-2.222	2.293	-3.257	3.288
α_4	2.913	-2.327	2.250	-3.443	3.446
α_5	2.403	-2.210	2.254	-3.334	3.379
α_6	0.742	-2.172	2.163	-3.330	3.317
α_7	-3.318	-5.257	4.901	-8.763	8.536
α_8	-3.146	-4.106	4.647	-7.931	8.148
σ_{tt}	6.817	6.670	7.093	6.453	7.299
$A_{FB}^{t\bar{t}}$	0.153	0.102	0.155	0.078	0.181
$A_{FB}^{t}(m_{t\bar{t}}-)$	0.044	0.018	0.041	0.006	0.053
$A_{FB}^{t}(m_{t\bar{t}}+)$	0.310	0.220	0.309	0.177	0.354
$A_{FB}^{t}(Y_t < 1)$	0.126	0.090	0.126	0.074	0.144
$A_{FB}^{t}(Y_t > 1)$	0.245	0.143	0.248	0.093	0.299
$\alpha_3^2+\alpha_4^2+\alpha_5^2+\alpha_6^2$	18.91	11.43	19.39	7.50	23.46

Table 6.4: Best fit values and the Bayesian confidence intervals (BCI) for parameters and the observables.

forward-backward asymmetry and of the total cross section of top quark pair production induced by 4F-operators was performed for the Tevatron up to $O(\alpha_s^2/\Lambda^2)$. The results show that next-to-leading order QCD corrections can change both the asymmetry and the total cross section by about 10%. As discussed in section 4.5.2, there are a total of 12 independent operators for the study of $t\bar{t}$ production and under the conditions described previously which mainly means we are only considering the u-quark contribution in the initial state. We have scanned linearly over the 12 parameters from the 4F-Lagrangian using the MCMC method. The range chosen for all parameters was again from -10 to 10. In fig 6.7 we present the likelihood distribution for all the 4F parameters, after the fit. A few comments are in order. First, operators in one row can only interfere with parameters in the same row. Second, only parameters in the first row interfere with the SM Lagrangian and consequently the main contribution for the asymmetry has to come from the parameters presented in the first row. This is clear from the plot as the four distributions in the first row are the only asymmetric ones - all

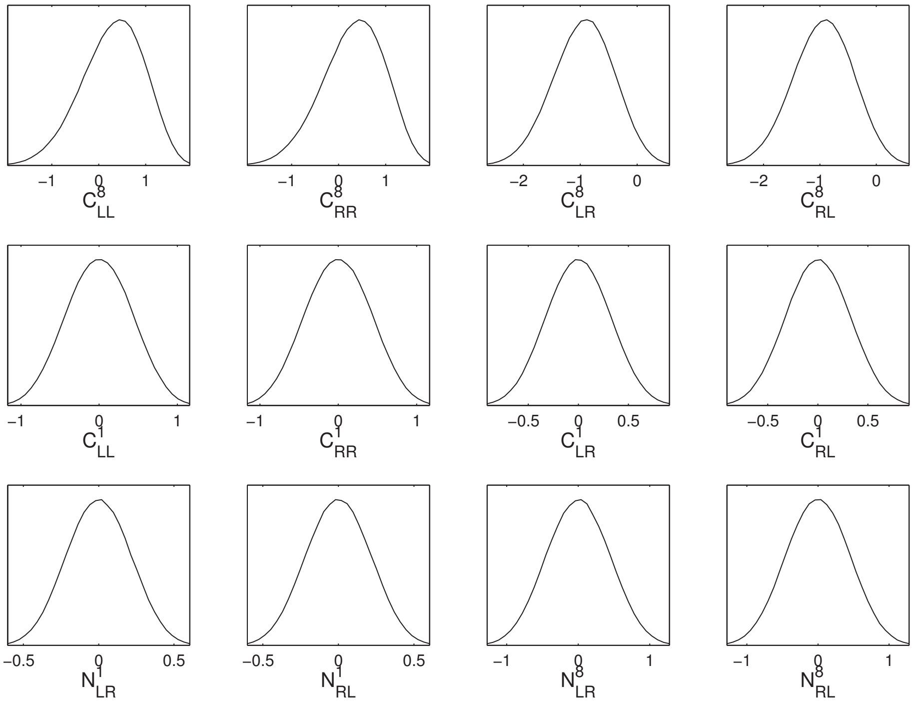

Figure 6.7: Likelihood distribution for the parameters of the four-fermion Lagrangian, after the fit.

other parameters in the following two rows have not only symmetric distributions but they show that the preferred value of these parameters is zero. However, in the case of 4F operators the cross sections and the asymmetries depend only on six combinations of the parameters. Therefore we have decided to present in fig 6.8 the likelihood distribution for those combinations together with the likelihood distributions of the total cross section and a few selected asymmetries. The relation between the new parameters and the original ones present in the 4F

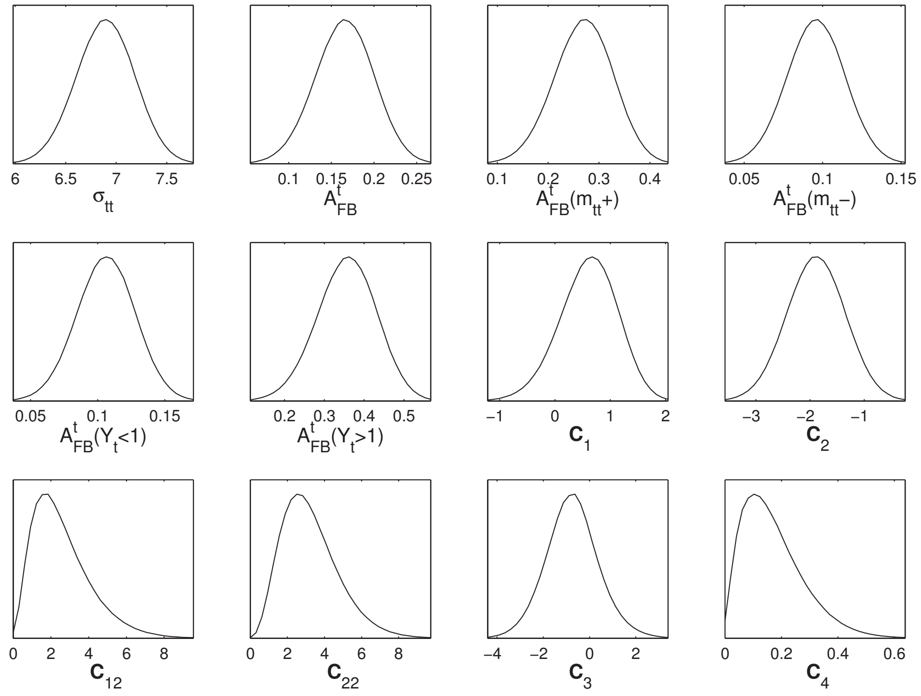

Figure 6.8: Likelihood distribution for the total cross section and for the asymmerties and for the six independent combinations of the 4F Lagrangian parameters, after the fit.

Lagrangian is

$$\begin{aligned}
C_1 &= C^8_{LL} + C^8_{RR} \\
C_2 &= C^8_{LR} + C^8_{RL} \\
C_{12} &= (C^8_{LL})^2 + (C^8_{RR})^2 + \frac{9}{2}\left[(C^1_{LL})^2 + (C^1_{RR})^2\right] \\
C_{22} &= (C^8_{LR})^2 + (C^8_{RL})^2 + \frac{9}{2}\left[(C^1_{LR})^2 + (C^1_{RL})^2\right] \\
C_3 &= C^8_{LL}C^8_{LR} + C^8_{RR}C^8_{RL} + \frac{9}{2}\left[C^1_{LL}C^1_{LR} + C^1_{RR}C^1_{RL}\right] \\
C_4 &= (N^1_{LR})^2 + (N^1_{RL})^2 + \frac{2}{9}\left[(N^8_{LR})^2 + (N^8_{RL})^2\right] \quad . \qquad (6.7)
\end{aligned}$$

It is clear that the experimental observables are well described by the fit. Regarding the parameters, the most relevant fact, that could already be inferred from fig 6.8, is that C_2 prefers to be non-zero and, for the same reason, the likelihood of both C_{12} and C_{22} peaks at 1. A similar trend can now be seen in the two-dimensional correlations presented in fig 6.9. It is clear that at 95 % CL the value zero is excluded in the top right plot. In the top left plot the value zero is still inside the 95 % CL contour. Regarding the correlations between cross section and asymmetries, and between pair of asymmetries, after the fit, the general trend is very similar to the one presented in the previous section for the strong and electroweak FCNC operators. Therefore we will make no further comments on those correlations.

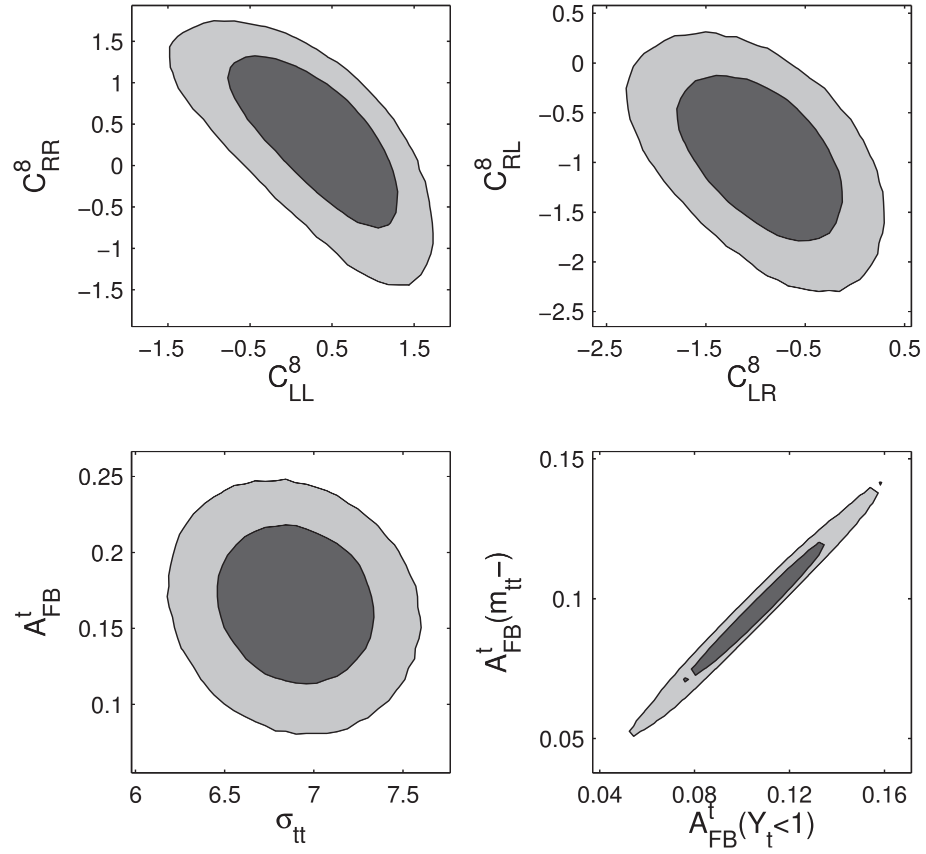

Figure 6.9: Two-dimensional correlations between the parameters that can give a significant contribution to the asymmetry. Also shown are typical examples of the correlations between cross section and asymmetries and between two asymmetry observables.

In fig 6.10 we present two dimensional correlations between C_1 and C_2 and

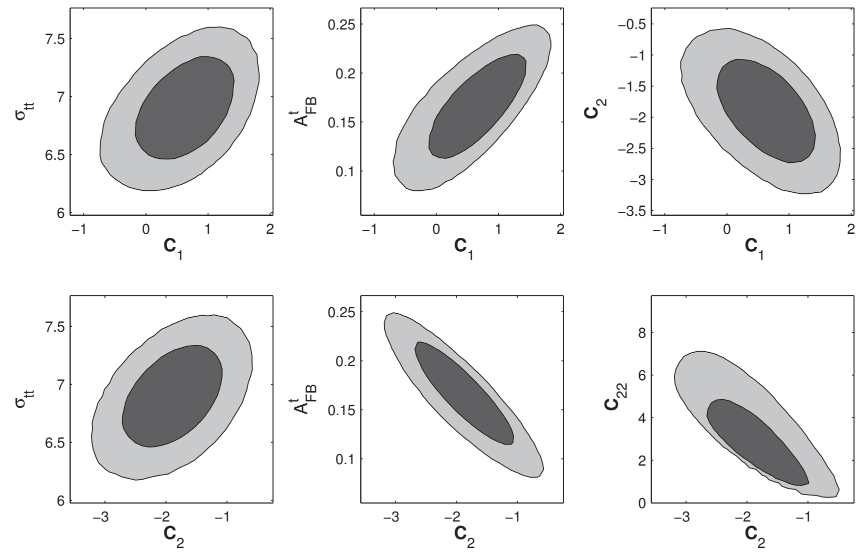

Figure 6.10: Two-dimensional correlations between the parameters C_1 and C_2 and the total cross section, total asymmetry and the parameter C_{22}.

the total cross section, total asymmetry and the parameter C_{22}. We see that while C_1 is positively correlated with both the cross section and the asymmetry, C_2 is positively correlated with the cross section but negatively correlated with the asymmetry. Furthermore C_1, C_2 and C_{22} are all negatively correlated with each other. Finally, we conclude that either C_2, C_{22} or both have to be non-zero which is not surprising given the relations presented in eqs. (3.5).

In table 6.5, we show the best fit point along with 68% and 95% BCIs. The best fit point is the one with least $\chi^2 = 6.28$. As seen in figure 6.9, only C^8_{AB} operators have relevant contributions to both the asymmetries and the cross sections. The weak operators, C^1_{AB} do not interfere with the SM diagrams, contributing therefore more to the cross sections and much less to the asymmetries. Thus, they are strongly constrained through the measured values of the cross sections. The N^i_{AB} operators contribute only to the cross sections and consequently are also strongly constrained and irrelevant as possible new physics contributions.

Again, due to the negative correlations between the cross section and the asymmetries, there is a slight tension in the fits. This leads to a mild preference for lower values of the total cross section. The asymmetries, on the other hand,

		68% interval		95% interval	
Quantities	Best fit	lower	upper	lower	upper
C^8_{LL}	0.915	-0.385	0.968	-1.119	1.466
C^8_{RR}	0.418	-0.368	0.980	-1.104	1.476
C^8_{LR}	-0.934	-1.487	-0.406	-2.031	0.064
C^8_{RL}	-0.963	-1.488	-0.406	-2.035	0.071
C^1_{LL}	-0.136	-0.420	0.420	-0.794	0.792
C^1_{RR}	0.002	-0.422	0.419	-0.795	0.793
C^1_{LR}	-0.082	-0.316	0.316	-0.606	0.606
C^1_{RL}	0.049	-0.316	0.318	-0.606	0.607
N^1_{LR}	0.057	-0.212	0.212	-0.405	0.405
N^1_{RL}	-0.036	-0.212	0.212	-0.405	0.404
N^8_{LR}	0.070	-0.442	0.441	-0.848	0.846
N^8_{RL}	0.040	-0.446	0.443	-0.852	0.850
σ_{tt}	7.054	6.601	7.181	6.315	7.453
$A^{t\bar{t}}_{FB}$	0.191	0.131	0.199	0.096	0.231
$A^t_{FB}(m_{tt}-)$	0.107	0.077	0.114	0.059	0.132
$A^t_{FB}(m_{tt}+)$	0.321	0.211	0.327	0.151	0.379
$A^t_{FB}(Y_t < 1)$	0.121	0.084	0.128	0.063	0.148
$A^t_{FB}(Y_t > 1)$	0.420	0.281	0.430	0.205	0.496

Table 6.5: The table of best fit values for the 4F case along with 68% and 95% BCI.

are reasonably well reproduced. We note that, $A^t_{FB}(m_{tt})$ prefers to be positive with 4F operators.

6.5 Bounds on the effective operators

In this section we discuss all possible bounds on the dimension six effective operators described in the previous sections. Our goal is to ascertain whether the values of the couplings multiplying each operator, that could explain the measured asymmetry discrepancy, are still allowed by the available experimental data. We start by considering the dimension six FCNC operators. We have seen above that the only effective operators stemming from the electroweak sector were likely to fit the Tevatron data on the top quark better than the SM. In fact, it is the sizeable contributions from the $\alpha_3, ..., \alpha_6$ operators that lead to the reduction in the χ^2 for our fits. We again note that the combination $\alpha_3^2 + \alpha_4^2 + \alpha_5^2 + \alpha_6^2 > 7.5$ with 97.5% CL, it is almost certainly non-zero. Therefore, we have now to focus on the bounds for operators α_3 to α_6 to understand if such a high value of the constants is not in contradiction with experimental data from other sources.

A very complete analysis on the electroweak FCNC operators was performed in (58) using not only all available data from B physics but also the data from direct FCNC top decays (the later will be updated in this work) [1]. The bounds obtained on the operators taken one at a time are (58) $\alpha_3^2 < 0.81$, $\alpha_4^2 < 0.011$ and $\alpha_6^2 < 0.096$ while the best bound on α_5 was shown to come from the direct constraint on $BR(t \to qZ)$ and $BR(t \to q\gamma)$. Therefore, to satisfy $\alpha_3^2 + \alpha_4^2 + \alpha_5^2 + \alpha_6^2 > 7.5$ one needs $\alpha_5^5 \approx 6.5$. However, such a value of α_5 would imply that $BR(t \to qZ) \approx 3.7\%$ and $BR(t \to q\gamma) \approx 6.3\%$. The most recent direct bounds on $BR(t \to q\gamma)$ and $BR(t \to qZ)$ are the ones from the Tevatron, 3.2% (148) and from the LHC, 1.1% (149), respectively. Hence, it is clear that such high values of α_5 are disallowed by Tevatron and LHC data on the direct searches for FCNC top decays with a photon or a Z-boson in the final state. Furthermore, indirect bounds from HERA, where bounds on cross sections are converted on bounds on the branching ratio, set a limit $BR(t \to q\gamma) \lesssim 0.5\%$ (150).

---

[1] Other analysis based on B physics observables and electroweak precision constraints were also performed in (59, 144, 145, 146, 147) leading to similar conclusions.

Also, a combined study on B physics and Tevatron data on top quark production cross section places an indirect bound on the sum of the FCNC branching ratios forcing them to be below the percent level (151). In conclusion, experimental data from very different sources constrain the operators that could explain the asymmetry in such a way that we consider that it is very unlikely that the observed discrepancy could be explained by these operators.

Contrary to the dimension six FCNC operators, there are no useful bounds on the four fermion operators involving two top quarks and this is even more so if the top is right-handed. Therefore, only the LHC could place constraints on these operators. However the values of the constants C_i and C_{ij} that could help explain the discrepancy give an extra cross section that is always below 10 pb even for $\sqrt{s} = 14$ TeV. Hence, given the error of $t\bar{t}$ production cross section it is very unlikely that these operators will be constrained in the near future.

6.6 Discussion and conclusions

In this chapter we have used a dimension six Lagrangian with FCNC interaction together with four-fermion operators to gain some insight in understanding the discrepancy between the experimental values obtained for the top pair production asymmetry and the corresponding SM predictions. We have built a minimal set of operators and we have used an MCMC approach to find the best simultaneous fit of all independent operators to the available data. Our conclusions regarding which operators give the best fit are as follows:

- Strong FCNC operators with coefficients $\alpha_{1,2}$ are most likely close to zero in order do fit the cross section values.

- Regarding Electroweak FCNC operators with coefficients α_3 to α_6 we conclude that one of them must be non-zero - the sum of the operators $\alpha_3 + \alpha_4 + \alpha_5 + \alpha_6$ was shown to be larger than 7.5 with 97.5 % CL.

- Electroweak FCNC operators with coefficients $\alpha_{7,8}$ are not relevant.

- Bounds on electroweak FCNC operators reveal that it is very unlikely that the asymmetry can come from new physics described by these operators -

in fact, the relation $\alpha_3 + \alpha_4 + \alpha_5 + \alpha_6 > 7.5$ is disallowed by the existing experimental bounds on the operators.

- Four-fermion operators with coefficients C^8_{AB} contribute to the asymmetries while the ones with coefficients C^1_{AB} give small contributions; the 4F combinations C_1, C_2, C_{12}, C_{22} contribute to the asymmetries; we should note that for the best fit point only C^8_{LR} and C^8_{Rl} are not consistent with zero at one sigma level.

- Four-fermion operators with coefficients N^i_{AB} contribute to the cross sections only.

- There is in all cases some tension between cross section and asymmetries when a simultaneous fit to all observables is performed.

- The contribution of 4F operators to the cross-section at LHC7 is of the order ±1.5 pb, which is allowed by the present estimates of the cross-section (152).

It is important to ask how do we figure out which operators are actually responsible for the asymmetry. To that end we note that the asymmetry, although called forward-backward, is actually a C-odd and for CP conserving interaction that can therefore be created by P-odd interactions as well. Further, our operators contribute to the asymmetry in two ways: kinematically and dynamically. The t-channel diagrams with FCNC interaction naturally originate more top quarks in the direction of the incoming u-quark leading to a positive asymmetry as measured by the CDF collaboration. This coupling does not need to be chiral to produce the required asymmetry, although our operators are chiral. For the 4F case, there is no such kinematical asymmetry generation and it is dominantly generated by the unbalance between left and right chiral operators interfering with the SM contribution. Thus, in both cases, we have the presence of chiral interaction, which also incarnates in the form of polarization of the produced top-quark. Hence, a study of such polarization effects (153) as a function of rapidity will be able to provide a probe of possible new physics. Further, our operators are also constrained by B-physics observables and for simplicity we have not accounted for them in our MCMC. We have nevertheless used the constraints from B-physics to conclude that FCNC operators are unlikely to account for the measured asymmetry at the Tevatron. We should stress that low mass mediators (like the Z') are not included in our study. In fact, the effective operator approach integrates out all interaction mediators, which is allowed only if they are heavy. Previous studies show that the low mass mediators are more successful in generating a large asymmetry while keeping the SM production cross section within the experimental measured values. Our work strengthens this conclusion.

To conclude, we remark that the $A_{FB}^{t\bar{t}}$observed at CDF can be casted in terms of dimension-six operators and we need more observables, from top-polarization and B-physics, to constrain them due to the multitude of these operators.

7

MEtop

This chapter summarises the work published with the reference:
Eur.Phys.J. **C**72, 2222 (2012).

7.1 Introduction

In this chapter we present a tool to measure FCNC effects related to the top quark at the production level. More evolved top FCNC searches can only be performed if a dedicated generator for top FCNC studies is available. Events for direct top production $pp(gu+gc) \to t$ studies can be generated at leading order by the PROTOS generator (154), the TopReX generator (155) and also by multi-purpose generators such as CompHEP (156) (see for instance the analysis in (157, 158)), CalcHEP (159) or MadGraph (160). We considered that it was both necessary and timely to make available a generator for top FCNC physics that included a larger set of FCNC operators together with a larger set of physical processes at the production level. This is the purpose of the MEtop event generator.

The MEtop main process is direct top production, $pp(gu + gc) \to t$, but calculated at NLO. NLO direct top was implemented by adopting an effective NLO approximation as described in (18). Besides direct top, MEtop can be used to generate events at LO for all FCNC processes with a top and a gluon or any quark other then the top in the final state. We plan to include other processes like $pp \to tV$, with $V = \gamma, Z, W$ in the near future. From the theoretical point of view we will adopt the effective operator formalism as described in chapter 4. We use a set of dimension six effective operators always involving at least one top-quark. Due to computational limitations and efficiency requirements, it is not possible to include all effective operators described in chapter 4. Therefore, MEtop comes with several choices of packages where different sets of effective operators are available. The set of operators is classified in three different groups: strong, electroweak and four-fermion (4F) operators. The list of operators in each package is presented in appendix A. Furthermore, the *User Manual* is presented in appendix B.

7.2 Direct top @ LO

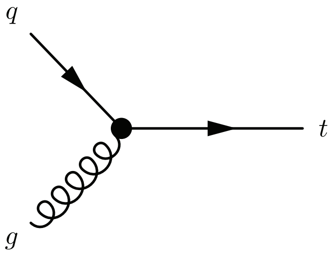

Figure 7.1: Feyman diagram for FCNC Direct top production, $q = u, c$.

In figure 7.1 we show the Born diagram for FCNC Direct top production. This is the main considered process for strong FCNC top studies, and it can be parametrized through the effective operator of equation (4.12) given by:

$$\mathcal{O}_S = g_s \frac{k^i}{\Lambda} \bar{t} \sigma^{\mu\nu} T^a (f^i + i h^i \gamma_5) q G^a_{\mu\nu} \quad , \quad i = u, c. \tag{7.1}$$

The operator is parametrized by the factor k^i, which works here as a coupling constant. From the operator $\mathcal{O}_S$, the Feynman rules are extracted and the squared and averaged amplitude results in:

$$\overline{|\mathcal{M}^B|^2} = \frac{8\pi\alpha_S}{3} \left(\frac{k^i}{\Lambda} \right)^2 m_t^4. \tag{7.2}$$

The corresponding cross section is given by:

$$\hat{\sigma}^B(z) = \frac{8\pi\alpha_S}{3s}\left(\frac{k^i}{\Lambda}\right)^2 m_t^2\delta(1-z), \tag{7.3}$$

where the variable s is the usual Mandelstam definition: $s = (k_1 + k_2)^2$, with k_1 and k_2 the incoming momenta, and $z = m_t^2/s$. The total cross section is obtained by using equation (2.17). In table 7.1 we show the total cross section for the LHC running at 8 TeV, and Tevatron at 2 TeV, with $k^{u,c} = 0.01$. As we can see from equation (7.3), the total cross section will depend on the k^i value we use. As mentioned above this variable parametrizes $\mathcal{O}_S$, and it is from its experimental bounds that FCNC interactions constraints are found. Today's most recent boundaries on $k^{u,c}$ were measured by the ATLAS collaboration and are show in table 7.2. The limits were converted for $k^{u,c}$ defined as in chapter 4. We also included the corresponding limits on the FCNC branching ratios $Br(t \to ug)$ and $Br(t \to cg)$, calculated with NLO precision in (161). The results in table 7.2 were obtained with the use of the Monte Carlo event generator PROTOS (154), which is today the most recent available tool that simulates FCNC Direct top production events. We will show that MEtop can also produce this type of events.

Subprocess	Tevatron @ 2Tev	LHC @ 7 Tev
$ug \to t$	0.57	6.12
$cg \to t$	0.028	0.91

Table 7.1: FCNC Direct top LO cross sections for $k^{u,c} = 0.01$. The calculation was includes $\bar{t}$ production.

$k^u < 4.8 \times 10^{-3}$	$Br < 5.7 \times 10^{-5}$
$k^c < 11.3 \times 10^{-3}$	$Br < 2.4 \times 10^{-4}$

Table 7.2: $k^{u,c}$ limits measured in (14).

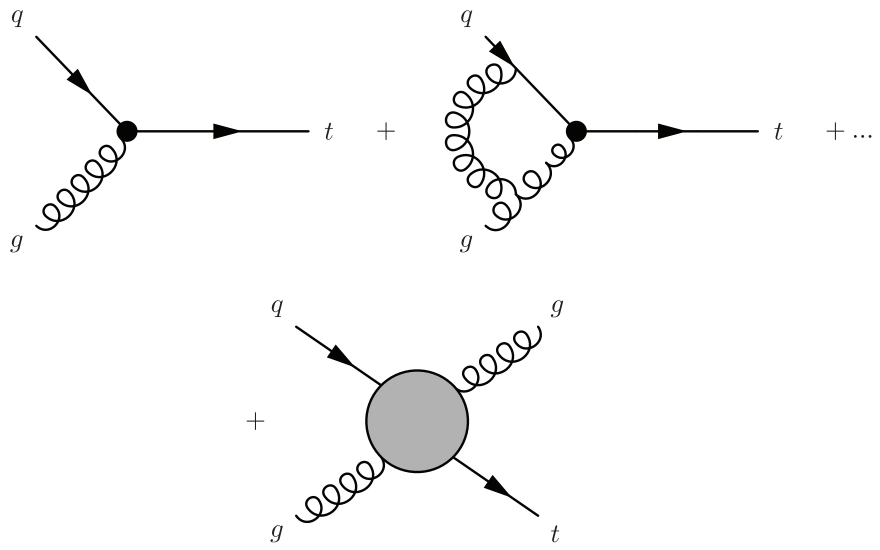

Figure 7.2: Feyman diagrams for NLO FCNC Direct top production, $q = u, c$.

7.3 Direct top @ NLO

As explained in section 2.3.2, the cross section calculation is based on a series expansion in the coupling constant α_S (for QCD as our QFT), where the first term is what we have been calling LO cross section. In order to include higher precision, the next term in the series must be considered. This will be the NLO calculation. In figure 7.2 we show a summary of all extra diagrams. In it, we show the same Born diagram dealt in the previous section, the virtual diagrams and a extra group, which is the real radiation process. As we saw in section 2.3.2, this extra process must be added in order to cure the infrared divergences originated from the inclusion of virtual diagrams. Additionally, since we are now including the extra parton radiation, and integrate it in the full $2 \to 2$ process phase-space, the final result is an inclusive cross section calculation, rather than pure exclusive. On top of this, since experimentally the radiated real gluon will be indistinguishable from, for example, an external final parton, one must add all possible FCNC process contributions with the final state $t + q$, where $q = u, c, d, s, b$ (together with the respective antiparticles). This processes are summarised in figure 7.3. The NLO calculation was taken from (51), and we show in table 7.3 the LO and NLO results for the LHC running at 7 TeV, with

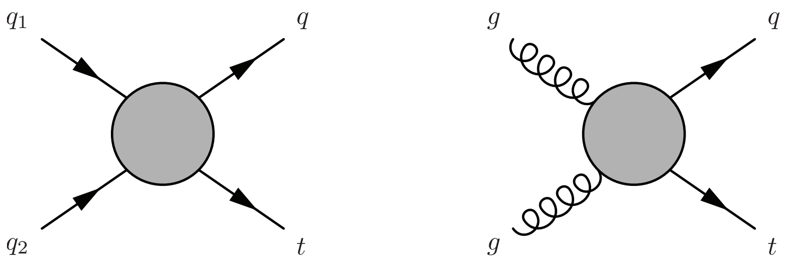

Figure 7.3: Feyman diagrams for $p, p \to t, q$ with $q = u, c, d, s, b$.

a top mass of $m_t = 173.1$ GeV. This NLO result does not include the $t + q$ processes. As we can see, the NLO result bring an accountable enhancement to the LO result. For the shown results the improvement of the $ug \to t$ cross section is 43%, while for $cg \to t$ is 84%. This is an accountable improvement, since from the experimental point of view, it means that by considering a K-factor only, a gain in the branching ratio limit of the same order will be obtained. In table 7.4 we show the FCNC top production cross sections but for the $t + q$ case.

Subprocess	LO	NLO
$ug \to t$	6.12	8.74
$cg \to t$	0.91	1.67

Table 7.3: FCNC Direct top LO and NLO cross sections for $k^{u,c} = 0.01$ and LHC @ 7 TeV. The calculation includes $\bar{t}$ production.

Subprocess	$k^u = 0.01$	$k^c = 0.01$
$p, p \to t, q$	1.12	0.40

Table 7.4: FCNC $t + q$ with $k^{u,c} = 0.01$ at the LHC @ 7 TeV and $PT_{cut} = 10$ GeV. The calculation includes $\bar{t}$ production.

7.4 Effective NLO approximation

In this approach, a merging scheme between 2 → 1 and 2 → 2 events is performed, where each process will separately populate two distinct but joint regions of the phase-space. A resolution parameter must then be defined, which in the present case is the cut in transverse momentum of the top quark applied to the real radiation process. P_{T}^{cut} will then play a role of a matching variable, P_{T}^{match}. The phase-space region for small P_{T} will be described by the 2 → 1 process and the subsequent parton shower (PS) mechanism, whereas the hard P_{T} region will be described by the 2 → 2 process. One must then just make sure that the transition is done in a smooth way. The virtual corrections are included via a K-factor applied to the cross section of the 2 → 1 process. We assume this to be a good approximation because the kinematics of the Born and Virtual configurations of the direct top process are identical. The events will then be generated according to the following relation

$$\sigma_{NLO} = K\sigma_{LO}(P_{\mathrm{T}}^{PS} < P_{\mathrm{T}}^{match}) + \sigma_{Real}(P_{\mathrm{T}} > P_{\mathrm{T}}^{match}) \tag{7.4}$$

where σ_{LO} is the tree-level direct top contribution, σ_{Real} is the real radiation part, K is the K-factor and P_{T}^{PS} and P_{T}^{match} are the transverse momentum of the first PS emission and the integration cut of the real radiation process, respectively. Once the direct top events are produced, they will be radiated through a radiator like the one in PYTHIA (162). In order to avoid double counting, the matching must ensure that the first PS emission from the 2 → 1 process will not fall within the 2 → 2 configuration phase-space. There are two ways of accomplishing it: either by vetoing all radiated 2 → 1 events that would be within the 2 → 2 configuration phase-space or simply by limiting the phase-space region of the radiated 2 → 1 events to the boundaries defined by the resolution variable. We choose to adopt the later.

In order to follow this approach, one must ensure that the PS mechanism added to the generated events from the Born configuration will populate the region with $P_{\mathrm{T}} < P_{\mathrm{T}}^{match}$ which can be assured using a PT-ordered shower [44], available in both current PYTHIA versions 6.4 and 8.1. We therefore assume that

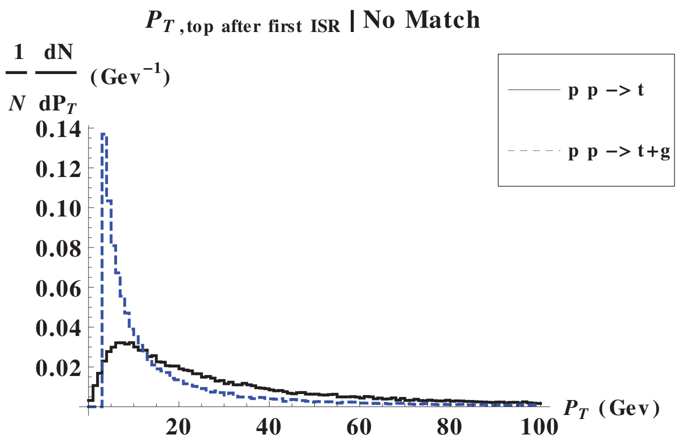

Figure 7.4: P_T distribution of the top quark for $\sqrt{s} = 7$ TeV. The black solid line is for direct top production after the first branching in ISR, with starting scale of m_t. The blue dashed line is for the hard process top+gluon production.

the generated events will be showered by a PT-ordered mechanism. Therefore we start by calculating the three cross sections from equation (7.4), with $P_\mathrm{T}^{cut} = P_\mathrm{T}^{match}$ for the $2 \rightarrow 2$ process. For the σ_{NLO} cross section we have used the expressions from (51), where the top quark is on-shell. The tree-level direct top and top+gluon amplitudes were generated with CalcHEP where the top quark and the W decays were included in order to preserve spin correlations. The cross sections are then calculated with the Cuba library. Hence, the K factor is calculated "on the fly" for each sub-process. After extracting the K-factor, the events are generated weighed according to equation (7.4). The PS starting scale can then be configured to start the branching in P_T^{match} for the $2 \rightarrow 1$ events configuration, which in MEtop is done by preparing the .lhe files to be used by PYTHIA. A short remark is in order - in the $2 \rightarrow 1$ configuration, no meaningful FSR from the top quark can be present due to its large mass. Hence, we consider a good approximation to take only ISR into account.

In figure 7.4, the black solid line represents the P_T distribution of the top quark in direct top production, after the first branching in ISR, with starting scale of m_t. In the same figure, the blue dashed line represents the hard process: top+gluon production. As described previously, P_T is the kinematical variable chosen to match the two processes avoiding double counting in the low P_T region.

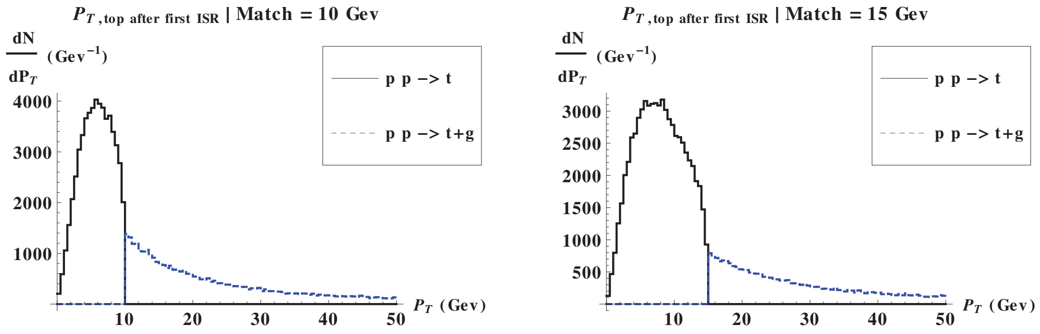

Figure 7.5: P_{T} distribution of top quark after the first ISR branching with a P_{T}^{match} of 10 GeV (left) and 15 GeV (right).

In figure 7.5 we present the P_{T} distribution of the top quark after the first ISR branching with a P_{T}^{match} of 10 GeV (left) and 15 GeV (right). The natural criterion to determine the value of the P_{T} matching parameter in the effective NLO approximation is the smoothness of the transverse momentum distribution. There are no significant differences when the value of P_{T}^{match} is varied in the 5 GeV to 20 GeV range. As can be seen in figure 7.5, there is never a completely smooth transition between the two sets of events. This only occur at partonic level as we will show that the smoothness is regained when the full shower is performed. Nevertheless, this effect should be included as part of the systematic uncertainties. This feature was checked for a large range of P_{T}^{match}. After including the full shower (ISR+FSR) and Multiple Interaction (MI) we have opted for a value of P_{T}^{match} of 10 GeV.

In figure 7.6 we show the P_{T} (left) and η (right) distributions of the top quark at the partonic level after the full shower and MI for $P_{\mathrm{T}} = 10$ GeV. The blue dashed line represents the real radiation part while the black line is the direct top fully showered but with the P_{T} starting scale at 10 GeV. The solid black line is the final NLO distribution which amounts to the sum of the previous two.

In figure 7.7 we present the LO and NLO P_{T} (left) and η (right) distributions of the top quark at the partonic level after the full shower and MI. It is clear from figure 7.7 that the P_{T} and η distributions of LO direct top production are quite different from the corresponding NLO direct top ones. In fact, the distributions show that the use of a constant K factor does not correctly describe the behaviour

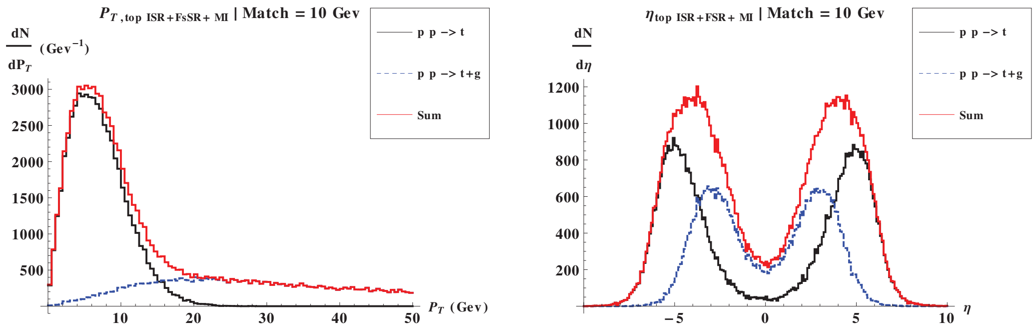

Figure 7.6: P_{T} (left) and η (right) distributions of the top quark at the partonic level after the full shower (ISR+FSR) and Multiple Interaction.

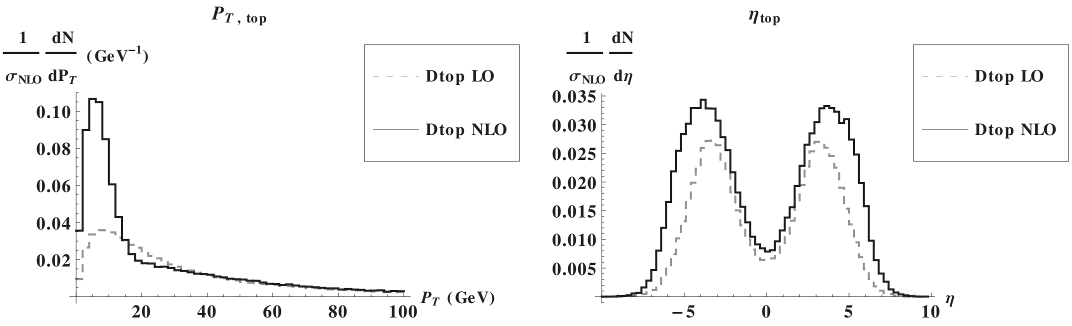

Figure 7.7: Comparison of the LO and NLO P_{T} (left) and η (right) distributions of the top quark at the partonic level after the full shower (ISR+FSR) and Multiple Interaction.

of direct top at NLO. Hence, a new analysis is needed to improve the accuracy of the bounds on the strong coupling constants κ_u and κ_c. The direct top NLO P_{T} distribution is shifted to low values of P_{T} as compared to the LO distribution while the $e\eta$ distributions are shifted to higher values of η as compared to the LO one. Obviously this applies only to the inclusive direct top analysis. In fact, analysis where a a high P_T jet is detected alongside the top-quark, like the one performed by the D0 collaboration (163), will not be modified significantly by using MEtop.

The actual experimental analysis is performed by looking at the distributions of the final state particles. Therefore, in figure 7.8 we present the comparison between LO and NLO P_{T} (left) and η (right) distributions of the lepton from $t \to bW \to bl\nu$ at the partonic level after the full shower and MI. Again, it is clear that the level of improvement by considering the NLO distributions heavily depends on the particular analysis being performed.

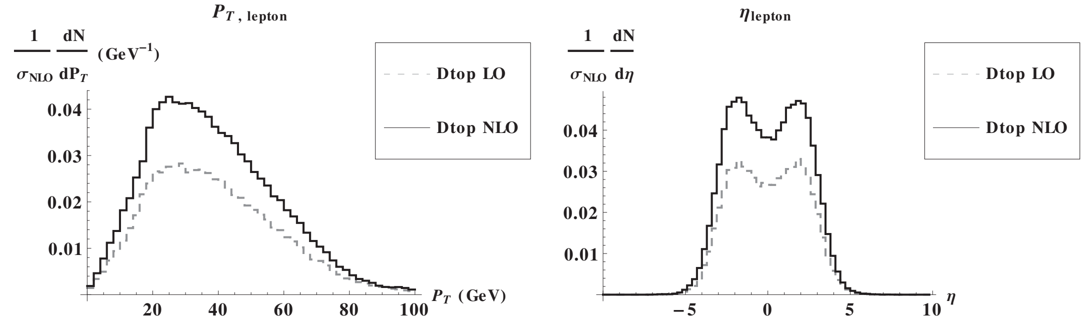

Figure 7.8: Comparison of the LO and NLO P_{T} (left) and η (right) distributions of the lepton from $t \to bW \to bl\nu$ at the partonic level after the full shower (ISR+FSR) and Multiple Interaction.

Finally, in figure 7.9 we compare the LO and NLO P_{T} (left) and η (right) distributions of the b-quark coming from $t \to bW \to bl\nu$ at the partonic level after the full shower and MI.

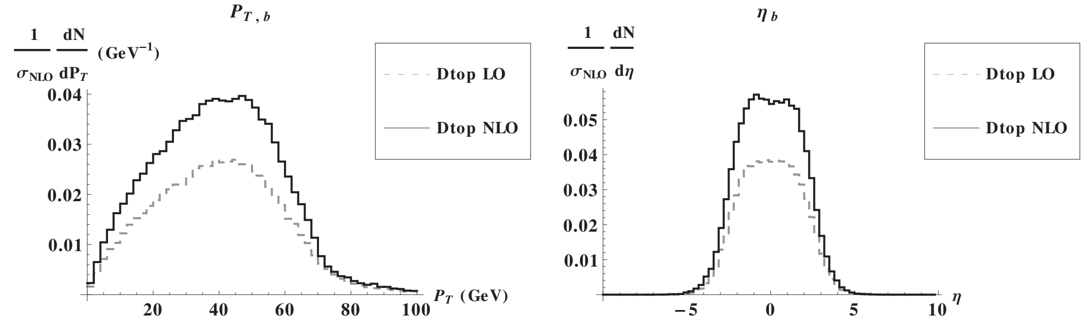

Figure 7.9: Comparison of the LO and NLO P_{T} (left) and η (right) distributions of the b-quark from $t \to bW \to bl\nu$ at the partonic level after the full shower (ISR+FSR) and Multiple Interaction.

We have just described how we generate a sample of inclusive direct top production at NLO. However, for the reasons we explained above, we need to add the parton level processes $gg \to t + q$ and $q_1 q_2 \to t + q$, where q, q_1, q_2 are quarks. Although the main contribution to top + jet production comes from the reaction where the jet is a gluon, all processes where the strong FCNC operator intervenes should be taken into account in the analysis. As these processes also suffer from infrared and collinear divergences, we have decided to avoid them by using a similar cut to that of P_{T}^{match}, that is, $P_{\mathrm{T}} > 10$ GeV. The complete NLO QCD corrections to the FCNC process of top+jet production were presented in (164). The corrections can increase the cross section by 10 % to 30 % at the LHC@14TeV.

Figure 7.10: $u\bar{b} \to t\bar{b}$ contribution to single top production, representing a SM type of diagram (left) and the corresponding strong FCNC diagram (right) that interferes with the SM one.

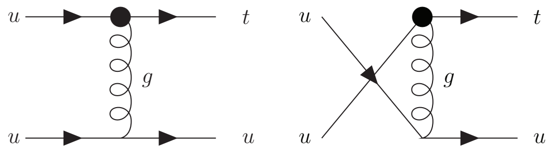

Figure 7.11: $uu \to tu$ contribution to single top production as an example of strong FCNC diagrams that do not interfere with the SM ones.

When generating the top + quark subprocesses we have to decide what is considered as signal in our analysis. $pp \to tq$ has three different classes of subprocesses: the ones which are exclusive to the Standard Model, like $u\bar{b} \to t\bar{b}$ (figure 7.10, left) , the ones that are originated exclusively via FCNC interactions, e.g. $uu \to tu$ (figure 7.11) , and the ones where interference between SM diagrams and pure FCNC diagrams occurs, like $u\bar{b} \to t\bar{b}$ (figure 7.10, right).

We define as FCNC signal the contributions from the two latter classes of subprocesses. For the pure FCNC processes this poses no problems. However, for the interference terms this procedure leads to the inclusion of a small portion of events that will also be counted as background. However, choosing the effective strong coupling constants as $\kappa_u = 0.01$ ($\Lambda = 1$ TeV) , $f_u = 1/\sqrt{2}$ and $h_u = 1/\sqrt{2}$ and for a CM energy of 7 TeV, the pure FCNC cross section is 8.718 pb, the interference term is 1.205 pb while the SM contribution amounts to only 0.018 pb. Hence, the SM contributions can be safely neglected. Note that the diagrams presented in this section are just examples of the three type of diagrams in single top FCNC production - all diagrams with a top quark in the final state are included in MEtop.

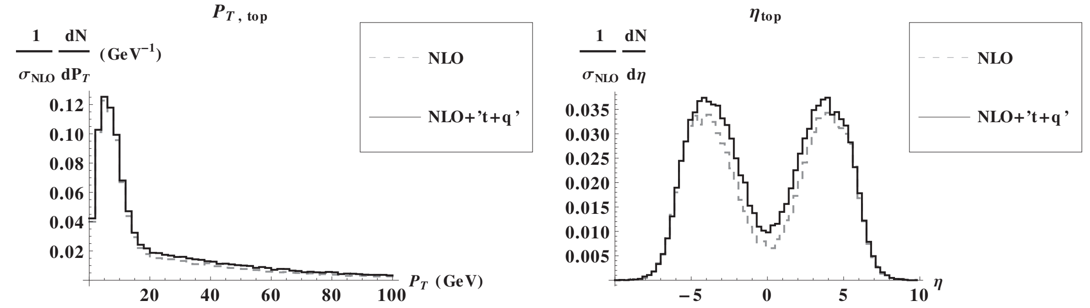

Figure 7.12: P_{T} (left) and η (right) distributions of the top quark for NLO direct top (solid line) and NLO direct top plus $pp \to tq$ with $P_{\mathrm{T}}^{match} = 10$ GeV and jet $P_{\mathrm{T}} > 10$ GeV.

In figure 7.12 we show the P_{T} and η distributions for the direct top at NLO summed with $pp \to tq$ for a $P_{\mathrm{T}}^{match} = 10$ GeV and the $P_{\mathrm{T}} > 10$ GeV. It is clear that the shape of the distributions do not change much with the inclusion of the $pp \to tq$ process but still the $pp \to tq$ process gives a contribution of the order of 10 % to the total cross section of the inclusive top production at the LHC at $\sqrt{s} = 7$ TeV.

7.5 Single top beyond the strong FCNC operators

In the previous sections we have discussed NLO direct top and $t + q$ production when only the strong FCNC operator is considered. We note that the leading order contribution to direct top does not receive contributions from other operators. Therefore, the NLO calculation is again performed with only the strong FCNC operator. As long as no excess is found at the LHC in the single top channel, the procedure described in the previous section gives us the best possible bound on the anomalous strong FCNC coupling when all other operators are discarded.

In the hard P_{T} region, the process $pp \to t + jet$ gets contributions from the complete set of independent operators. As these operators are independent from each other (and therefore so are the respective coupling constants) the interference terms between strong and electroweak or 4F could be sizeable. If an excess is found in the single top channel, one has to take into account all possible contributions from the remaining operators. A thorough analysis of the distributions of each individual operator will help us understand which operators could be important for a given experimental analysis. Moreover, even if an excess is not seen in the single top channel, dedicated analysis could most probably help constraining definite sets of operators.

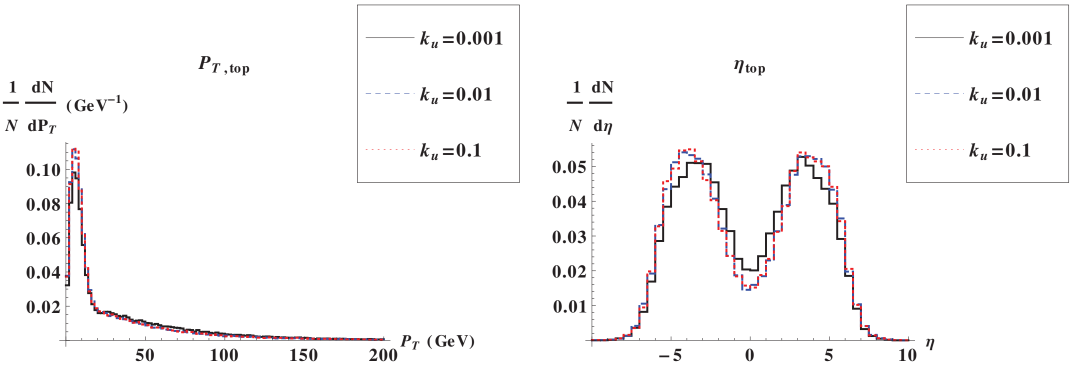

Figure 7.13: P_{T} (left) and η (right) distributions of the top quark when only the strong operator is turned on with $P_{\mathrm{T}}^{cut} = P_{\mathrm{T}}^{match} = 10$ GeV. Process considered is direct top at NLO plus $pp \to tq$ for $\sqrt{s} = 7$ TeV and three values of k_u with $\Lambda = 1$ TeV.

We start by considering the strong operator. When all other operators are turned off the P_{T} and η distributions have a very mild dependence on the strong coupling constant κ (κ_u to be more precise, and we have set $\kappa_c = 0$). This is shown in figure 7.13 where the P_{T} (left) and η (right) distributions of the top-quark are shown for three values of κ, 0.001, 0.01 and 0.1 and $\Lambda = 1$ TeV. The process is direct top NLO plus $pp \to tq$ for $\sqrt{s} = 7$ TeV and $P_{\mathrm{T}}^{cut} = P_{\mathrm{T}}^{match} = 10$ GeV. It is clear that the shape of the distributions does not vary much making it possible to perform the analysis for one constant and then to extract a bound on the strong operator.

We now move to the study of the electroweak operators. We first consider only

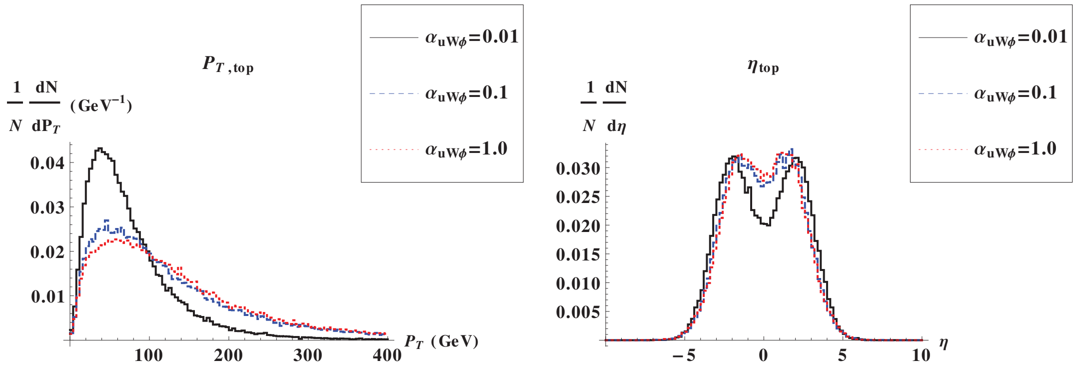

Figure 7.14: P_{T} (left) and η (right) distributions of the top quark when just one electroweak operator, $O_{uW\phi}$, is turned on. The process is $pp \to tq$ for $\sqrt{s} = 7$ TeV and $P_{\mathrm{T}}^{cut} = 10$ GeV.

one operator $O_{uW\phi}$ turned on. At the end of section 2 we showed that present bounds on the coupling constant for this operator are of the order 0.3 TeV^{-1}. In figure 7.14 we present the P_{T} (left) and η (right) distributions of the top-quark for three values of $\alpha_{uW\phi}$, 0.01 , 0.1 and 1 and $\Lambda = 1$ TeV. As $\alpha_{uW\phi} \to 0$ we recover the pure SM contribution of electroweak origin. The SM cross section for this process and for 7 TeV is $\sigma = 0.019$ pb while the total cross section for $\alpha_{uW\phi} =$ 0.01, 0.1 and 1 are $\sigma = 0.0020$ pb, 0.148 pb and 12.4 pb respectively. Therefore the different shapes of the P_{T} and η distributions are due to the interference with the SM contribution. When $\alpha_{uW\phi} = 1$, the total cross section is almost 100 times larger than its pure SM counterpart. Therefore, this value shows how the distribution behaves when the SM contribution is negligible.

This kind of behaviour can occur for any operator on the list, provided that the coupling constants are such that SM and FCNC cross sections are of the same order of magnitude. Any deviation relative to the SM showing up in the distributions could mean an interference with one or more operators. Understanding the different distribution requires dedicated studies with no assurance however that the responsible operators could be identified. One should emphasise that a thorough study of the P_{T} and η distributions of the top-quark could help identifying classes of FCNC operators. A similar discussion applies to the 4F operators case.

One should also note that $pp \to tq$ does not include direct top, because the strong operator is turned off. Contrary to strong operator scenario, in this case the distributions change with the value of the electroweak constant. Therefore, any bound based on the production process has to take into account that different coupling constants can lead to different distributions.

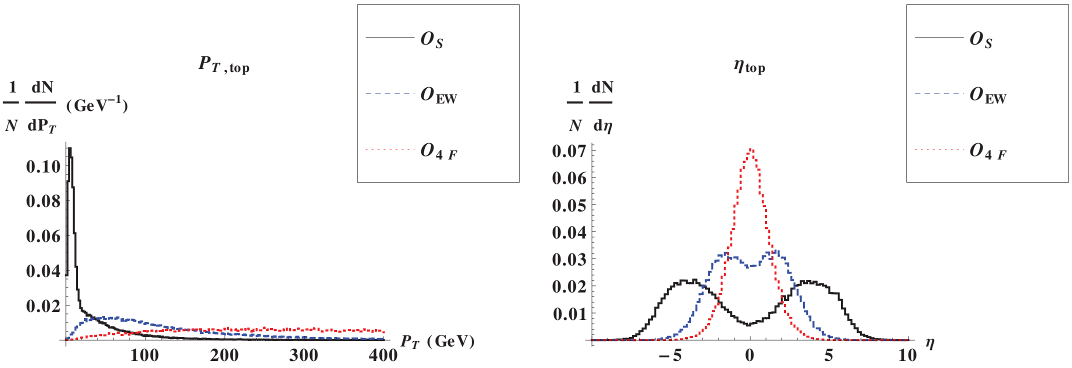

Figure 7.15: P_{T} (left) and η (right)distributions of the top quark when just one operator is taken non-zero at a time. We compare the distributions of the strong FCNC operator with one electroweak, $O_{uW\phi}$, and one 4F operator. The process is $pp \to tq$ for $\sqrt{s} = 7$ TeV and $P_{\mathrm{T}}^{cut} = 10$ GeV.

Having studied the distributions of a definite operator representative of each class, we will now perform a comparison between classes. In figure 7.15 we present the P_{T} (left) and η (right) distributions of the top-quark when just one operator is taken non-zero at a time. We compare the distributions of the strong FCNC operator with one electroweak operator (with coupling constant $\alpha_{uW\phi}$), and one 4F operator, $(\bar{u}\,\gamma_\mu\,\gamma_L\,u)\,(\bar{u}\,\gamma^\mu\,\gamma_L\,t)$. It is clear from the figure that the distributions can be quite different and therefore distinguishable to some extent. The ability to distinguish the different operators depends heavily on the relative values of the coupling constants. If an excess in single top production is seen we can try to understand its origin by looking at all possible distributions. However, this will always be a hard task because different operators give similar distributions and therefore only very particular scenarios can be probed.

7.6 Conclusions

We have presented a new generator for the study of FCNC top interactions. The generator MEtop comes with different packages, each with a subset of a complete set of dimension six operators. At the moment MEtop can generate events for direct top and for top plus jet production, where the jet can be any quark other than the top or it can be a gluon.

The direct top production process is implemented at NLO using an effective NLO approximation. Also, the inclusive contribution to direct top coming from $pp \to tq$ can be included in the event generation. We have shown that the top P_T and η distributions show clear differences when the events are generated at LO or at NLO. Therefore, the use of a constant K-factor does not provide an accurate description of direct top production at NLO. We conclude that a new experimental analysis is needed in order to improve the constraints on the strong FCNC coupling constants. The inclusion of the inclusive process $pp \to tq$ will further improve this bound. We note that a detailed study of the P_T and η distributions of the top-quark could help identifying classes of FCNC operators .

At LO, the contributions stemming from the different operators can be compared in the single top production process. In particular, 4F operators can be for the first time constrained at hadron colliders. Constraining the 4F operators can help us understand their role in the asymmetry measured at the Tevatron.

The bounds on $BR(t \to u(c)Z)$ and $BR(t \to u(c)\gamma)$ are obtained in the process $pp \to t\bar{t}$ where one of the top-quarks decays as $t \to bW$ while the other decays as $t \to u(c)Z$ or $t \to u(c)\gamma$. This means that all electroweak FCNC couplings always appear in the same combination. With MEtop we are able to look for distribution that isolate each electroweak FCNC operator. This way more detailed information can be obtained about each operator.

New final states with FCNC contributions, like for instance $pp \to tW$ (165), are to be included in the next version of MEtop.

8

Experimental Simulation

This chapter summarises the work published in the reference:
Phys. Rev. **D**88, 114011 (2013).

8.1 Introduction

The purpose of this chapter is threefold. First we want to compare the previous analysis where the events were generated at LO and normalized with a K-factor with one where the direct top events are generated at NLO using MEtop described in the previous chapter. We will therefore redo the analysis performed by the ATLAS collaboration in (14) with the NLO events generated by MEtop. Second, because MEtop also includes the LO hard FCNC process $pp \to tj$, where j is a light jet, we will account for the contribution of the hard process to the analysis already performed. Our goal is to check weather a sizeable improvement in the limit is obtained just by adding the events from the FCNC single top process to the direct top events. Finally, we will perform an analysis where again we follow (14) but allow for one extra hard jet in the signal. It is clear that the final state will then be very similar to the SM single top one. Hence, our objective is to check if the major increase in the background can be compensated by the increment in the number of signal events.

8.2 Data Sample

Three different sets of signal events were generated with METop,

- FCNC direct top @LO: $Dtop^{LO}$,
- FCNC direct top @NLO: $Dtop^{NLO}$,
- FCNC direct top @NLO plus FCNC single top @LO: $Dtop^{NLO} + (t+j)^{LO}$.

The last set ($Dtop^{NLO} + (t+j)^{LO}$) is a weighed combination of direct top production at NLO with FCNC single top production at LO. As discussed in chapter 4, only one FCNC operator for each light quark (u and c) contributes to the direct top process. Therefore, each set is composed of two samples - one where only the ugt coupling is turned on and the other where only the cgt coupling is turned on. The generation of the FCNC single top quark events in $Dtop^{NLO} + (t+j)^{LO}$ followed the same rule. All events were generated assuming a SM top quark decay, *i.e.*, $BR(t \to W^+ b) \approx 100$ % and only the leptonic decay of the W was considered. Additionally, the full τ leptonic decay was taken into consideration in both signal and background. We have used the Parton Density Function (PDF) set CTEQ6 for all LO processes and CTEQ6.6 for the NLO cross sections.

As previously stated the SM FCNC cross section is negligible due to its very low rate. The most significant backgrounds are single top production, $t\bar{t}$ production, W/Z plus jets (both light and heavy jets), diboson production and the multijet background. The single top background (t-channel, s-channel and Wt associated production) together with $t\bar{t}$ were generated with POWHEG (166) at NLO and the CTEQ6.6 NLO PDFs were used. For W plus light jets, Wc plus light jets, $Wb\bar{b}$, $Wc\bar{c}$ (plus light jets) and Z plus light jets we have used AlpGEN (167) with the CTEQ6 LO PDFs. In all events generated with AlpGEN the jets have a transverse momentum above 20 GeV and $\Delta R_{jj} > 0.7$. Further, in the W plus jets case, the jets have $|\eta_j| < 4.9$ and for Z plus jets $|\eta_j| < 2.5$. For both the W and the Z plus jets events, the number of jets was varied from 0 to 3. To remove overlaps between n and $n+1$ partons the MLM matching scheme (168) was used. The cross sections were then normalized at NLO using MCFM (76, 77).

The events were then submitted to a parton shower simulator performed with PYTHIA 6 in order to include initial (ISR) and final (FSR) state radiation, as well as multiple interactions. The Perugia tune (169) was used to handle the underlying events in POWEG while the ATLAS MC09 tune (170) was used for events generated with AlpGen. Finally, both signal and background detector simulation was performed with Delphes (171), which is a framework for the fast simulation of a generic detector in a collider experiment. For the detector and trigger configurations, we resorted to the ATLAS default definitions in Delphes. However, in order to reproduce the ATLAS analysis as faithful as possible we have redefined the sum of the E_T in a cell to be calculated within a cone of $\Delta R = 0.3$ for the lepton, and $\Delta R = 0.4$ for the jet. Additionally, the b-tagging efficiency was set to be 57%, and the b-mistagging to 0.2% for light-quark jets and 10% for c-quark jets. These values were chosen to match the ATLAS analysis (14). Finally, we have not considered the diboson and multijets background which in the ATLAS analysis (14) amounts to 9 % of the total background (the largest contribution comes from multijets with about 6.7 %).

8.3 Event selection

As previously discussed we have performed two different analyses. The first one is similar to one presented in (14) by the ATLAS collaboration. It should be noted however that besides the usual cut-based analysis, ATLAS uses a multivariate analysis technique (neural-network) to separate signal from background. As we will not be using this multivariate technique, our results cannot be compared with theirs. This is not an issue because our aim is not to compare our analysis with the experimental one but rather to study its performance for different sets of events generated with MEtop. The ATLAS analysis will be used as our standard analysis because it provides the best current limits on the *ugt* and *cgt* strong FCNC couplings. It will also serve as a means to control our background. In the present work the limits on the FCNC couplings were obtained using the ATLAS cut-based part of the analysis plus an additional cut on the top invariant mass. From now on, we shall call this analysis "ATLAS" but it should be clear that this is not the ATLAS analysis performed in (14). A detailed description of what we call the "ATLAS" analysis will be presented below. Still in the framework of this first analysis we will consider a new set of signal events, $Dtop^{NLO} + (t + j)^{LO}$, that is, we will add the FCNC single top to the NLO direct top. The ATLAS final state consists of one b-quark jet, one lepton (electron or muon) and missing energy. In the analysis, we ask for exactly zero non-b jets. However, a jet can only be identified with $p_T > 25$ GeV and $|\eta_j| < 2.5$. This means that some of the events from FCNC single top will still pass the selection if the non b-jet is soft. Hence, we will study how the inclusion of the FCNC single top events will affect the bound on the couplings.

The second analysis will be performed considering a different final state topology with an extra hard non-b jet. In table 8.1 we present the total cross section for each of the three set of events, where the FCNC coupling constants were set to either zero or $\kappa_{qgt}/\Lambda = 0.01$ TeV^{-1}, where κ_{qgt} is defined in equation (4.12). The $t + j$ sample and the corresponding total cross section is produced with a 10 GeV cut on the jet p_T. For the chosen value of the coupling constant, the FCNC single top cross section gives an additional contribution of 14% and 27% to the full NLO direct top cross section, for the ugt and cgt operators respectively. These extra events are kinematically similar to the SM single top ones and are therefore expected to be mainly located in regions discarded by the ATLAS analysis. Nevertheless, it is important to understand if an analysis that considers an extra hard jet can lead to an improvement on the FCNC couplings limit. We will refer to this analysis as ATLAS(m).

	$\sigma(Dtop^{LO})$ (pb)	$\sigma(Dtop^{NLO})$ (pb)	$\sigma(Dtop^{NLO} + (t + j)^{LO})$ (pb)
ugt	2.245	2.972	3.374
cgt	0.355	0.567	0.720

Table 8.1: $Dtop^{LO}$, $Dtop^{NLO}$ and $Dtop^{NLO} + (t + j)^{LO}$ total cross sections for $\sqrt{s} = 8$ TeV, $\kappa_{qgt}/\Lambda = 0.01$ TeV^{-1} and leptonic channel.

We have used the ATLAS default trigger card on the Delphes detector with an isolated electron with $p_T > 25$ GeV or an isolated muon with $p_T > 20$ GeV In the analysis we demanded at least one electron or one muon with $p_T > 25\,GeV$.

	ATLAS		ATLAS(m)	
Process	Events ($1fb^{-1}$)	Efficiency (%)	Events ($1fb^{-1}$)	Efficiency (%)
Single top	330.8	0.286	1198.5	1.035
$t\bar{t}$	111.0	0.052	773.1	0.365
W + light jets	2900.1	0.026	4300.3	0.039
Wc + light jets	1796.2	0.317	2384.4	0.421
$Wb\bar{b}/Wc\bar{c}$ + light jets	45.9	0.591	128.7	1.656
Z + jets	66.4	0.002	116.2	0.004
Total background	5250.4		8901.2	

Table 8.2: Number of events and efficiency for the background processes in the ATLAS and in the ATLAS(m) analyses.

Exactly one reconstructed jet with $p_T > 25$ GeV is required. This jet has to be identified as a b-quark jet (b-tagged). We excluded events with missing transverse energy $\not{E}_T < 25$ GeV In order to further reduce the multijet background - most of it with low $\not{E}_T$ and low values of the reconstructed W-boson transverse mass $M_T^W = \sqrt{2p_T^l\not{E}_T - 2(p_x^l\not{E}_x + p_y^l\not{E}_y)}$ - we have required $M_T^W + \not{E}_T > 60$ GeV Finally, the top-quark invariant mass is set to be above 140 GeV. This last cut was not implemented by ATLAS in their cut-based part of the analysis (14) but it is included in the multivariate part.

In the ATLAS(m) analysis we have changed the requirements regarding jets: we have asked for one or two reconstructed jets with $p_T > 25$ GeV, where one jet must be a b-jet and the second is forced to be a non-b jet. In the left panel of fig. 8.1 we show the jet multiplicity for jets with $p_T > 25$ GeV. In the right panel we show the top quark invariant mass before the respective cut is implemented which allow us to understand the effect of this additional cut in the analysis.

In table 8.2 we list all backgrounds considered in the analysis as well as the event yield and the efficiency for a luminosity of $1\,fb^{-1}$. These are the final events gathered after all cuts. As expected there is a significant increase in the single top and $t\bar{t}$ backgrounds because there is an extra non-b jet in the ATLAS(m) analysis. However, the overall increase in the total background in ATLAS(m) relative to ATLAS is not as large because the major contributions to the total background comes from W+jets where the increment is not so dramatic.

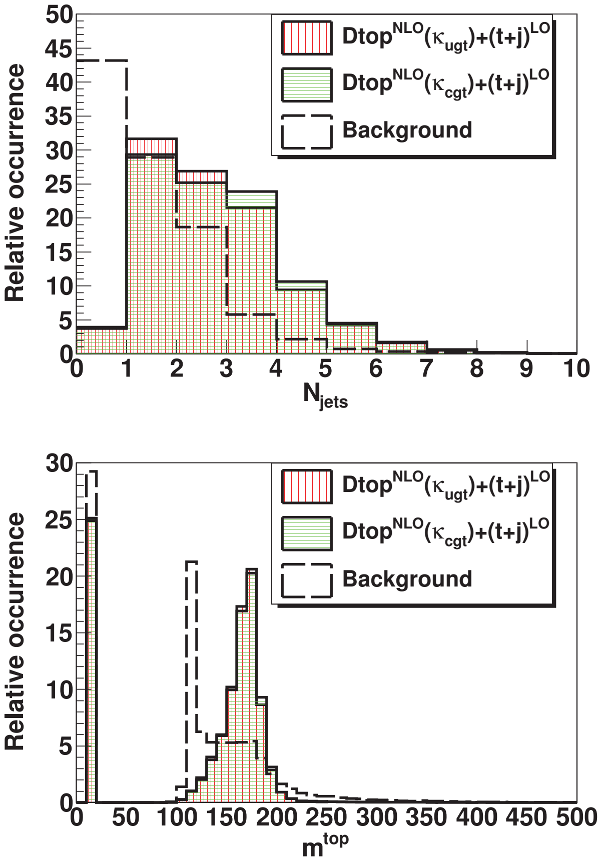

Figure 8.1: In the left panel we present the jet multiplicity for jets with $p_T > 25$ GeV. On the right we show the top-quark invariant mass.

	ATLAS	ATLAS(m)
Process	Efficiency (%)	Efficiency (%)
$Dtop^{LO}(\kappa_{ugt})$	2.509	–
$Dtop^{LO}(\kappa_{cgt})$	3.428	–
$Dtop^{NLO}(\kappa_{ugt})$	2.591	–
$Dtop^{NLO}(\kappa_{cgt})$	3.581	–
$Dtop^{NLO}(\kappa_{ugt}) + (t+j)^{LO}$	2.413	3.283
$Dtop^{NLO}(\kappa_{cgt}) + (t+j)^{LO}$	3.072	4.142

Table 8.3: Efficiencies for the signal processes.

In table 8.3 we list the efficiencies for the signal processes after all cuts. There is no significant difference between the LO and NLO samples in the ATLAS analysis. The only notable difference arises in the ATLAS(m) analysis for the $Dtop^{NLO} + (t+j)^{LO}$ sample. As expected the efficiency is better in ATLAS(m) than in ATLAS which is in accordance with the design of ATLAS(m). We now have to check if the rise in the number of signal events is enough to compensate for the increase in the total background.

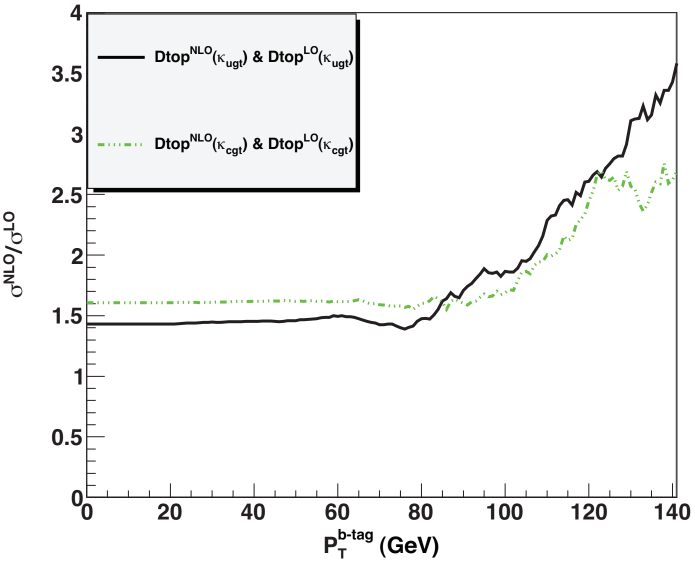

Figure 8.2: K-factor as function of the transverse momentum cut on the b-tagged jet.

As the LO and NLO results are quite similar, the NLO result seems to be well described by the LO sample with a constant K-factor. In figure 8.2 we plot the K-factor as a function of the transverse momentum cut of the b-tagged jet. In this plot we have performed all cuts except the one on the b-jet in the ATLAS analysis. Then we have calculated the ratio between the number of events coming from the NLO sample and the same number with the LO sample for different values of the p_T cut on the b-tagged jet. It is clear that the use of a constant K-factor is justified up to approximately a $p_T = 60$ GeV cut. For large p_T the recipe fails. However, the number of events decreases steeply with the b-jet p_T cut for large p_T values and therefore their contribution to the total number of events becomes negligible. We have checked several other distributions always reaching the same conclusion - the regions where the use of a constant K-factor would not be allowed, contribute with a small number of events to the analysis. Obviously, one should note that this is true for this particular analysis and not a general rule.

8.4 Limits

In this section we will present the bounds on the anomalous couplings for four different scenarios: ATLAS analysis with the three samples $Dtop^{LO}$, $Dtop^{NLO}$ and $Dtop^{NLO} + (t+j)^{LO}$ and ATLAS(m) with $Dtop^{NLO} + (t+j)^{LO}$. In fact, because the ATLAS analysis with the $Dtop^{LO}$ and $Dtop^{NLO}$ leads to very similar results we will only show the results for the NLO sample. Further, the ATLAS(m) analysis with only direct top events has negligible signal events yields.

As previously stated, the best current exclusion limit (assuming only one non-zero coupling at a time) was obtained in (14) by ATLAS. With an energy of $\sqrt{s} = 7$ TeV and a total integrated luminosity of $2.05 \pm 0.08\ fb^{-1}$ the obtained limits at 95% C.L. were

$$\kappa_{ugt}/\Lambda < 4.8 \times 10^{-3}\ \text{TeV}^{-1} \quad \kappa_{cgt}/\Lambda < 11.3 \times 10^{-3}\ \text{TeV}^{-1}\ . \tag{8.1}$$

As discussed, our goal is not to compete with this analysis but rather to understand if there is a way to improve it. According to our analysis there would be two possibilities to improve the bounds on the couplings. The first one would be to just include the FCNC single top events in the signal, that is, to use the sample $Dtop^{NLO} + (t+j)^{LO}$. The second would be to change the analysis by including an extra hard non-b jet (ATLAS(m)). In order to obtain the 95% CL limits for κ_{ugt}/Λ and κ_{cgt}/Λ, we have used the code described in (172).

In fig. 8.3 we present the results for $\sqrt{s} = 8$ TeV and a total integrated luminosity of 20 fb^{-1}. In the left panel we show the 95% C.L. upper limit on the coupling constant κ_{ugt}/Λ and κ_{cgt}/Λ according to the ATLAS analysis for the

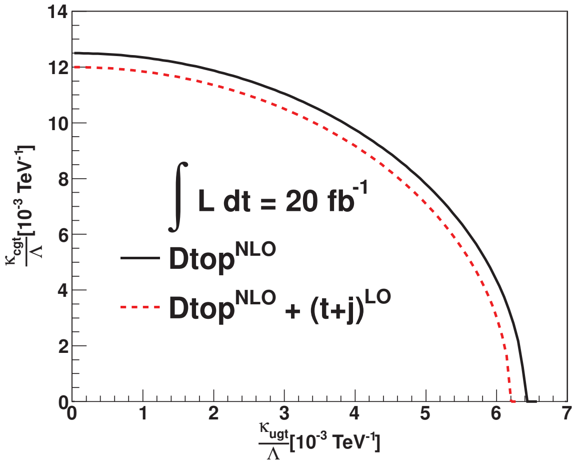

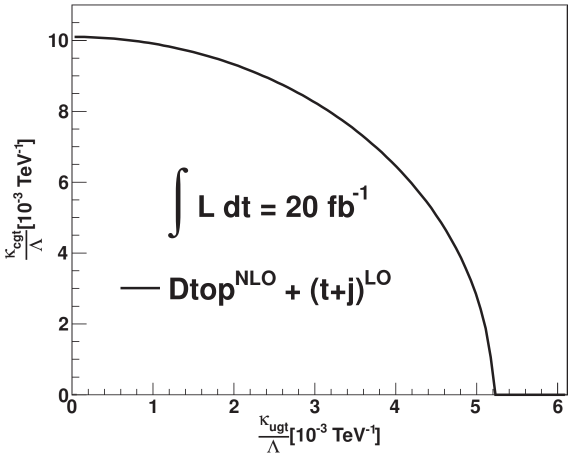

Figure 8.3: Up -Upper limit on the coupling constant κ_{ugt}/Λ and κ_{cgt}/Λ according the ATLAS analysis. Bottom - Upper limit on the coupling constant κ_{ugt}/Λ and κ_{cgt}/Λ according the ATLAS(m) analysis.

$Dtop^{NLO}$ sample (black line) and for the $Dtop^{NLO} + (t+j)^{LO}$ sample (slashed red line). The LO result with the K-factor is almost on top of the the NLO one and therefore it is not shown in the figure. Hence, for this particular analysis, no significant difference is seen when using the NLO generator. In the botton panel we show the ATLAS(m) analysis with the $Dtop^{NLO} + (t+j)^{LO}$ sample. The numeric results for the limits with each coupling taken non-zero at a time are shown in table 8.4 (they correspond to the intersection of the exclusion curve with the x and y axes).

	ATLAS	ATLAS(m)
Process	$\kappa/\Lambda\,[10^{-3}]\,TeV^{-1}$	$\kappa/\Lambda\,[10^{-3}]\,TeV$
$Dtop^{NLO}(\kappa_{ugt})$	6.4	–
$Dtop^{NLO}(\kappa_{cgt})$	12.5	–
$Dtop^{NLO}(\kappa_{ugt}) + (t+j)^{LO}$	6.2	5.2
$Dtop^{NLO}(\kappa_{cgt}) + (t+j)^{LO}$	12.0	10.1

Table 8.4: Limits of the κ_{qgt}/Λ.

The results presented in fig. 8.3 and in table 8.4 allow us to conclude that a slight improvement in the bound can be achieved by including the full set of events $Dtop^{NLO} + (t+j)^{LO}$ in the ATLAS analysis. The same is true for the ATLAS(m) analysis when compared with ATLAS, even when the $Dtop^{NLO} + (t+j)^{LO}$ is considered. However, we should look at this results as an indication that a full detector analysis is worth doing. First because the improvement is only of the order a few % and second because since we did not consider the multi-jet background, we could be overestimating the sensitivity in ATLAS(m).

8.5 Conclusions

We have studied top production at the LHC via FCNC interactions. We have performed two different analyses using the MEtop generator which allows for the production of NLO direct top events and LO FCNC $pp \to tj$ events. In the first one we have followed ATLAS in (14) but using two different samples, one with only direct top NLO events and the other one with direct top NLO plus the LO $t+j$ FCNC events. In the second analysis we allow for an extra hard non-b jet in the final state increasing both the signal and the background yields.

We have concluded that the inclusion of the FCNC single top events has increased the sensitivity. Even if the limit is better by only a few percent this should be implemented in the experimental analysis because this is a real contribution to the process and should not be neglected. Furthermore, its inclusion is straightforward with MEtop. In the second analysis the limit on the couplings is significantly better. In this case however we should look at the result as an indication that an experimental analysis is worth performing.

Before the present thesis has been concluded new top FCNC coupling limits were measured by ATLAS (173), where FCNC Direct top @ NLO events generated by MEtop were used. They present now the best current limits on top FCNC physics.

We show in figure 8.4 the measured coupling constant upper limits κ_{ugt}/Λ and κ_{cgt}/Λ, which can be compared with the our fast simulation analysis results shown in 8.3. By comparison we can concluded that although we have performed a fast simulation, close upper limits values were obtained.

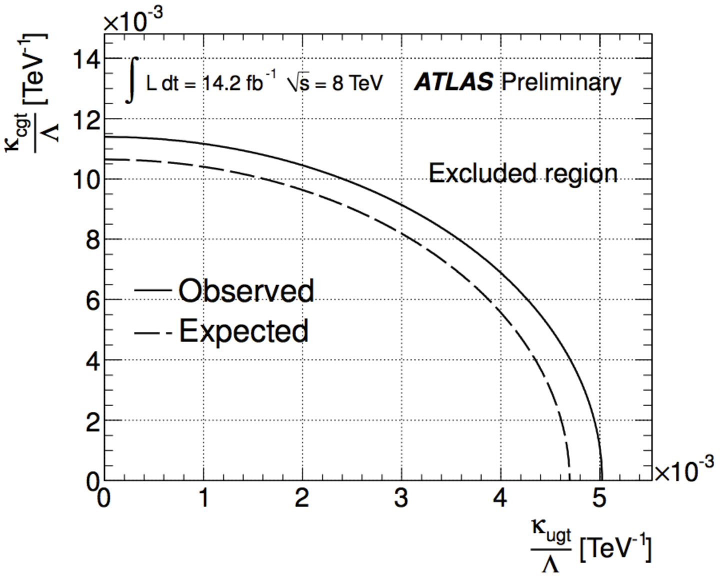

Figure 8.4: Upper limit on the coupling constant κ_{ugt}/Λ and κ_{cgt}/Λ according the new ATLAS analysis . From (173).

9

Conclusions

A number of new results in top FCNC physics have been presented in this work. We began with a presentation on the subject of collider physics where we gave the reader the necessary basic tools for understanding the key issues behind the many technicalities one must consider before studying a collision process at a high energy collider. The main focus was on the use of Monte Carlo generators, on the theory of hadronic collisions and parton shower simulation. A brief description of the MCMC method was also introduced.

The main purpose of the LHC is to test the SM of strong and electroweak interactions. After presenting the SM, a detailed account of the effective lagrangian formalism was given. We have used a dimension six Lagrangian to parametrize physics beyond the SM. As explained, this Lagrangian has the SM as its low energy limit and a particular subset was built for the study of top physics related to flavour changing neutral currents. Different subsets were used according to the study being performed as was shown later: the subset used in FCNC top pair production is not the same as the one used in direct top production. Similar differences occur if a process is studied at a hadron or at a lepton collider.

In chapter 5 we showed a study of FCNC single top production at a future electron-positron collision. The main question we wanted to address was what could a lepton colider tell us after the LHC was shut down. The main conclusion was that in some of the proposed scenarios for the ILC (for example a centre-of-mass energy of $\sqrt{s} = 500$ GeV and 500 fb^{-1} of luminosity) no significant improvements on the bounds and branching ratios is expected for the electroweak operators. On the contrary, an improvement is expected for the four-fermion operators due to significant increase of the total cross section that grows with the collider's energy. In case of a $\gamma\gamma$ collider we have concluded that a good improvement on the $Br(t \to q\gamma)$ bound can be obtained, using a single effective operator.

We have then moved to chapter 6 where an attempt was made to understand the discrepancy between the experimentally measured values and the SM predictions for the forward-backward asymmetry in top pair production using the effective operator formalism. We have investigated the possibility that new physics described by top FCNC effective operators could account for the measured asymmetry at the Tevatron. Therefore a minimal set of dimension six FCNC operators (including four-fermion operators) was tested. The search was made through a fit of 14 physical observables using Markov Chain Monte Carlo approach. The final result showed that it is very unlikely that the asymmetry can be described by either electroweak or strong FCNC effective operators. A tension between the measured value of the total cross section, which agrees with the SM prediction, and the asymmetries, revealed to be one the main issues preventing that a good fit to all observables could be obtained. Regarding four-fermion operators a good fit to all observable was obtained. Since there are no strong constraints on the 4F operators, they could in fact explain the discrepancy observed at the Tevatron.

Most of the time devoted to this thesis was used in building a new Monte Carlo generator for top FCNC studies. The MEtop generator was presented in chapter 7 where its main features were highlighted. It is the first generator where NLO direct top events can be produced. We have shown that in the NLO events, the top quark kinematical distributions presented a significant differences form the LO ones. Therefore a simple K-factor recipe applied to the LO distributions does not work in general. The generator also allows for the generation of single top FCNC events at LO. Hence, an inclusive analysis of FCNC direct top plus one jet can also be performed. Several sets of dimension six operators were made available allowing for the study of different Lorentz structures. The generator is now being used by the ATLAS collaboration, in particular by the very recent analysis results presented in (173).

In chapter 8 two detector level analyses were performed in order to test MEtop performance. In the first one we have followed ATLAS in [3] but using two diferent samples, one with only direct top NLO events and the other one with direct top NLO plus the LO t + j FCNC events. In the second analysis we allow for an extra hard non-*b* jet in the final state increasing both the signal and the background yields. We have concluded that the inclusion of the FCNC single top events has increased the sensitivity. Even if the limit is better by only a few percent this should be implemented in the experimental analysis because this is a real contribution to the process and should not be neglected. Furthermore, its inclusion is straightforward with MEtop. In the second analysis the limit on the couplings is significantly better. In this case however we should look at the result as an indication that an experimental analysis is worth performing.

CERN's hadron collider will soon resume its operation with the center-of-mass energy increased to 13 or 14 TeV. The search for FCNC in top physics has therefore just began. The SM values for the branching ratios of top rare decays will not be achieved even at very high luminosity. However, even if no signal of top FCNC is found, stringent limits will be put on the coupling constants of the effective operators and therefore restrict the class of models that have the SM as its low energy limit.

Appendix A

Available Model files

At the moment there are three different packages available in MEtop, with a different set of effective operators. The main reason to have the different packages is to make the generation of events faster. The lightest version includes only the strong sector. Then there are two other versions one with strong plus electroweak operators and the other one with strong plus 4F operators. The set of operators follows from the calculations shown in chaper 4.

In equation A.1 we present the strong FCNC lagrangian as it is written in the package "MEtop_S_vxx.tar.gz"

$$\mathcal{L}_S \quad = \quad co1\, \mathcal{O}_{uG} + co2\, \mathcal{O}_{cG} + h.c. \tag{A.1}$$

with

$$\mathcal{O}_{uG} = i\frac{g_s}{\Lambda}\bar{u}\lambda^a\sigma^{\mu\nu}(fu + hu\ \gamma_5)tG^a_{\mu\nu} \quad , \quad \mathcal{O}_{cG} = i\frac{g_s}{\Lambda}\bar{c}\lambda^a\sigma^{\mu\nu}(fc + hc\ \gamma_5)tG^a_{\mu\nu} \tag{A.2}$$

and $co1$, $co2$, fu, hu, fc, hc are real constants to be chosen in the file param.dat. The constants f_i, h_i allow the choice of different chiralities while co_i are overall normalization constants. Although it usually considered that $f_i^2 + h_i^2 = 1$, this relation has to be implemented by the user by a judicious choice of parameters f_i and h_i.

The package "MEtop_SEW_vxx.tar.gz" contains the strong and electroweak sectors. The lagrangian introduced in this package is

$$\begin{aligned}\mathcal{L}_{SEW} &= \mathcal{L}_S + \frac{1}{\Lambda^2} \sum_{\substack{i,j=1,3\\ i\neq j}} \Big(\alpha^{ij}_{uW} \mathcal{O}^{ij}_{uW} + \alpha^{ij}_{uB\phi}\, \mathcal{O}^{ij}_{uB\phi} + \alpha^{ij}_{\phi u}\, \mathcal{O}^{ij}_{\phi u} + \alpha^{(3,ij)}_{\phi q}\, \mathcal{O}^{(3,ij)}_{\phi q} \\ &\qquad + \alpha^{(1,ij)}_{\phi q}\, \mathcal{O}^{(1,ij)}_{\phi q} + \alpha_{u\phi}\, \mathcal{O}^{ij}_{u\phi} \Big) \qquad (A.3)\end{aligned}$$

where the electroweak operators are

$$\begin{aligned} \mathcal{O}^{ij}_{u\phi} &= (\phi^\dagger \phi)\,(\bar{q}_{Li}\, u_{Rj}\, \tilde{\phi}) \qquad , \qquad \mathcal{O}^{(1,ij)}_{\phi q} = i\,(\phi^\dagger\, D_\mu\, \phi)\,(\bar{q}_{Li}\, \gamma^\mu\, q_{Lj}) \\ \mathcal{O}^{(3,ij)}_{\phi q} &= i\,(\phi^\dagger\, D_\mu\, \tau^I\, \phi)\,(\bar{q}_{Li}\, \gamma^\mu\, \tau^I\, q_{Lj}) \quad , \quad \mathcal{O}^{ij}_{\phi u} = i\,(\phi^\dagger\, D_\mu\, \phi)\,(\bar{u}_{Ri}\, \gamma^\mu\, u_{Rj}) \\ \mathcal{O}^{ij}_{uW} &= (\bar{q}_{Li}\, \sigma_{\mu\nu}\, \tau_I\, u_{Rj})\, \tilde{\phi}\, W^I_{\mu\nu} \qquad , \qquad \mathcal{O}^{ij}_{uB\phi} = (\bar{q}_{Li}\, \sigma_{\mu\nu}\, u_{Rj})\, \tilde{\phi}\, B_{\mu\nu} \end{aligned}$$

and all coupling constants are real. In param.dat all coupling constant have the form co_i. The relation between the coupling constants presented in equation A.3 and the co_i parameters to be chosen in param.dat is presented in table A.1.

$co3 \rightarrow \alpha^{ut}_{uW}$	$co4 \rightarrow \alpha^{tu}_{uW}$	$co5 \rightarrow \alpha^{ut}_{uB\phi}$	$co6 \rightarrow \alpha^{tu}_{uB\phi}$
$co7 \rightarrow \alpha^{ut}_{\phi u}$	$co8 \rightarrow \alpha^{tu}_{\phi u}$	$co9 \rightarrow \alpha^{(3,ut)}_{\phi q}$	$co10 \rightarrow \alpha^{(3,tu)}_{\phi q}$
$co11 \rightarrow \alpha^{(1,ut)}_{\phi q}$	$co12 \rightarrow \alpha^{(1,tu)}_{\phi q}$	$co13 \rightarrow \alpha^{ut}_{u\phi}$	$co14 \rightarrow \alpha^{tu}_{u\phi}$

Table A.1: Coefficient dictionary for $\mathcal{L}_{SEW}$.

Finally, the file "MEtop_S4F_vxx.tar.gz" contains the strong and 4F sector

$$\mathcal{L}_{S4F} = \mathcal{L}_S + \mathcal{L}_{4fu} + \mathcal{L}_{4fc} \qquad (A.4)$$

where the 4F lagrangians were presented in equations 4.38 and 4.39. The relation between the parameters these equations and the corresponding co_i parameters in the param.dat file is shown in table A.2:

Finally we note that any combination of parameters can be made in a new package and can be made available upon request. Generator and the different packages can be downloaded at **http://coimbra.lip.pt/∼miguelwon/MEtop/**.

$co27 \to \alpha_{qq}^{1113} + \alpha_{qq'}^{1113}$	$co33 \to \alpha_{qq}^{1123} + \alpha_{qq'}^{2113}$	$co39 \to \alpha_{uu}^{1123}$
$co28 \to \alpha_{qu'}^{1311}$	$co34 \to \alpha_{qq}^{2113} + \alpha_{qq'}^{1123}$	$co40 \to \alpha_{uu}^{2113}$
$co29 \to \alpha_{qu'}^{1113}$	$co35 \to \alpha_{qu'}^{1321}$	$co41 \to \alpha_{qu'}^{2311}$
$co30 \to \alpha_{uu}^{1113}$	$co36 \to \alpha_{qu}^{1321}$	$co42 \to \alpha_{qu'}^{1123}$
$co31 \to \alpha_{qu}^{1311}$	$co37 \to \alpha_{qu'}^{2113}$	$co43 \to \alpha_{qu}^{2311}$
$co32 \to \alpha_{qu}^{1113}$	$co38 \to \alpha_{qu}^{2113}$	$co44 \to \alpha_{qu}^{1123}$

Table A.2: Coefficient dictionary for $\mathcal{L}_{S4F}$.

Appendix B

MEtop User Manual

B.1 Installation

MEtop is written in C and python and it generates events following the .LHE format. It can therefore be easily interfaced with PYTHIA or Herwig. In order to compile it, you need a C compiler [1] and python version 2.6 or later. To run the package you must additionally install

- Cuba Library version 3.0
- LHAPDF version 5.8.6
- Numpy version 1.3.0

The Cuba and LHAPDF library must be available through the library environment variable (for example).

To install MEtop you just have to execute ”make” in the main directory.

---

[1] There is one file written in Fortran and therefore you also need a Fortran compiler.

B.2 The generator

B.2.1 param.dat

In MEtop all parameters are set in one file: ”param.dat”. Table B.1 summarizes the definition of each parameter.

Mx	Particle's masses (x=u,d,c,s,b,t,e,μ,τ,W,Z,H)
wx	Particle's Widths (x=W,t,Z,H)
sx	Values for CKM matrix elements (x=12,23,13)
SW	$\sin\theta_W$ (θ_W is the Weinberg angle)
EE	Electromagnetic coupling constant
cox	couplings of the x operator (x=1,2,...,9)
fx,hx	Chirality parameters from operators co1 and co2
Q	Factorization scale
miuR	Renormalization scale for Direct top at NLO
L	Energy scale
ECM	Centre of mass Energy
PTmatch	P_T for matching
PTmin	Cut in P_T for LO $2 \to 2$ processes
NEvnts	Number of events to generate
pdf	PDF name according to LHAPDF
pp	Type of collider: 1 for pp and -1 for $p\bar{p}$
DecMod	Turn on/off W decay modes
SpCorr	Turn on/off Spin Correlations
ttbar	t, $\bar{t}$ channel. 0-t only;1-$\bar{t}$ only;2-t and $\bar{t}$
seed	Turn random number seed

Table B.1: Summary description of ”param.dat” file.

B.2.2 Physical processes

In addition to the parameters defined in table B.1 there are two more flags in ”param.dat” file: ”cs” and ”Process”. The first one dictates whether or not to calculate the cross sections and/or to generate events. The second sets which physical process should be taken into account. If ”cs” is set to 0, the cross sections for all sub-processes defined by the ”Process” flag will be calculated and no generation will be performed. The result will be stored in the CS folder, in a csX.txt file, where X can be ”Dtop”,”Gtop” and ”Lqtop”. If ”cs” is set to 1, only the event generation will be performed. In this case events are produced according to the calculated cross sections. After generation, the .LHE files will be stored in the Events folder together with a file ”runinfo.txt” which stores all information related to the event generation.

top-quark FCNC interactions were introduced in MEtop through an effective lagrangian. Depending on which operators are ”turned on”, different physics will be generated. Two different topologies are available: $2 \to 1 \to 3$ and $2 \to 2 \to 4$. [1] The first one concerns ”Direct top” production, and the second is related to ”top+gluon” and ”top+ light quark”.

Process Number	Description	Comments
1	Direct top (LO)	Strong Op. only
2	top+gluon (LO)	Strong Op. only; set PTmin
3	top+quark (LO)	All Op.; set PTmin
21	Direct top (NLO)	Strong Op. only
22	Direct top (NLO) + top+quark (LO)	All Op.

Table B.2: Processes available in MEtop

Strong FCNC top interactions are included in MEtop through two equivalent effective operators, one for the top-up-gluon interaction, and the other for the interaction of the top with a c-quark. In process 1, only the strong coupling constants are needed. Process 2 has the same effective operators but due to the infrared divergences appearing in top+gluon production a cut in the top-quark transverse momentum has to be set via the variable PTmin. In process 3, top + light quark [2] production, all operators can contribute, strong, electroweak and 4F. It is now possible to choose which operators to include. Again a value for PTmin has to be chosen.

---

[1] When ”SpCorr” is set to 0, the top-quark decay will not be performed in MEtop, that is, the generated events will have the topology $2 \to 1$ and $2 \to 2$. In this case the spin correlations are lost.

[2] Here light quark stands for the set $u, \bar{u}, d, \bar{d}, c, \bar{c}, s, \bar{s}, b, \bar{b}$.

Process 21 is inclusive direct top production at NLO and again only strong operators intervene. The NLO result is obtained by a matching procedure (as described previously) which depends on one variable, PTmatch, to be chosen by the user. The cross section results are written in three files: ”csDtopLO.txt”, the LO result for direct top, ”csDtopNLO.txt”, the NLO increment relative to the LO result ($\sigma_{NLO}^{Total} - \sigma_{LO}^{Total}$), and ”csGtop.txt”, the LO cross section for ”top+gluon” process with a top quark transverse momentum above ”PTmatch”. Therefore the variable ”PTmin” is irrelevant for this process. After the generation, the results are stored in one file in the Events folder named ”DtopNLO.lhe”, containing $2 \to 1 \to 3$ and the $2 \to 2 \to 4$ configurations. These events constitute the inclusive direct top NLO event generation, and must subsequently be showered by PYTHIA using the P_T-ordered scheme, in order to complete the matching procedure. Finally, with process 22, MEtop sums process 21 with process 3. The ”PTmacth” variable plays the same role as in process 21 and ”PTmin” will be the top transverse momentum cut, for the ”top + quark” sub-processes.

B.3 Running MEtop

To run the package you just have to execute the command ”./run.py” in the main directory. Care should be taken when changing the values of the physical parameters and/or the process you wish to calculate. In such cases you must always recalculate the value of the cross section. In addition, if you change the process used for the generation, you must be sure that all cross sections pertaining the new process are calculated beforehand. This is mandatory because the generation is done using the cs*.txt files saved in the CS folder.

References

[1] J. A. Aguilar-Saavedra. *Acta Phys. Polon. B*, **35**:2695, 2004.

[2] A. Heister et al. ALEPH Coll. *Phys. Lett.*, B543:173, 2002.

[3] DELPHI Coll. J. Abdallah et al. *Phys. Lett.*, B509:21, 2004.

[4] G. Abbiendi et al. OPAL Coll. *Phys. Lett.*, B521:181, 2001.

[5] P. Achard et al. L3 Coll. *Phys. Lett.*, B549:290, 2002.

[6] H. Abramowicz et al. ZEUS Coll. *Phys. Lett.*, B708:27, 2012.

[7] F. D. Aaron et al. H1 Coll. *Phys. Lett.*, B678:450, 2009.

[8] F. Abe et al. CDF Coll. *Phys. Rev. Lett.*, 80:2525, 1998.

[9] R. Santos R. Guedes and M. Won. [arXiv:1007.2992 [hep-ph]].

[10] V. M. Abazov et al. D0 Collaboration. *Phys. Lett.*, B701:313, 2011.

[11] T. Aaltonen et al. CDF Collaboration. *Phys. Rev. Lett.*, 201:192002, 2008.

[12] G. Aad et al. ATLAS Collaboration. [arXiv:1206.0257.

[13] T. Aaltonen et al. CDF Collaboration. CMS-PAS-TOP-11-028.

[14] G. Aad *et al.* [ATLAS Collaboration]. *Phys. Lett. B*, 712:351, 2012, [arXiv:1203.0529v2 [hep-ph]].

[15] T. Aaltonen *et al.* [CDF Collaboration]. *Phys. Rev. Lett.*, 101:202001, 2008, [arXiv:0806.2472 [hep-ex]].

[16] J. H. Kuhn and G. Rodrigo. *Phys. Rev. Lett.*, 81:49, 1998, [arXiv:hep-ph/9802268].

[17] J. H. Kuhn and G. Rodrigo. *Phys. Rev. D*, 59:054017, 1999, [arXiv:hep-ph/9807420].

[18] E. Boos et al. *Phys. Atom. Nucl.*, 69:1317, 2006 [Yad. Fiz. 69 (2006) 1352].

[19] G. P. Lepage. *Journal of Computational Physics*, **27**:192–203, 1978.

[20] T. Hahn. *Comput. Phys. Commun.*, **168**:78, 2005.

[21] J. Beringer et al. (Particle Data Group). *Phys. Rev. D*, **86**:010001, 2012.

[22] Torbjorn Sjostrand, Stephen Mrenna, and Peter Z. Skands. PYTHIA 6.4 Physics and Manual. *JHEP*, 0605:026, 2006, hep-ph/0603175.

[23] G. Corcella, I.G. Knowles, G. Marchesini, S. Moretti, K. Odagiri, et al. HERWIG 6: An Event generator for hadron emission reactions with interfering gluons (including supersymmetric processes). *JHEP*, 0101:010, 2001, hep-ph/0011363.

[24] J. Alwall et all. *Comput.Phys.Commun.*, **176**:300–304, 2007.

[25] J. F. Owens, A. Accardi, and W. Melnitchouk. [arXiv:1212.1702v1. http://www.phys.psu.edu/∼cteq.

[26] A.D. Martin, W.J. Stirling, R.S. Thorne, and G. Watt. *Eur. Phys. J. C*, 63:189–285, 2009, [arXiv:0901.0002v3. http://mstwpdf.hepforge.org.

[27] Ian J. R. Aitchison and Anthony J. G. Hey. *Gauge Theories in Particle Physics, Third Edition - Volume II*, 2004.

[28] W. J. Stirling R. K. Ellis and B. R. Webber. *QCD and Collider Physics*, page Cambridge University Press, 1996.

[29] T. Kinoshita. *J. Math. Phys.*, 3:650–667, 1962.

[30] M. Nauenberg T. D. Lee. *Phys. Rev. 133*, pages B1549–B1562, 1962.

[31] Guido Altarelli and G. Parisi. *Nucl. Phys. B*, **126**:298, 1997.

[32] F. Ambroglini et all. 2009, [arXiv:0902.0293v1.

[33] Torbjorn Sjostran. *Introduction to Monte Carlo Event Generators*, Lectures given in CTEQ-MCnet School 2010.

[34] D. Amati et all. *Nucl. Phys. B*, 173:429, 1980.

[35] K. Nakamura et al. (Particle Data Group). *J. Phys. G*, **37**:075021, 2010.

[36] S. L. Glashow. *Nucl. Phys.*, 22:579?588, 1961.

[37] A. Salam. Proceedings Of The Nobel Symposium Held 1968 at Lerum, Sweden, Stockholm, 1968.

[38] S. Weinberg. *Phys. Rev. Lett.*, 19:1264?1266, 1967.

[39] H. Georgi. *Ann. Rev. Nucl. Part. Sci*, **43**:209, 1993.

[40] C. Itzykson and J.B. Zuber. *Quantum Field Theory.* McGraw-Hill, New York, 1980.

[41] T. Appelquist and J. Carazzone. *Phys. Rev. D*, **11**:2856, 1975.

[42] W. Buchmuller and D. Wyler. *Nucl. Phys. B*, **268**:621, 1986.

[43] B. Grzadkowski, M. Iskrzynski, M. Misiak, and J. Rosiek. *JHEP*, 1010:085, 2010, [arXiv:1008.4884 [hep-ph]].

[44] J. A. Aguilar-Saavedra. *Nucl. Phys. B*, **812**:182–204, 2009.

[45] L. Maiani S.L. Glashow, J. Iliopoulos. *Phys. Rev. D*, **2 (7)**:1285, 1986.

[46] J. L. Hewett G. Eilam and A. Soni. *Phys. Rev. D*, **44**:1473, 1991 [Erratum-ibid. D 59 (1999) 039901].

[47] L. Reina D. Atwood and A. Soni. *Phys. Rev. D*, **55**:3156, 1997.

[48] P. M. Ferreira, R. B. Guedes, and R. Santos. *Phys. Rev. D*, 77:114008, 2008, [arXiv:0802.2075 [hep-ph]].

[49] R. A. Coimbra, P. M. Ferreira, R. B. Guedes, O. Oliveira, A. Onofre, R. Santos, and M. Won. *Phys. Rev. D*, 79:014006, 2009, arXiv:0811.1743 [hep-ph]].

[50] J. A. Aguilar-Saavedra. *Nucl. Phys. B*, 812:181–204, 2009, [arXiv:0811.3842 [hep-ph]].

[51] L. L. Yang J. J. Liu, C. S. Li and L. G. Jin. *Phys. Rev. D*, **72**:074018, 2005.

[52] J. A. Aguilar-Saavedra. *Nucl. Phys. B*, **843**:638, 2010 [Erratum-ibid.B851:443-444,2011].

[53] A. V. Semenov. *Comput. Phys. Commun.*, 180:431–454, 2009, [arXiv:0805.0555.

[54] A. Belyaev et all. *JHEP*, **0509**:005, 2005.

[55] P. M. Ferreira, O. Oliveira, and R. Santos. *Phys. Rev. D*, 73:034011, 2006, [arXiv:hep-ph/0510087.

[56] P. M. Ferreira and R. Santos. *CDF Conference Note 10807 (2012)*, 73:054025, 2006, [arXiv:hep-ph/0601078.

[57] J. A. Aguilar-Saavedra. *Nucl. Phys. B*, 843:638–672, 2011, [arXiv:1008.3562 [hep-ph]].

[58] P. J. Fox *et al.* *Phys. Rev. D*, 78:054008, 2008.

[59] B. Grzadkowski and M. Misiak. *Phys. Rev. D*, 78:077501, 2008.

[60] J. Carvalho *et al.* *Eur. Phys. J.*, 52:999–1019, 2007.

[61] T. Lari *et al.* Report of Working Group 1 of the CERN Workshop "Flavour in the era of the LHC".

[62] CMS Physics TDR: Volume II, CERN/LHCC 2006-021.

[63] T. L. Cheng and P. Teixeira-Dias. ATL-PHYS-PUB-2006-029.

[64] S. Bar-Shalom and J. Wudka. *Phys. Rev. D*, 60:094016, 1999.

[65] S. Andringa *et al* DELPHI collaboration. *Phys. Rev. D*, 60:094016, DELPHI 2006-003 CONF 749, 2006. F.Veloso, Master Thesis, Univ. Técnica de Lisboa, 2004.

[66] J. A. Aguilar-Saavedra. *Phys. Lett. B*, 502:115, 2001.

[67] J. A. Aguilar-Saavedra and T. Riemann.

[68] T. Han and J. L. Hewett. *Phys. Rev. D*, 60:074015, 1999.

[69] A. Soni S. Bar-Shalom, G. Eilam and J. Wudka. *Phys. Rev. Lett.*, 79:1217, 1997.

[70] K. Whisnant K. J. Abraham and B. L. Young. *Phys. Lett. B*, 419:381, 1998.

[71] E. E. Boos. *Nucl. Instrum. Meth. A*, 472:22, 2001.

[72] J. J. Zhang *et al. Phys. Rev. Lett.*, 102:072001, 2009.

[73] V. M. Abazov *et al.* [D0 Collaboration]. *Phys. Rev. Lett.*, 100:142002, 2008, [arXiv:0712.0851 [hep-ex]].

[74] T. Aaltonen *et al.* [CDF Collaboration]. *Phys. Rev D*, 83:112003, 2011, [arXiv:1101.0034 [hep-ex]].

[75] T. Aaltonen *et al.* [CDF Collaboration]. *Phys. Rev. Lett.*, 105:012001, 2010, [arXiv:1004.3224 [hep-ex]].

[76] J. M. Campbell and R. K. Ellis. *Phys. Rev. D*, 60:113006, 1999, [arXiv:hep-ph/9905386].

[77] Code available from http://mcfm.fnal.gov/.

[78] T. Aaltonen *et al.* [CDF Collaboration]. *Phys. Rev. Lett.*, 102:222003, 2009, [arXiv:0903.2850 [hep-ex]].

[79] D. Pagani W. Hollik. [arXiv:1107.2606 [hep-ph]].

[80] G. Rodrigo J. H. Kuhn. [arXiv:1109.6830 [hep-ph]].

[81] V. Ahrens, A. Ferroglia, M. Neubert, B. D. Pecjak, and L. L. Yang. *Phys. Rev. D*, 84:074004, 2011, [arXiv:1106.6051 [hep-ph]].

[82] V. M. Abazov *et al.* [D0 Collaboration]. [arXiv:1107.4995 [hep-ex]].

[83] B. Grinstein, A. L. Kagan, J. Zupan, and M. Trott. [arXiv:1108.4027 [hep-ph]].

[84] Q. H. Cao, D. McKeen, J. L. Rosner, G. Shaughnessy, and C. E. M. Wagner. *Phys. Rev. D*, 81:114004, 2010, [arXiv:1003.3461 [hep-ph]].

[85] E. Gabrielli, M. Raidal, and A. Racioppi. [arXiv:1112.5885 [hep-ph]].

[86] E. Gabrielli and M. Raidal. *Phys. Rev. D*, 84:054017, 2011, [arXiv:1106.4553 [hep-ph]].

[87] J. Cao, K. Hikasa, L. Wang, L. Wu, and J. M. Yang. [arXiv:1109.6543 [hep-ph]].

[88] J. A. Aguilar-Saavedra, A. Juste, and F. Rubbo. [arXiv:1109.3710 [hep-ph]].

[89] J. Y. Liu, Y. Tang, and Y. L. Wu. [arXiv:1108.5012 [hep-ph]].

[90] P. Ko, Y. Omura, and C. Yu. [arXiv:1108.4005 [hep-ph]].

[91] S. Jung, A. Pierce, and J. D. Wells. [arXiv:1108.1802 [hep-ph]].

[92] Y. Bai and Z. Han. [arXiv:1106.5071 [hep-ph]].

[93] P. Ko, Y. Omura, and C. Yu. [arXiv:1108.0350 [hep-ph]].

[94] D. Krohn, T. Liu, J. Shelton, and L. T. Wang. [arXiv:1105.3743 [hep-ph]].

[95] C. H. Chen, S. S. C. Law, and R. H. C. Li. [arXiv:1104.1497 [hep-ph]].

[96] J. A. Aguilar-Saavedra and M. Perez-Victoria. *Phys. Lett. B*, 701:93, 2011, [arXiv:1104.1385 [hep-ph]].

[97] M. R. Buckley, D. Hooper, J. Kopp, and E. Neil. *Phys. Rev. D*, 83:115013, 2011, [arXiv:1103.6035 [hep-ph]].

[98] S. Jung, A. Pierce, and J. D. Wells. *Phys. Rev. D*, 83:114039, 2011, [arXiv:1103.4835 [hep-ph]].

[99] G. Rodrigo and P. Ferrario. *Nuovo Cim. C*, 33:04, 2010, [arXiv:1007.4328 [hep-ph]].

[100] R. S. Chivukula, E. H. Simmons, and C. P. Yuan. *Phys. Rev. D*, 82:094009, 2010, [arXiv:1007.0260 [hep-ph]].

[101] B. Xiao, Y. k. Wang, and S. h. Zhu. *Phys. Rev. D*, 82:034026, 2010, [arXiv:1006.2510 [hep-ph]].

[102] A. Rajaraman, Z. Surujon, and T. M. P. Tait. [arXiv:1104.0947 [hep-ph]].

[103] J. Shu, K. Wang, and G. Zhu. [arXiv:1104.0083 [hep-ph]].

[104] M. I. Gresham, I. W. Kim, and K. M. Zurek. arXiv:1103.3501 [hep-ph]].

[105] N. Craig, C. Kilic, and M. J. Strassler. [arXiv:1103.2127 [hep-ph]].

[106] E. R. Barreto, Y. A. Coutinho, and J. Sa Borges. *Phys. Rev. D*, 83:054006, 2011, [arXiv:1103.1266 [hep-ph]].

[107] A. R. Zerwekh. [arXiv:1103.0956 [hep-ph]].

[108] B. Bhattacherjee, S. S. Biswal, and D. Ghosh. [arXiv:1102.0545 [hep-ph]].

[109] M. I. Gresham, I. W. Kim, and K. M. Zurek. [arXiv:1102.0018 [hep-ph]].

[110] J. Cao, L. Wang, L. Wu, and J. M. Yang. [arXiv:1101.4456 [hep-ph]].

[111] P. H. Frampton, J. Shu, and K. Wang. *Phys. Lett. B*, 683:294, 2010, [arXiv:0911.2955 [hep-ph]];.

[112] K. Cheung, W. Y. Keung, and T. C. Yuan. *Phys. Lett. B*, 682:287, 2009, [arXiv:0908.2589 [hep-ph]].

[113] S. Jung, H. Murayama, A. Pierce, and J. D. Wells. *Phys. Rev. D*, 81:015004, 2010, [arXiv:0907.4112 [hep-ph]].

[114] D. K. Ghosh, A. Nyffeler, V. Ravindran, N. Agarwal, P. Agarwal, P. Bandyopadhyay, R. Basu, and B. Bhattacherjee *et al.* *Pramana*, 76:707, 2011.

[115] G. Isidori and J. F. Kamenik. pages [arXiv:1103.0016 [hep–ph]].

[116] L. Wu J. Cao, Z. Heng and J. M. Yang. *Phys. Rev. D*, 81:014016, 2010, [arXiv:0912.1447 [hep-ph]].

[117] C. H. Chen, G. Cvetic, and C. S. Kim. *Phys. Lett. B*, 694:393, 2011, [arXiv:1009.4165 [hep-ph]].

[118] H. Wang, Y. k. Wang, B. Xiao, and S. h. Zhu. [arXiv:1107.5769 [hep-ph]].

[119] B. Xiao, Y. k. Wang, and S. h. Zhu. [arXiv:1011.0152 [hep-ph]].

[120] M. V. Martynov and A. D. Smirnov. [arXiv:1010.5649 [hep-ph]].

[121] M. V. Martynov and A. D. Smirnov. *Mod. Phys. Lett. A*, 25:2637, 2010, [arXiv:1006.4246 [hep-ph]].

[122] P. Ferrario and G. Rodrigo. *Phys. Rev. D*, 80:051701, 2009, [arXiv:0906.5541 [hep-ph]].

[123] R. Foot. *Phys. Rev. D*, 83:114013, 2011, [arXiv:1103.1940 [hep-ph]].

[124] A. Djouadi, G. Moreau, and F. Richard. *Phys. Lett. B*, 701:458, 2011, [arXiv:1105.3158 [hep-ph]].

[125] M. Bauer, F. Goertz, U. Haisch, T. Pfoh, and S. Westhoff. *JHEP*, 1011:039, 2010, [arXiv:1008.0742 [hep-ph]].

[126] A. Djouadi, G. Moreau, F. Richard, and R. K. Singh. *Phys. Rev. D*, 82:071702, 2010, [arXiv:0906.0604 [hep-ph]].

[127] A. Djouadi, G. Moreau, and F. Richard. *Nucl. Phys. B*, 773:43, 2007, [arXiv:hep-ph/0610173].

[128] Nobuhiro Uekusa. [arXiv:0912.1218 [hep-ph]].

[129] Hooman Davoudiasl, Thomas McElmurry, and Amarjit Soni. [arXiv:1108.1173 [hep-ph]].

[130] A. Arhrib, R. Benbrik, and C. H. Chen. *Phys. Rev. D*, 82:034034, 2010, [arXiv:0911.4875 [hep-ph]].

[131] J. Shu, T. M. P. Tait, and K. Wang. *Phys. Rev. D*, 81:034012, 2010, [arXiv:0911.3237 [hep-ph]].

[132] K. M. Patel and P. Sharma. *JHEP*, 1104:085, 2011, [arXiv:1102.4736 [hep-ph]].

[133] I. Dorsner, S. Fajfer, J. F. Kamenik, and N. Kosnik. *Phys. Rev. D*, 81:055009, 2010, [arXiv:0912.0972 [hep-ph]].

[134] T. Aaltonen *et al.* [The CDF Collaboration]. [arXiv:1107.5063 [hep-ex].

[135] T. Aaltonen *et al.* [CDF Collaboration]. [arXiv:1108.4755 [hep-ex].

[136] J. A. Aguilar-Saavedra and M. Perez-Victoria. [arXiv:1107.2120 [hep-ph]].

[137] J. A. Aguilar-Saavedra and M. Perez-Victoria. [arXiv:1107.0841 [hep-ph]].

[138] J. A. Aguilar-Saavedra and M. Perez-Victoria. [arXiv:1105.4606 [hep-ph]].

[139] M. Perez-Victoria J. A. Aguilar-Saavedra. *JHEP*, 1105:034, 2011, [arXiv:1103.2765 [hep-ph]].

[140] C. Delaunay, O. Gedalia, Y. Hochberg, G. Perez, and Y. Soreq. [arXiv:1103.2297 [hep-ph]].

[141] C. Degrande, J. M. Gerard, C. Grojean, F. Maltoni, and G. Servant. *JHEP*, 1103:125, 2011, [arXiv:1010.6304 [hep-ph]].

[142] D. W. Jung, P. Ko, J. S. Lee, and S. h. Nam. *Phys. Lett. B*, 691:238, 2010, [arXiv:0912.1105 [hep-ph]].

[143] D. Y. Shao, C. S. Li, J. Wang, J. Gao, H. Zhang, and H. X. Zhu. [arXiv:1107.4012 [hep-ph]].

[144] J. Drobnak, S. Fajfer, and J. F. Kamenik. *Phys. Lett. B*, 701:234, 2011, [arXiv:1102.4347 [hep-ph]].

[145] Q. H. Cao, J. Wudka, and C. P. Yuan. *Phys. Lett. B*, 658:50, 2007, [arXiv:0704.2809 [hep-ph]].

[146] C. Zhang, N. Greiner, and S. Willenbrock. [arXiv:1201.6670 [hep-ph]].

[147] N. Greiner, S. Willenbrock, and C. Zhang. *Phys. Lett. B*, 704:218, 2011, [arXiv:1104.3122 [hep-ph]].

[148] F. Abe *et al.* [CDF Collaboration]. *Phys. Rev. Lett.*, 80:2525, 1998.

[149] ATLAS Collaboration. *ATLAS-CONF-2011-154 (2011).*

[150] H. Abramowicz *et al.* [ZEUS Collaboration]. *Phys. Lett. B*, 708:27, 2012, [arXiv:1111.3901 [hep-ex].

[151] P. M. Ferreira and R. Santos. *Phys. Rev. D*, 80:114006, 2009, [arXiv:0903.4470 [hep-ph]].

[152] T. J. Kim. [arXiv:1201.4772 [hep-ex]].

[153] D. Choudhury, R. M. Godbole, S. D. Rindani, and P. Saha. *Phys. Rev. D*, 84:014023, 2011, [arXiv:1012.4750 [hep-ph]].

[154] J. A. Aguilar-Saavedra. *Nucl. Phys.*, B837:122–136, 2010.

[155] S. R. Slabospitsky and L. Sonnenschein. *Phys. Lett.*, 148:87, 2002.

[156] E. Boos et al. [CompHEP Collaboration]. *Nucl. Instrum. Meth A*, 534:250, 2004.

[157] V. M. Abazov *et al.* [D0 Collaboration]. *Phys. Lett. B*, 701:313, 2011.

[158] T. Aaltonen *et al.* [CDF Collaboration]. *Phys. Rev. Lett.*, 101:192002, 2008.

[159] A. Pukhov *et al.* [arXiv:hep-ph/9908288;arXiv:hep-ph/0412191.

[160] J. Alwall *et al.* *JHEP*, 1106:128, 2011.

[161] J. J. Zhang et al. *Phys. Rev. Lett.*, 102:072001, 2009.

[162] S. Mrenna T. Sjostrand and P. Skands. *JHEP*, 05:026, 2006.

[163] V. M. Abazov *et al.* [D0 Collaboration]. *Phys. Lett. B*, 693:81, 2010.

[164] J. J. Zhang J. Gao, C. S. Li and H. X. Zhu. *Phys. Rev. D*, 80:114017, 2009.

[165] S. M. Etesami and M. Mohammadi Najafabadi. *Phys. Rev. D*, 81:117502, 2010.

[166] S. Alioli, P. Nason, C. Oleari, and E. Re. *JHEP*, 1006:043, 2010.

[167] M. L. Mangano, M. Moretti, F. Piccinini, R. Pittau, and A. D. Polosa. *JHEP*, 0307:001, 2003.

[168] JM. Mangano. *Merging multijet matrix elements and shower evolution in hadronic collisions.* http://cern.ch/%7Emlm/talks/lund-alpgen.pdf (2004).

[169] P. Z. Skands. [arXiv:0905.3418 [hep-ph].].

[170] ATLAS Monte Carlo tunes for MC09. ATL-PHYS-PUB-2010-002.

[171] S. Ovyn, X. Rouby, and V. Lemaitre. [arXiv:0903.2225 [hep-ph]].

[172] F. M. A. Veloso, J. Carvalho, and A. Onofre. *Study of ATLAS sensitivity to FCNC top quark decays.* CERN-THESIS-2008-106.

[173] ATLAS Collaboration. *ATLAS-CONF-2013-063.*